

# Privacy-Preserving EHR Transformation with Mathematical Guarantees: A Human–AI Co-Designed Solution

Maolin Wang<sup>1,†</sup>, Beining Bao<sup>1,†</sup>, Gan Yuan<sup>2</sup>, Hongyu Chen<sup>1</sup>, Bingkun Zhao<sup>1</sup>, Baoshuo Kan<sup>1</sup>, Jiming Xu<sup>4</sup>,  
Qi Shi<sup>1</sup>, Yinggong Zhao<sup>1</sup>, Yao Wang<sup>1</sup>, Wei-Ying Ma<sup>1</sup>, Jun Yan<sup>1,2,3</sup>

<sup>1</sup>Hong Kong Institute of AI for Science (HKAI-Sci), City University of Hong Kong

<sup>2</sup>Department of Biostatistics, City University of Hong Kong

<sup>3</sup>Institute of Digital Medicine, City University of Hong Kong

<sup>4</sup>YIDU TECH co. Ltd.

 [Code & Projects](#)

## Abstract

Electronic health records (EHRs) and other real-world clinical data are essential for clinical research, medical artificial intelligence, and life science, but their sharing is severely limited by privacy, governance, and interoperability constraints. These barriers create persistent data silos that hinder multi-center studies, large-scale model development, and broader biomedical discovery. Existing privacy-preserving approaches, including multi-party computation and related cryptographic techniques, provide strong protection but often introduce substantial computational overhead, reducing the efficiency of large-scale machine learning and foundation-model training. In addition, many such methods make data usable for restricted computation while leaving them effectively invisible to clinicians and researchers, limiting their value in workflows that still require direct inspection, exploratory analysis, and human interpretation. We propose a real-world-data transformation framework for privacy-preserving sharing of structured clinical records. Instead of converting data into opaque representations, our approach constructs transformed numeric views that preserve medical semantics and major statistical properties while, under a clearly specified threat model, provably breaking direct linkage between those views and protected patient-level attributes. Through collaboration between computer scientists and the AI agent **SciencePal**, acting as a constrained tool inventor under human guidance, we design three transformation operators that are non-reversible within this threat model, together with an additional mixing strategy for high-risk scenarios, supported by theoretical analysis and empirical evaluation under reconstruction, record linkage, membership inference, and attribute inference attacks. Although we implement and evaluate the framework on intensive care unit (ICU) data as one representative clinical use case, it is intended for structured EHR and real-world clinical datasets in general, offering a practical and computationally feasible path toward privacy-preserving clinical data access, sharing, and exchange, and ultimately supporting multi-center studies, cross-institutional training of large-scale models, and translational life-science research.

## 1 Introduction

### 1.1 From Model Bottlenecks to Data Bottlenecks

Electronic health records (EHRs) and other forms of real-world clinical data have become central resources in modern clinical AI. Large neural networks and foundation models are now widely applied to diagnosis prediction, risk stratification, clinical decision support, and multimodal patient summarization across diverse healthcare settings (Johnson et al., 2023a; 2016; Harutyunyan et al., 2019). For many hospitals and research

<sup>†</sup>Equal Contribution.

groups, having a sufficiently powerful model is no longer the primary obstacle: open-source and commercial models are increasingly abundant, and cloud compute is relatively accessible (Rajpurkar et al., 2017).

In practice, a more pressing concern repeatedly surfaces in our collaborations with hospital IT and data governance teams: the real bottleneck lies not in the model, but in the data. Under the joint constraints of regulation, ethics, and institutional governance, high-quality clinical data containing longitudinal records, time series, laboratory results, medications, and treatment histories are often required to remain strictly within hospital intranets or controlled environments (van Velzen et al., 2025; Conduah et al., 2025; Goldberger et al., 2000). They cannot be freely copied to research clouds, let alone uploaded to third-party platforms (Kaissis et al., 2020; Rieke et al., 2020; Aggarwal & Yu, 2008). Even for internal research teams, many hospitals expose only restricted query interfaces or sandboxed environments, while external collaborators often have access only to heavily aggregated or de-identified summaries.

These arrangements are essential for patient privacy, but they create a shared practical difficulty for clinical research and deployment: models can move, data cannot. Algorithm engineers struggle to perform systematic exploratory data analysis (EDA), quality checks, and pipeline debugging on the true data distribution. Clinicians lack sufficiently rich cohort-level views to judge whether a study population is well defined or whether a statistical pattern is clinically plausible. At the current stage of clinical AI, data availability and governability, rather than model capacity alone, constitute the primary bottleneck (Deng et al., 2022; Rojas et al., 2018). Although this challenge applies broadly to structured EHR and real-world clinical datasets, in the following sections we use ICU data as a representative and practically important showcase.

## 1.2 Mainstream Approaches: Usable but Invisible

To enable joint analysis and modeling without exposing plaintext data, the privacy-preserving computation community has developed a rich set of methods, including multi-party computation (MPC), homomorphic encryption (HE), trusted execution environments (TEE), federated learning, and differentially private (DP) query or training mechanisms. These approaches have substantially advanced the state of secure data use and are especially valuable in settings where formal protection guarantees are paramount and direct human access to raw records is neither necessary nor desirable. Over the past decade, this toolbox has expanded from classical secure query answering to deep and federated models, with practical implementations of neural networks over encrypted data and large-scale federated optimization now available in both research prototypes and open-source frameworks (Gilad-Bachrach et al., 2016; Yuan et al., 2025; McMahan et al., 2017; Kairouz et al., 2021; Munjal & Bhatia, 2023).

From a systems perspective, however, many of these methods occupy what may be called the *usable but invisible* design quadrant: models and algorithms can train or infer on encrypted values, protected hardware, distributed parameters, or privacy-filtered outputs, while humans see little to none of the underlying individual records or per-point values. This property is a strength in many high-value applications, such as privacy-sensitive multi-institutional model training, secure cross-site analytics, and the release of protected aggregate statistics (McMahan et al., 2017; Dwork & Roth, 2014; Munjal & Bhatia, 2023). In such scenarios, the primary requirement is trustworthy computation rather than visible data access, and cryptographic or DP-based mechanisms are an appropriate—and often necessary—engineering choice.

Several lines of work nonetheless point out that this design point can become more restrictive in everyday clinical research and real-world model development. First, many cryptographic and privacy-preserving pipelines introduce substantial overhead in computation, communication, and system complexity. Empirical evaluations of HE- and MPC-based deep learning schemes, as well as surveys of approximate-HE PPML systems and federated learning, report significant slowdowns and communication costs compared with plaintext training, even for moderate-size neural networks (Gilad-Bachrach et al., 2016; Yuan et al., 2025; Kairouz et al., 2021). While such costs may be acceptable for narrowly scoped secure analytics, they can become a practical burden for large-scale machine learning workflows, repeated ablation studies, and especially foundation-model training on high-dimensional clinical data, where practitioners already face tight GPU budgets and long wall-clock times. Differentially private training introduces an additional layer of trade-offs: DP-SGD protects training examples but typically requires more iterations and can reduce accuracy, with the degradation being particularly pronounced for complex models and under-represented subgroups (Bagdasaryan et al., 2019). These efficiency and utility costs do not negate the value of these methods, but they do make it harder to adopt them as the default for exploratory, iteration-heavy large-model development.

Second, many real-world research tasks still depend on data being not only computable, but also inspectable. Algorithm engineers often need to run detailed exploratory data analysis, quality checks, failure diagnosis,

and pipeline debugging on actual numeric tables in order to identify missingness patterns, temporal misalignment, distribution shift, or data processing errors (Pineau et al., 2021). Qualitative studies of high-stakes AI similarly find that practitioners spend substantial effort on “data work”—cleaning, reformatting, and visually inspecting raw and intermediate datasets—and that breakdowns in this process can trigger cascading downstream failures (Sambasivan et al., 2021). In clinical domains, secondary analyses of electronic health records (EHRs) and other real-world data repeatedly emphasize that these sources are heterogeneous, noisy, and biased, and thus require intensive preprocessing and medical validation before robust modeling is possible (Liu & Panagiotakos, 2022). Clinicians rely on visible cohort-level data views to judge whether a study population is medically coherent and whether an observed pattern is clinically plausible, while regulators and hospital IT teams may require data representations that are interpretable enough to support practical auditing and governance.

As a result, even when hospitals possess sizable EHR warehouses and substantial computing infrastructure, there remains a gap between methods that are secure in principle and data views that are truly usable in day-to-day scientific practice. This gap is particularly important for structured clinical records and real-world data, where privacy protection must coexist with interpretability, workflow efficiency, and the operational realities of collaborative research and large-model development (Artsi et al., 2025).

### 1.3 Human–AI Co-Design with SciencePal

Privacy-preserving yet clinically interpretable data views require transformation operators that satisfy multiple, sometimes competing, requirements: they should preserve medical meaning and cohort-level statistics, make it infeasible to reverse sensitive individual information under our threat model, and remain simple and cheap enough to deploy on routine hospital infrastructure. To search this design space, we adopt a human–AI co-design paradigm.

Rather than letting an AI agent use high-compute tools, we ask the AI to *design* low-compute tools (Shin et al., 2025; Niu et al., 2025; Shahin et al., 2025). The AI role in this process is played by **SciencePal**<sup>1</sup>, an AI research assistant that provided preliminary ideas and candidate proposals at each stage. Human researchers define the problem, specify constraints, and validate every claim; SciencePal explores the space of possible operators and attack sketches under these constraints. The overall protocol proceeds in three iterative phases.

In the first phase, human researchers specify qualitative and quantitative constraints that any candidate operator must satisfy. At a high level, cohort-level means and variances should be preserved, perturbations should be uniformly bounded by a small, human-controlled privacy knob, most data points should actually be perturbed rather than left unchanged, and per-column computation should scale linearly with the number of records and run on commodity CPUs without long-lived shared keys. Formal definitions and proofs of these properties are given later in the paper, but here they serve as a checklist guiding the design search.

In the second phase, SciencePal acts as a constrained tool inventor. Given the human specification, it searches for operator families in the literature that approximately satisfy these requirements and, upon identifying a gap, proposes new geometric operators and mixing strategies that are intended to meet them. These proposals come with informal geometric intuition, standardized forms, Python pseudo-code, and explicit claims about which constraints are satisfied. Crucially, these are *preliminary ideas*: SciencePal contributes conceptual scaffolding, not verified tools.

In the third phase, the human team acts as both reviewer and attacker. We formalize the candidate operators, prove or refute the stated properties, and discard those that violate key constraints. On a MIMIC-IV ICU subset (Johnson et al., 2023a), we instantiate a Privacy Evaluation Protocol analogous to cryptographic security games, with three leakage levels (L0/L1/L2: no, few, or many paired samples) and four attack families (A: reconstruction, B: record linkage, C: membership inference, D: attribute inference) (Shokri et al., 2017; Carlini et al., 2021; Dick et al., 2023). We use these attacks to identify operators and parameter ranges that, under our threat model, provably prevent exact recovery of protected information while still preserving medical semantics and statistical structure, and to separate them from candidates that, although geometrically well-structured, remain highly invertible under strong attacks (Yeom et al., 2018; Hu et al., 2022).

### 1.4 Summary of the Framework and Contributions

Our framework can be viewed as a solution for transforming structured clinical and real-world data into views that remain clinically interpretable and statistically faithful, while making it theoretically impossible, under our threat model, to exactly reverse protected individual-level information. Privacy strength and utility

---

<sup>1</sup><https://sciencepal.ai>

loss are controlled by a single, human-interpretable privacy knob, enabling practitioners to tune the trade-off instead of relying on opaque de-identification heuristics. This makes “usable and visible” privacy-preserving numeric views a realistic option for many clinical and research workflows.

Formally, we cast column-level transformations as constrained motions on a *mean-variance manifold* with an  $\alpha$ -hierarchy. In standardized space, each column lies on the intersection of a zero-mean hyperplane and a fixed-norm sphere, and all operators are required to preserve cohort-level means and variances while keeping perturbations within a unified  $\ell_\infty$  bound  $\alpha$  (Freksen, 2021). This geometric view allows us to reason about which parts of the data distribution are preserved, which are randomized, and how irreversibility arises.

Three base operators emerge from this process.

**T1: Local triplet rotations.** Along the time axis, each standardized sequence is partitioned into short windows, and small random orthogonal rotations are applied in the local mean-zero subspace, preserving short-range autocorrelation while injecting controlled noise (Yoon et al., 2019).

**T2: Noise plus manifold projection.** Controlled noise is added in standardized space and then reprojected by re-centering and re-scaling onto the mean-variance manifold, which is particularly effective at preserving marginal distributions and multi-column correlation (Goodfellow et al., 2014b; Xu et al., 2019b).

**T3: Global Householder reflection (negative case).** We apply a single Householder reflection in the mean-zero subspace. This transformation nearly preserves all first and second order statistics as well as autocorrelation, but remains highly invertible under strong reconstruction attacks, and therefore serves as a negative control (Narayanan & Shmatikov, 2008).

Early experiments with fixed bounds in physical units revealed severe imbalance: low-variance variables were over-perturbed while high-variance variables were barely affected (Roman, 2023). Switching to a unified z-score bound  $\alpha$  automatically adapts perturbation magnitude to each variable’s scale, making the privacy-utility trade-off curve more interpretable. We further observe that merely increasing  $\alpha$  yields gradual rather than step-like privacy gains: even at large  $\alpha$ , some variables still admit high reconstruction  $R^2$  (Li et al., 2022). To address this, we introduce a per-stay orthogonal Q-mixing extension for a small set of high-risk variables. For each stay, a  $48 \times 48$  orthogonal mixing is applied to local time windows before applying T1 or T2. Under this construction, and with  $\alpha$  fixed at 1.0, linear reconstruction  $R^2$  for sensitive variables such as heart rate and glucose is driven close to zero, while preserving distributional shape and downstream prediction performance within acceptable ranges (Goncalves et al., 2020; Yuan et al., 2023). Together with our formal analysis, this provides both theoretical and empirical evidence that, at appropriate settings, the transformed views do not allow attackers in our model to reverse key privacy-sensitive attributes.

The main contributions of this paper are:

- 1. A real-world-data transformation solution that keeps data usable and visible under privacy constraints.** We introduce a unified geometric framework for column-level EHR and real-world clinical data transformations on a mean-variance manifold, providing a single privacy knob  $\alpha$  that trades small, quantifiable utility loss for provable non-reversibility of protected information under our threat model, while preserving medical semantics and key cohort-level statistics.
- 2. A family of non-reversible operators under our threat model and a tunable privacy-utility mechanism.** Building on this framework, we propose operators T1, T2, and a negative-control operator T3, together with a per-stay orthogonal Q-mixing extension that sharply reduces linear reconstruction  $R^2$  for high-risk variables without changing  $\alpha$ . We accompany these with a Privacy Evaluation Protocol with L0/L1/L2 leakage levels and A/B/C/D attack families to systematically evaluate privacy and utility.
- 3. An EHR-Privacy-Agent system for multi-scenario deployment.** We build a three-layer system (operators, modules, skills) running nightly CPU-only de-identification over in-hospital caches, with configurable privacy profiles for in-hospital research, teaching, and strong-privacy export scenarios, making privacy-preserving yet interpretable numeric views operationally feasible.
- 4. A human–AI co-design methodology with SciencePal.** We demonstrate a methodology in which SciencePal provides preliminary geometric ideas and experimental sketches, while human researchers specify constraints, prove properties, design attacks, and select deployable tools. Failures such as T3 are preserved as systematic negative cases, and the full division of labor is documented in the appendix, illustrating how an AI “scientist” can expand the search space while humans retain responsibility for the final scientific claims.

## 2 Background: Privacy-Preserving Data Release and Analysis

### 2.1 Privacy-Preserving Data Publishing and Mining

Classical work on privacy-preserving data publishing (PPDP) assumes that a data owner wishes to release a static dataset for offline analysis while reducing the risk of re-identification or sensitive attribute inference. Early work focuses on tabular microdata through two main lines of techniques. Equivalence-class based anonymization, including  $k$ -anonymity,  $\ell$ -diversity, and  $t$ -closeness, generalizes or suppresses quasi-identifiers so that each released record falls into an equivalence class of size at least  $k$  (Sweeney, 2002). Perturbation and permutation of numerical attributes, where values are blurred with noise, permuted, or aggregated into cluster centers, provides an alternative route to obscuring individual values (Marino et al., 2019; Hammer et al., 2024; Agrawal & Srikant, 2000).

Privacy-preserving data mining (PPDM) concentrates on performing mining tasks without directly releasing the dataset. Randomized response allows each data provider to locally randomize her own record before sending it to the analyst (Warner, 1965). Federated and distributed learning frameworks split training across multiple data holders, aggregating intermediate results through secure protocols without exposing raw records (McMahan et al., 2017; Kerrigan et al., 2020).

Together, PPDP and PPDM provide a rich toolbox for analyzing without fully exposing raw data (Fung et al., 2010; Aggarwal & Yu, 2004). However, most of this literature implicitly assumes that the analyst cares primarily about a derived statistical or mining result rather than a tabular view that human experts can directly use for EDA and visualization. Direct human access to per-column values, temporal structure, and cohort-level shapes is rarely treated as a first-class requirement. Two mismatches with the in-hospital structured EHR scenario (instantiated here on ICU data) are worth noting. Classical PPDP targets one-time release of a static dataset to external researchers, whereas we need repeated long-term in-hospital reuse: clinicians and engineers perform EDA, visualization, and pipeline debugging on cohorts repeatedly inside a secure hospital environment. Additionally, traditional PPDM views humans as consumers of final results rather than as participants who inspect data quality and structure midway through the workflow. In our setting, clinicians and IT staff both need to see the approximate shape and correlation structure of each column directly on the privacy-enhanced view.

### 2.2 Cryptographic Protocols in the Usable-but-Invisible Quadrant

Over the past decade, cryptography and systems security have produced powerful protocols that enable joint computation without revealing plaintext data. Secure multi-party computation (MPC) splits raw data into shares distributed across multiple parties, which jointly perform training or inference without reconstructing plaintext (Borges et al., 2025). Homomorphic encryption (HE) allows models to operate directly on encrypted data via supported algebraic operations (Goldreich, 2004). Trusted execution environments (TEE) run sensitive computation inside hardware enclaves with memory isolation and remote attestation, so that external parties cannot inspect plaintext data or intermediate states (Ohrimenko et al., 2016).

From a systems viewpoint, these methods lie in a usable-but-invisible design quadrant: models operate on protected representations while humans have essentially no access to per-record or per-timepoint values. This is ideal for multi-institutional training of prediction models, statistical agencies releasing differential-privacy-constrained official statistics, and joint analysis in finance or advertising where raw data must not be shared. In these settings, humans consume models or aggregate statistics rather than raw views, and not seeing plaintext is part of the design goal.

For the in-hospital structured EHR use case (instantiated in our experiments on ICU data), this quadrant is too narrow. Algorithm engineers need column-level numeric tables to perform EDA, quality checks, and pipeline debugging. Clinicians need to see cohort-level vital sign trajectories to apply medical intuition for sanity checks. Data governance and compliance teams must audit what a pipeline has done to specific variables such as heart rate or lactate, rather than simply trusting a black-box secure protocol. These needs intrinsically call for a visible data view, even if numerically transformed, as long as it remains clinically interpretable. The usable-but-invisible cryptographic toolbox is necessary but not sufficient: it solves cross-institutional secure modeling but does not cover the many daily clinical research workflows that depend on human inspection and intuition.

### 2.3 Differential Privacy and Synthetic Data

Differential privacy (DP) provides a formal privacy definition centered on the indistinguishability of neighboring databases and has been widely deployed for releasing statistics and training models (Dwork et al., 2006).

For EHR and tabular data, there is a growing body of work on DP-GAN, DP-VAE, and PATE-style generators that aim to produce datasets which statistically resemble real data while satisfying  $\epsilon$ -DP constraints (Liu et al., 2024; Tian et al., 2024; Jordon et al., 2018). In one-shot external release scenarios, these methods offer formal privacy bounds and high-level utility, preserving certain marginals and correlation structure for statistical analysis and model development.

However, transplanting DP-synthetic schemes directly into the in-hospital structured EHR setting (such as ICU time-series data) raises several practical issues. To satisfy global DP constraints, generative models often sacrifice fidelity on minority patterns and rare events, yet for clinical researchers the mean, variance, and range of individual lab tests are first-class objects in EDA. DP is also defined in terms of global randomness, so individual time-point deviations in synthetic data can be large and hard to bound; in contrast, one of our explicit goals is a unified z-score  $\ell_\infty$  bound  $\alpha$  so that clinicians can reason about perturbations in terms of standard deviations. DP-GAN and DP-VAE systems further require training relatively large models, consuming substantial privacy budgets during hyperparameter tuning, which is operationally expensive for a nightly pipeline running on hospital CPU clusters. Finally, many synthetic pipelines focus on statistical metrics and downstream task performance (Jordon et al., 2022; Loni et al., 2025), whereas actual EHR QA often requires inspecting questions such as what HR trajectories look like for a cohort or whether the tail of lactate behaves strangely; this demands geometrically controlled perturbations at the column and temporal levels, not just an overall resemblance.

## 2.4 Positioning: An In-Hospital Visible View

Putting the above together, existing privacy technologies fall into two main paradigms. The first is usable but invisible: cryptographic protocols allow models to operate safely on encrypted or protected data, but humans cannot see plaintext. The second is synthetic but DP-guaranteed: generative models and DP-sanitized releases provide formal privacy bounds for one-shot external publication, but make it difficult to precisely control column-level perturbations and temporal structure.

This paper addresses a third, complementary quadrant: constructing, within a controlled in-hospital environment, an EHR view that is usable and visible, yet non-reversible at the individual-record level under our no-key, structure-aware threat model. We do not attempt to replace MPC, HE, or TEE for cross-institutional training, nor do we compete with DP-synthetic GANs at the level of formal  $\epsilon$ -DP definitions. We focus instead on a gap in current practice: the lack of a geometrically controllable, EDA-friendly, nightly-generatable privacy-enhanced tabular view for in-hospital clinical research and QA pipelines (Riou et al., 2024; Jahan Sarmin et al., 2024). Against this backdrop, we now turn to related work on geometric transformations and synthetic EHR, asking which ideas can be adapted into candidate column-level operator families for our Human-AI co-design protocol.

## 3 Problem Formulation and Geometric View

### 3.1 Data and Pipeline Setup: From Structured EHR to Column-wise Operators

We consider a typical structured EHR warehouse containing longitudinal clinical measurements. Without loss of generality, we use intensive care unit (ICU) time-series data as a running example. Let  $\mathcal{S}$  denote the set of stays (ICU admissions in our running example) and  $\mathcal{V}$  the set of variables of interest, such as heart rate (HR), blood pressure, lactate, and glucose. For each ICU stay  $s \in \mathcal{S}$  and each variable  $v \in \mathcal{V}$ , after preprocessing we obtain a time series

$$x_{s,v} = (x_{s,v,1}, \dots, x_{s,v,n_{s,v}}) \in \mathbb{R}^{n_{s,v}},$$

where  $n_{s,v}$  is the number of sampled time points for stay  $s$  on variable  $v$ .

In real systems, these time series are typically irregularly sampled and contain missing values. To focus on the numerical transforms themselves, without entangling interpolation strategies and missingness mechanisms, we adopt the following simplifying convention.

**Assumption: Gridding and alignment.** For each variable  $v$ , we resample all stays on a pre-specified time grid, for example one point per hour. After interpolation and imputation, we concatenate all observations of that variable across stays into a single column vector

$$x_v \in \mathbb{R}^{n_v},$$

where  $n_v$  is the total number of time points for variable  $v$  over the cohort. Analyses on a single stay can be viewed as selecting the corresponding subsequences inside this large vector.

Under this simplified view, the raw dataset can be written as

$$D_{\text{raw}} = \{x_v \in \mathbb{R}^{n_v} : v \in \mathcal{V}\},$$

where each column  $x_v$  represents the time unfolding of one clinical physiologic or laboratory variable (ICU in our running example) over the entire cohort.

We assume a standard hospital-side processing pipeline. Each night, an *EHR-Privacy-Agent* running inside the hospital intranet extracts the latest batch of stays from the production system and forms an incremental view of  $D_{\text{raw}}$ . On an intranet server operating in a CPU-only environment, a family of *column-wise operators* is applied to each variable  $v$ , mapping the raw column  $x_v$  to a perturbed column  $y_v$ . Collecting all perturbed columns yields

$$D_{\text{priv}} = \{y_v : v \in \mathcal{V}\},$$

which is then written into an in-hospital research and teaching cache that can be accessed by clinical researchers, quality analytics teams, and the *EHR-Privacy-Agent* itself. Throughout this process, the original  $D_{\text{raw}}$  remains in a tightly controlled production system, is never exported to the research environment, and is never directly exposed to LLMs or external tools.

The core object studied in this paper is therefore a family of column-wise random operators

$$T_\alpha : \mathbb{R}^{n_v} \rightarrow \mathbb{R}^{n_v}, \quad x_v \mapsto y_v = T_\alpha(x_v; \omega),$$

where  $\alpha \geq 0$  is a unified privacy control parameter and  $\omega$  denotes the internal randomness used by the operator. In what follows, all geometric discussions are carried out in the space of a single column vector  $x_v$ . The multi-variable, multi-stay setting can be understood as repeatedly applying the same operator family to different columns and subsequences.

### 3.2 Column-wise Mean–Variance Manifold: Geometrizing the EHR Transformation Problem

To strike a balance between easy interpretability and resistance to reconstruction, we want each column-wise operator to satisfy two basic intuitions. First, when clinicians or engineers perform EDA and modeling on the perturbed column  $y_v$ , they should still observe scales and fluctuation magnitudes comparable to those of the original data. Second, the operator may induce nontrivial geometric motion in high dimensions, but it should preserve low-order statistics, especially the first and second moments, as much as possible.

To formalize these ideas, we introduce a unified geometric viewpoint, which we refer to as the *mean–variance manifold*. We begin by recalling the basic statistical quantities associated with a column vector.

For any column vector  $x \in \mathbb{R}^n$ , its empirical mean is defined as

$$\mu(x) = \frac{1}{n} \sum_{i=1}^n x_i,$$

which captures the overall level of the signal across time.

Correspondingly, the empirical variance is given by

$$\sigma^2(x) = \frac{1}{n} \sum_{i=1}^n (x_i - \mu(x))^2,$$

measuring the magnitude of fluctuations around the mean. The standard deviation is then defined as

$$\sigma(x) = \sqrt{\sigma^2(x)}.$$

In practice, to ensure numerical stability, we clip extremely small values of  $\sigma(x)$  from below to avoid division by zero or unstable scaling. Based on these quantities, we define the z-score standardized version of  $x$  as

$$z(x) = \frac{x - \mu(x)\mathbf{1}}{\sigma(x)} \in \mathbb{R}^n,$$

where  $\mathbf{1}$  denotes the all-ones vector. This transformation recenters the vector to have zero mean and rescales it to unit variance, effectively removing the original physical units and placing all variables on a common, dimensionless scale.

For any vector  $x$  with  $\sigma(x) > 0$ , the standardized vector  $z = z(x)$  lies in

$$\mathcal{M}(0,1) = \{z \in \mathbb{R}^n \mid \mu(z) = 0, \sigma^2(z) = 1\}.$$

Geometrically, this set can be viewed as the intersection of the zero-mean hyperplane

$$H = \{z \in \mathbb{R}^n \mid \mu(z) = 0\}$$

with the sphere of radius  $\sqrt{n}$ ,

$$S = \{z \in \mathbb{R}^n \mid \|z\|_2 = \sqrt{n}\},$$

so that  $\mathcal{M}(0,1) = H \cap S$ . Thus, after standardization, each clinical time-series column lies on the same high-dimensional manifold with zero mean and unit variance. This viewpoint is useful for two reasons. First, any transform that starts and ends on  $\mathcal{M}(0,1)$  will, after de-standardization, exactly preserve the original column mean and variance. Specifically, if  $z' \in \mathcal{M}(0,1)$ , then

$$y = \mu(x)\mathbf{1} + \sigma(x)z'$$

satisfies

$$\mu(y) = \mu(x), \quad \sigma^2(y) = \sigma^2(x).$$

This provides a natural geometric route to enforce our later C1 constraint.

Second, differences in physical units across variables, such as mmHg, mg/dL, and bpm, are absorbed into the standardization step. In z-score space, every variable is measured on the same dimensionless scale of number of standard deviations, which makes it possible to introduce a single privacy knob  $\alpha$  across all variables.

Accordingly, each column-wise operator  $T_\alpha$  can be decomposed into three stages. We first standardize the raw column via

$$x \mapsto z(x) \in \mathcal{M}(0,1).$$

We then apply a random transform on the manifold,

$$z \mapsto z' = \tilde{T}_\alpha(z; \omega), \quad \tilde{T}_\alpha : \mathcal{M}(0,1) \rightarrow \mathcal{M}(0,1).$$

Finally, we de-standardize through

$$z' \mapsto y = \mu(x)\mathbf{1} + \sigma(x)z'.$$

The true design freedom lies in the choice of  $\tilde{T}_\alpha$ . The operators T1, T2, T3, as well as the later Q-mix extensions, can all be understood as different realizations of  $\tilde{T}_\alpha$ .

### 3.3 A Unified Privacy Knob $\alpha$ : Controlling $\ell_\infty$ Perturbations in z-Score Space

Once the mean–variance geometry is fixed, we still need a unified privacy scale across variables. The practical question is simple: how many standard deviations of per-point deviation do we allow, on average, in the transformed data. To answer this, we introduce a scalar parameter  $\alpha \geq 0$  and constrain perturbations in z-score space through an  $\ell_\infty$  bound.

For almost all realizations of the internal randomness  $\omega$ ,

$$\|\tilde{T}_\alpha(z; \omega) - z\|_\infty \leq \alpha.$$

In words, each time point in standardized space may move by at most  $\alpha$  standard deviations. Returning to physical units, any coordinate  $x_i$  in the original column must satisfy

$$|y_i - x_i| \leq \alpha \cdot \sigma(x),$$

where  $\sigma(x)$  is the cohort-level standard deviation of that column. Hence,  $\alpha$  can be interpreted as a universal ceiling on per-point deviations, measured in units of standard deviations.

In our early experiments, we adopted a more naive strategy and imposed a fixed maximum deviation `maxdiff` in the original physical space, for example  $\pm 0.5$  or  $\pm 1.0$  in the corresponding units. This quickly revealed two serious problems. For low-variance variables, the same `maxdiff` could correspond to several standard deviations, severely distorting near-constant trajectories and harming interpretability as well as downstream model stability. For high-variance variables, by contrast, the same `maxdiff` amounted to only a tiny z-score shift and provided little additional protection against reconstruction or membership attacks.

These observations show that a uniform physical-space bound leads to highly heterogeneous privacy strength across variables. We therefore abandon that design and instead enforce a unified  $\ell_\infty$  bound  $\alpha$  in z-score space, using number of standard deviations as the sole privacy scale. This choice automatically adapts perturbation strength to each variable’s intrinsic variability, allows privacy–utility trade-offs across variables to be compared along the same  $\alpha$ -axis, and enables a systematic study of what we later call the  $\alpha$ -hierarchy.

Empirically, we observe that as  $\alpha$  increases, reconstruction difficulty and membership proxies for T1 and T2 improve monotonically. At the same time, we also find that simply increasing  $\alpha$  is not always sufficient to produce a qualitative jump in privacy for some especially sensitive variables, which motivates the introduction of Q-mix later in the paper.

### 3.4 Full Design Constraints C1–C4 for Column-wise Operators

Building on the mean–variance geometry and the unified parameter  $\alpha$ , we summarize the engineering and statistical design requirements of our column-wise operators as follows.

#### Design goals: semantics, non-reversibility, and deployability

Before formalizing the constraints C1–C4, we summarize the three high-level design goals that motivate them.

**G1: Semantic and statistical faithfulness.** Transformed data should preserve medically meaningful semantics and key cohort-level statistics, so that clinicians and engineers can perform EDA, QA, and downstream modeling on the transformed views almost as they would on the raw data.

**G2: Theoretical non-reversibility under a clear threat model.** Under a specified, realistic threat model, the transformation should prevent exact reversal of protected individual-level information and allow us to reason about privacy-utility trade-offs through a single, interpretable privacy knob.

**G3: Practical deployability on routine hospital infrastructure.** The transformation pipeline must be simple and lightweight enough to run nightly on CPU-only hospital servers, without large generative models or specialized hardware, and produce numeric views that remain directly inspectable by humans.

In the rest of this section, constraints C1–C4 and the threat model C5 formalize these three goals in geometric and algorithmic terms.

**C1: Column-wise mean–variance preservation.** For any variable  $v$ , let  $x_v$  be the original column and  $y_v$  the perturbed column. We require

$$\mu(y_v) = \mu(x_v), \quad \sigma^2(y_v) = \sigma^2(x_v)$$

to hold numerically up to machine precision. Geometrically, this means moving on the mean–variance manifold and then de-standardizing.

**C2: Unified z-score  $\ell_\infty$  bound  $\alpha$ .** For the standardized vector  $z_v = z(x_v)$ , the operator  $\tilde{T}_\alpha$  must satisfy

$$\|\tilde{T}_\alpha(z_v; \omega) - z_v\|_\infty \leq \alpha,$$

with the same  $\alpha$  shared across all variables as the single privacy knob.

**C3: Full variability.** To avoid pseudo-anonymization patterns in which only a small subset of points is perturbed while most points remain unchanged, we require that for the overwhelming majority of time points, the transformed series differs from the original in at least one coordinate. Intuitively, most points in a time series should actually move.

**C4: CPU-friendly and streaming complexity.** From an engineering standpoint, each column-wise operator should have computational complexity  $O(n_v)$  or  $O(n_v \log n_v)$  with a small constant factor, so that nightly jobs over hundreds of thousands of stays remain feasible in a CPU-only environment. Ideally, the operator should also admit a streaming implementation, enabling possible near-real-time extensions.

Together, conditions C1 through C4 define the feasible design space for the family of operators studied in this paper. The fundamental operators, T1, T2, and T3, along with the later Q-mix extensions, are all required to meet these conditions. However, for Q-mix, a slightly relaxed interpretation of C4 is adopted, as it is applied only to a limited subset of high-risk variables, allowing for some flexibility in its implementation while still maintaining robust privacy guarantees.

### 3.5 Threat Model C5: No-key, Structure-aware Adversary and L0/L1/L2

Having specified the operator space, we now clarify the class of attackers that we consider to be within scope. Our goal is not to construct a formally complete cryptosystem, but rather to design one-way numerical transformations that, under a realistic yet relatively strong threat model, prevent exact recovery of protected individual-level information and substantially degrade the success of reconstruction- and membership-type attacks compared with using the raw data.

#### 3.5.1 Kerckhoffs’s Principle and the No-key Assumption

For the numerical transformation pipeline implemented by the EHR-Privacy-Agent, we adopt a transparency assumption analogous to Kerckhoffs’s principle in cryptography. In our setting, the adversary is assumed to know the form of the operator family, including the matrix formulations and pseudo-code of T1, T2, T3, and Q-mix, as well as the end-to-end transformation process. Public hyperparameters are also assumed to be known, including  $\alpha$ , window lengths, Q-mix dimensions, and which variables have Q-mix enabled.

At the same time, the system does not rely on a long-term shared key. Internally, the operators may still use pseudo-random number generators and seeds, for example when constructing a per-stay, per-variable orthogonal matrix  $Q_{s,v}$  from a tuple such as (hospital\_internal\_seed,  $s, v$ ). However, these seeds are treated as one-time secrets confined to the hospital computing environment. They exist only inside the in-hospital pipeline, are never exposed through external interfaces, exported files, or logs, and cannot be reliably inferred or reused by an adversary even if some paired ( $D_{\text{raw}}, D_{\text{priv}}$ ) samples are leaked.

We therefore refer to the adversary as a *no-key, structure-aware adversary*. Such an adversary fully understands the structure and implementation of the operator family, but does not have access to the internal seeds or one-time randomness used in the hospital pipeline. This should be distinguished from traditional encryption with a fixed long-term key. Our goal is not to build a reversible encryption mechanism, but rather a one-way, single-use numerical transformation pipeline. In this sense, no-key means that we do not assume or provide a reusable long-term symmetric key abstraction, even though internal randomness is still present.

#### 3.5.2 Leakage Levels: L0 / L1 / L2

Under the no-key assumption, the adversary’s power depends crucially on how many input–output pairs can be observed. Let  $x$  denote an original column vector or subsequence and  $y = T_\alpha(x; \omega)$  the corresponding perturbed result. We consider three leakage levels.

At level L0, the adversary observes only many perturbed columns or time series  $\{y_v\}$ , without any direct access to the corresponding originals  $\{x_v\}$ . This models external researchers or third parties who only see the released privacy-enhanced data. At level L1, the adversary can access a small number of paired samples  $(x, y)$ , on the order of 0.01% of stays or time points, corresponding to situations such as sporadic internal leaks, manual spot checks, or accidentally exposed audit samples. At level L2, the adversary can observe a substantial fraction of paired samples, for example about 20% of stays or time points, which reflects a stronger insider scenario or a multi-center setting in which one party has access to both raw and privacy-enhanced views. Across these leakage levels, we focus on four classes of attack tasks. The A-family covers pointwise and sequence reconstruction, where the goal is to predict  $x$  or key statistics derived from  $x$  given  $y$ . The B-family concerns record linkage and re-identification, where an attacker uses an external raw record  $x^{\text{ext}}$  to identify the most likely matching record in  $\{y\}$ . The C-family addresses membership inference, namely deciding whether a particular individual’s data appear in  $\{x\}$  or contributed to the privacy-enhanced release (Shokri et al., 2017; Zhang et al., 2022). The D-family concerns attribute inference and indistinguishability-style games, for example when the adversary is given  $(x_0, x_1)$  and  $y = T_\alpha(x_b)$  and must infer the hidden bit  $b$ , in analogy with IND-style formulations in cryptography (Annamalai et al., 2024).

In this paper, we mainly instantiate A-family reconstruction attacks in single-column experiments and use membership proxies as approximate indicators for C-family risks (Carlini et al., 2021; Shokri et al., 2017). A complete treatment of the B/C/D families, as well as the fully multivariate setting, is left for future work.

From a cryptographic viewpoint, our reconstruction and membership attacks can be regarded as simplified chosen-plaintext-style evaluations. Depending on the leakage level, the adversary may access some number of  $(x, y)$  pairs and attempts to infer  $x$  or some sensitive function of  $x$  from  $y$ . We do not claim security in the strict IND-CPA or IND-CCA sense. Rather, these attacks serve as empirical lower bounds on privacy risk within the chosen adversarial model.

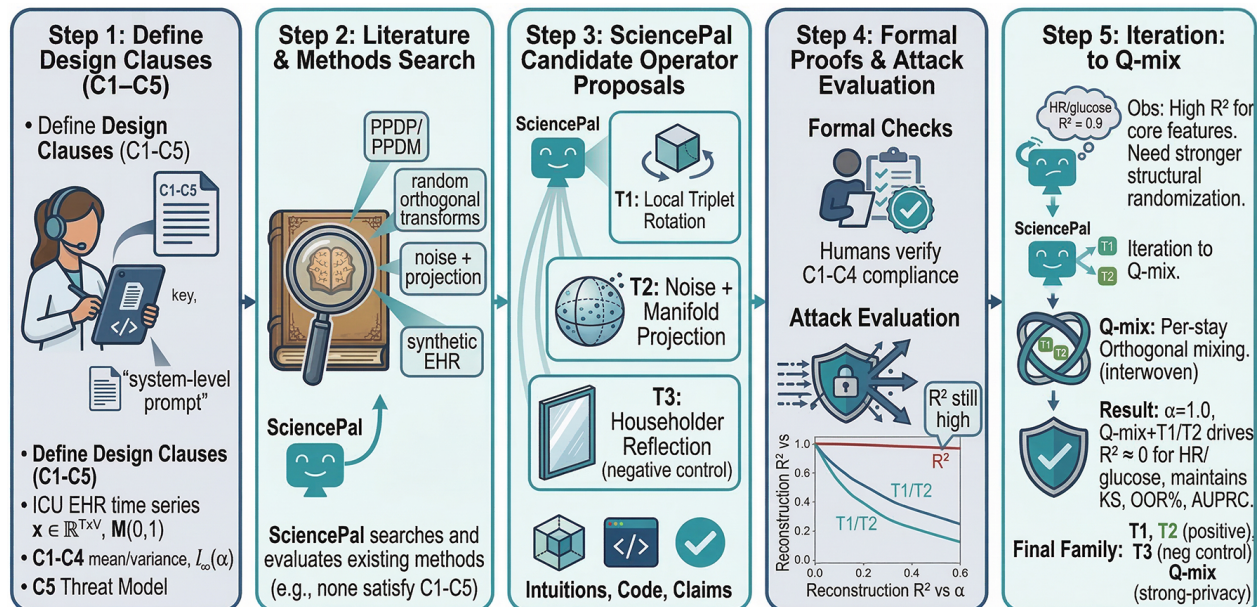


Figure 1: SciencePal co-design protocol for geometric operator families. **Step 1:** Humans specify operator clauses C1–C4 and threat model C5. **Step 2:** SciencePal searches PPDP/PPDM and related methods, finding no operator that satisfies all clauses. **Step 3:** SciencePal proposes candidate operators T1, T2, and T3. **Step 4:** Humans prove properties and run attack-based evaluation, keeping T1/T2 and rejecting T3. **Step 5:** Observing residual high reconstruction risk for some variables, humans and SciencePal co-design per-stay Q-mix extensions, yielding the final operator family.

### 3.6 Formal Problem Statement

We can now summarize the **central problem** of this paper.

**Problem: Column-wise geometric operator design.** Given a structured EHR dataset  $D_{\text{raw}}$  (we use ICU time-series EHR data as a running example), the column-wise operator design constraints C1–C4, and the no-key, structure-aware threat model C5, design a family of random operators  $\{T_\alpha\}_{\alpha \geq 0}$  such that, under leakage levels L0/L1/L2 and for selected attack families, in particular A-family reconstruction and membership proxies, the adversary’s success rate in recovering protected individual-level information is substantially worse than when using the raw data, while simultaneously preserving downstream task performance within an acceptable utility range and maintaining deviations in column-wise distributional shape, multivariate correlation structure, and temporal structure at levels that remain interpretable and suitable for clinicians and engineers performing EDA and QA.

We next describe a SciencePal co-design protocol that explains how these operators are proposed, filtered, and iteratively refined through a loop in which humans specify constraints, the AI assistant SciencePal proposes candidate tools, and humans then verify and attack the resulting designs.

## 4 SciencePal Co-design / AI-making Protocol

As discussed in Section 9, we did not find any existing column-wise operator family in the literature that simultaneously satisfies C1–C4 and C5. This motivates an explicit SciencePal co-design workflow, in which the AI assistant SciencePal is treated as a constrained tool-builder rather than an autonomous decision-maker. In this section, we formalize that SciencePal co-design / AI-making protocol. The overall five-step protocol is summarized in Figure 1.

### 4.1 Step 1: Human Specification of Geometric and Engineering Requirements

The process begins with human researchers formulating a precise operator-design specification based on structured EHR use cases (instantiated on ICU data) and hospital engineering constraints. This specification includes data and compute requirements, namely that data remain strictly inside the hospital intranet,

nightly jobs must run in a CPU-only environment, and operators must not depend on large generative models or GPU inference. It also includes the geometric and statistical constraints C1–C3, namely exact preservation of column-wise mean and variance, unified  $\ell_\infty$  control in z-score space through  $\alpha$ , and full variability so that most points are genuinely perturbed. In addition, the specification includes the complexity requirement C4, which asks for  $O(n_v)$  or near- $O(n_v)$  algorithms with small constants and, where possible, streaming implementations. Finally, it includes the threat model C5, under which the adversary is no-key and structure-aware, and the operators are expected to offer meaningful protection under L0/L1/L2 leakage against at least a subset of the A/B/C/D attack families.

This specification is written as a mixture of natural language and mathematical notation in the form of operator-design clauses and is then used as a system-level prompt for subsequent interactions with SciencePal.

#### **4.2 Step 2: SciencePal Literature Search and Candidate Operator Proposals**

Given this specification, SciencePal is asked to perform two tasks. The first is literature search. It surveys the PPDP/PPDM, random orthogonal transform, noise-plus-projection, time-series privacy, and synthetic EHR literature for operator families that might already satisfy C1–C4 while remaining compatible with structured EHR (including ICU time-series data) and the mean–variance manifold perspective. This search concludes that, although many related ingredients exist, including random orthogonality, Householder reflections, and noise-plus-normalization schemes, no off-the-shelf method fully fits the deployment constraints once CPU-only execution and a unified  $\alpha$  knob are imposed. The second task is candidate operator design. After establishing the lack of a fully compatible existing scheme, SciencePal is prompted to propose new operator families under the given specification. These proposals include geometric intuitions on the mean–variance manifold, explicit mathematical forms and sufficient conditions such as orthogonality and projection steps, pseudo-code level implementation sketches, and self-declared claims regarding C1–C4. At this stage, several candidate structures are proposed, of which three representative families eventually evolve into the basic operators T1, T2, and T3.

#### **4.3 Step 3: Human Geometric Proofs and First-stage Filtering**

In the third stage, human researchers act as reviewers and carry out formal geometric and statistical analysis of the candidate operators proposed by SciencePal. This includes checking whether each manifold-based definition is self-consistent, deriving its effects on column-wise means and variances to verify C1, analyzing perturbation norms in z-score space and their dependence on  $\alpha$  to verify C2, and evaluating whether the operator can be implemented in  $O(n_v)$  or  $O(n_v \log n_v)$  time with possible streaming support to verify C4.

Candidates that clearly violate C1–C4, for example by introducing uncontrolled nonlinearities or breaking mean/variance preservation in corner cases, are discarded. Candidates with plausible geometric and computational properties are retained for attack-based evaluation. In this paper, the three retained basic operators are T1, a local triplet rotation; T2, a noise-plus-projection transform onto the mean–variance manifold; and T3, a global Householder reflection that is ultimately kept as a negative case.

#### **4.4 Step 4: Attack-driven Evaluation and Positive/Negative Labeling**

In the fourth stage, the surviving candidates are implemented on real ICU time-series EHR data. The evaluation spans three dimensions. First, we measure geometric and statistical fidelity through numerical errors in column-wise means and variances, as well as metrics such as  $1 - \text{KS}$ , Frobenius distance between correlation matrices, autocorrelation functions (ACFs), and Ljung–Box tests. Second, we examine downstream utility by tracking changes in AUROC and AUPRC for several ICU prediction tasks. Third, we assess resistance to attacks through reconstruction experiments and membership proxies under L0/L1/L2 leakage.

These experiments allow us to label operators as either positive or negative cases from a privacy perspective. T1 and T2 emerge as positive cases: for moderate  $\alpha$ , they preserve means, variances, and correlation structure almost perfectly while substantially increasing the difficulty of reconstruction and membership attacks. T3, by contrast, becomes a negative case. Although it appears nearly perfect on conventional statistical metrics, including means, variances, correlations, and ACFs, it remains highly invertible under L2 combined with A-family linear reconstruction attacks, with  $R^2$  close to 1. We therefore regard T3 as suitable only for very light perturbation or didactic in-hospital use, but not for strong-privacy external release.

Such negative cases are themselves important outputs of the AI-making process. They show that geometric elegance and statistical similarity alone are insufficient. Privacy claims must be tested explicitly through attack experiments.

#### 4.5 Step 5: Iteration and Extension: From the $\alpha$ -Hierarchy to Q-mix

After the initial operator family T1/T2/T3 and its  $\alpha$ -hierarchy had been established, our single-column attack experiments revealed an important phenomenon. As  $\alpha$  increases, the  $R^2$  of T1 and T2 under A-family reconstruction decreases monotonically, but for some especially sensitive variables, particularly HR and glucose, the  $R^2$  values can still remain in the range 0.6 to 0.9 even when the marginal distributions already show visibly substantial shifts. In other words, privacy improves gradually but does not exhibit a qualitative jump. This observation triggered a new round of SciencePal co-design. Human researchers sharpened the requirement by asking whether, while keeping  $\alpha$ , C1–C4, and the basic T1/T2 structures unchanged, it would be possible to add a stronger structural randomization mechanism for a small subset of high-risk variables so that reconstruction  $R^2$  under L2 and A-family attacks would drop close to zero. In response, SciencePal proposed several forms of per-stay orthogonal mixing. Building on these ideas, we designed and implemented a per-stay orthogonal Q-mixing extension: for each stay  $s$  and variable  $v$ , a  $48 \times 48$  orthogonal matrix  $Q_{s,v}$  is constructed, applied to local time windows to mix coordinates, and then combined with T1 or T2. The human team subsequently proved that Q-mix satisfies C1–C4 in the slightly relaxed deployment sense noted earlier. With  $\alpha = 1.0$  unchanged, Q-mix combined with T1 or T2 can reduce the  $R^2$  of HR and glucose reconstruction under L2 plus linear A-family attacks to values close to zero, while keeping distributional shape and downstream predictive performance within acceptable ranges.

It is important to emphasize that Q-mix is not a new basic operator family. Rather, it is a deployment-level per-stay orthogonal extension module that is enabled only for a small subset of sensitive variables in strong-privacy scenarios such as external release or multi-center sharing. For most in-hospital research and teaching settings, the default remains T1 or T2, with optional light T3 only for very mild perturbation.

In this sense, the SciencePal co-design / AI-making protocol not only yields the three basic operators T1, T2, and T3, but also reveals the limitations of the pure  $\alpha$ -hierarchy and motivates Q-mix as a stronger privacy extension. The protocol itself is therefore one of the methodological contributions of the paper.

### 5 Operator Families: Column-wise T1/T2/T3 and Per-stay Q-mix Extensions

#### 5.1 Design Guide and Notation

We summarize the geometry, privacy, and utility trade-offs of the four operators in Figure 2.

For convenience, throughout this section we fix a single variable  $v$  and omit its subscript. We therefore work with a single column vector  $x \in \mathbb{R}^n$ , its standardized form

$$z = z(x) = \frac{x - \mu(x)\mathbf{1}}{\sigma(x)} \in \mathcal{M}(0, 1),$$

and a randomized operator in standardized space of the form

$$z' = \tilde{T}_\alpha(z; \omega), \quad z, z' \in \mathcal{M}(0, 1),$$

where  $\omega$  denotes the internal randomness. The corresponding operator in the original physical space is

$$T_\alpha(x; \omega) = \mu(x)\mathbf{1} + \sigma(x)\tilde{T}_\alpha(z(x); \omega).$$

Under this formulation, C1 is automatically satisfied as long as  $\tilde{T}_\alpha$  maps  $\mathcal{M}(0, 1)$  back to itself. The remaining constraints, namely C2 through C4, depend on the specific construction of  $\tilde{T}_\alpha$ .

We next introduce three basic operator families. T1 performs local triplet rotations, T2 applies noise followed by projection, and T3 is a global Householder reflection that serves as a negative case. We then introduce Q-mix as a per-stay orthogonal extension that wraps around T1 and T2.

#### 5.2 T1: Local Triplet Rotation

##### 5.2.1 Intuition

T1 performs local, low-dimensional, small-angle random rotations along the time axis. The aim is to scramble fine-scale temporal patterns while preserving local temporal structure, such as short-range autocorrelation, together with global mean and variance. Concretely, the standardized vector  $z \in \mathbb{R}^n$  is partitioned into disjoint windows of length three, and a random orthogonal transformation is applied within each three-dimensional subspace.

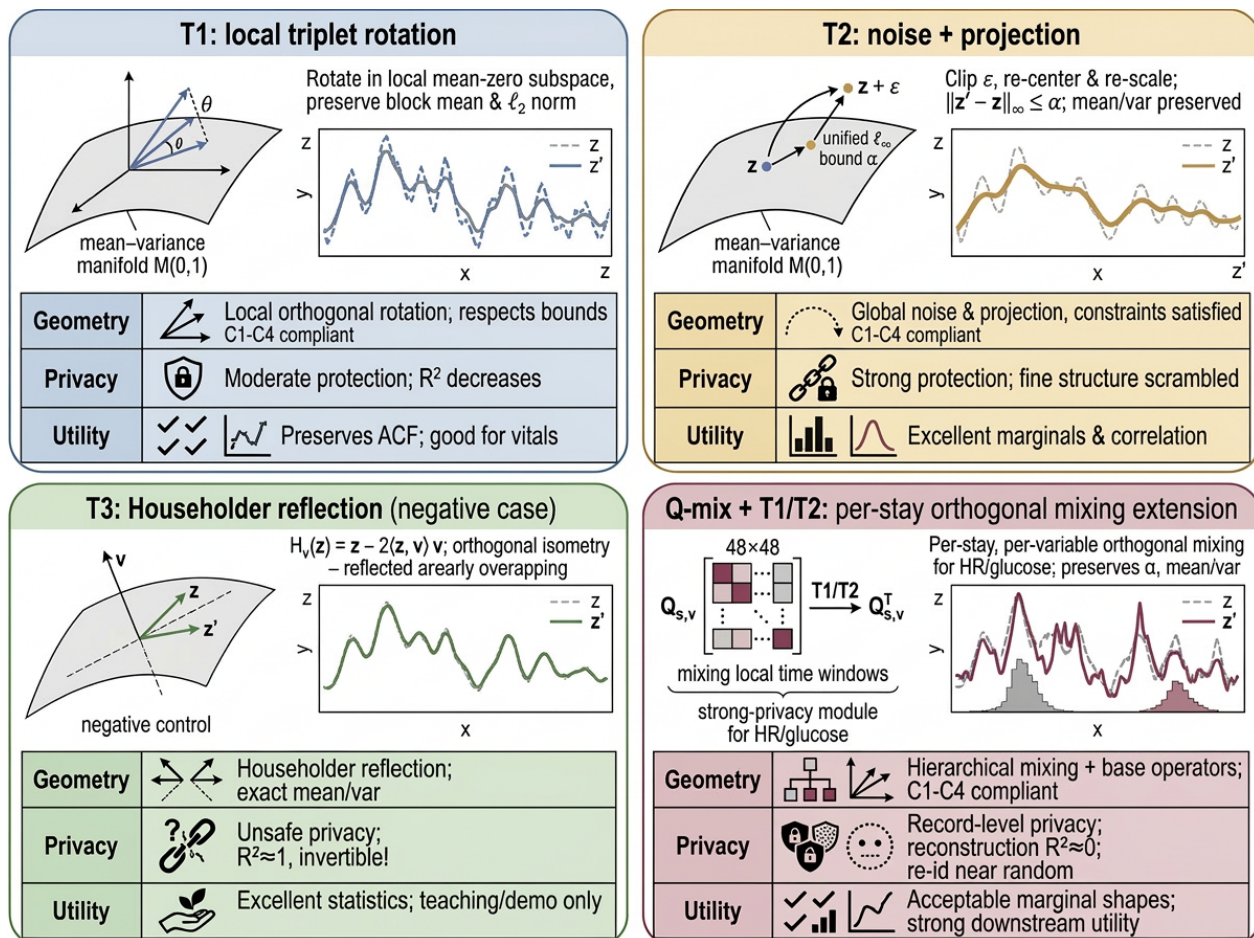


Figure 2: Overview of the column-wise geometric operators studied in this work. **T1** applies local triplet rotations on  $\mathcal{M}(0,1)$ , preserving mean/variance and short-range autocorrelation with moderate privacy. **T2** adds bounded z-score noise with global  $\ell_\infty$  limit  $\alpha$ , then recenters to  $\mathcal{M}(0,1)$ , giving stronger privacy while largely preserving marginals and correlations. **T3** is a global Householder reflection that preserves low-order statistics but is highly invertible ( $R^2 \approx 1$ ), and serves as a negative control. **Q-mix** wraps T1/T2 with per-stay orthogonal mixing on selected high-risk variables, keeping fixed while sharply reducing reconstruction risk and retaining acceptable utility.

## 5.2.2 Algorithm

Let the column length be  $n$ , and partition the index set into triplets

$$B_1 = \{1, 2, 3\}, B_2 = \{4, 5, 6\}, \dots$$

For a final segment with fewer than three points, one may either replicate neighboring points or use a reduced-size rotation; this has negligible effect on C1 and C2 and is omitted here for brevity.

For each triplet  $B$ , define the local vector  $z_B = (z_i)_{i \in B} \in \mathbb{R}^3$ . We first compute its local mean  $\mu_B = \frac{1}{3} \sum_{i \in B} z_i$  and decompose

$$z_B = \mu_B \mathbf{1}_3 + r_B, \quad \mathbf{1}_3 = (1, 1, 1)^\top, \quad \mathbf{1}_3^\top r_B = 0.$$

Thus  $r_B$  lies in the two-dimensional subspace orthogonal to  $\mathbf{1}_3$ . Let  $\{u_1, u_2\}$  be an orthonormal basis of this subspace and write  $r_B = a_1 u_1 + a_2 u_2$ . We then sample

$$\theta_B \sim \text{Unif}[-\theta_{\max}, \theta_{\max}]$$

and rotate the coefficient pair  $(a_1, a_2)$  in the plane:

$$\begin{pmatrix} a'_1 \\ a'_2 \end{pmatrix} = \begin{pmatrix} \cos \theta_B & -\sin \theta_B \\ \sin \theta_B & \cos \theta_B \end{pmatrix} \begin{pmatrix} a_1 \\ a_2 \end{pmatrix}.$$

The transformed block is then reconstructed as

$$z'_B = \mu_B \mathbf{1}_3 + a'_1 u_1 + a'_2 u_2.$$

Applying this construction to all triplets yields a perturbed vector  $z' \in \mathbb{R}^n$ . Since each local transform preserves both the block mean and the block norm, the global mean of  $z'$  remains zero and the global  $\ell_2$  norm remains  $\sqrt{n}$ . Hence  $z' \in \mathcal{M}(0, 1)$ . At the same time, the relative magnitudes and phases inside each triplet are rotated into new configurations, which perturbs higher-order local temporal patterns.

### 5.2.3 Satisfying C1–C4

T1 satisfies C1 because it maps  $\mathcal{M}(0, 1)$  to itself. To enforce C2, we calibrate  $\theta_{\max}(\alpha)$  offline so that for any triplet input  $z_B$  and any admissible angle  $\theta \in [-\theta_{\max}, \theta_{\max}]$ , the local perturbation satisfies  $\|z'_B - z_B\|_\infty \leq \alpha$ . In practice, this is done through analytic bounds combined with numerical search over representative triplet geometries. Once  $\theta_{\max}(\alpha)$  is fixed, the full-column perturbation also satisfies  $\|z' - z\|_\infty \leq \alpha$ .

T1 also satisfies C3. Whenever  $\theta_B \neq 0$ , at least one component of the residual vector changes, so  $z'_B \neq z_B$ . Since  $\theta_B$  is sampled from a continuous distribution, the probability of drawing exactly zero is negligible, and almost all non-degenerate triplets are perturbed. Finally, T1 satisfies C4 because each triplet requires only constant-size vector operations and one  $2 \times 2$  rotation, yielding overall  $O(n)$  complexity with a small constant and a natural streaming implementation.

## 5.3 T2: Noise plus Projection

### 5.3.1 Intuition

Where T1 emphasizes local geometric perturbations, T2 acts more like a global but controlled noise injection followed by a projection back onto the mean–variance manifold. The idea is to add bounded perturbations in z-score space and then restore the output to zero mean and unit variance.

### 5.3.2 Algorithm

Given  $z \in \mathcal{M}(0, 1)$ , we sample Gaussian noise

$$\varepsilon \sim \mathcal{N}(0, \tau^2 I_n)$$

and center it by subtracting its empirical mean, yielding

$$\varepsilon^{(0)} = \varepsilon - \mu(\varepsilon) \mathbf{1}.$$

We then clip its coordinates using a threshold  $c(\alpha)$ ,

$$\varepsilon_i^{(1)} = \text{clip}(\varepsilon_i^{(0)}, -c(\alpha), c(\alpha)),$$

so that  $\|\varepsilon^{(1)}\|_\infty \leq \alpha/2$ . Defining  $\tilde{z} = z + \varepsilon^{(1)}$ , we project back to  $\mathcal{M}(0, 1)$  by re-centering and renormalizing:

$$\tilde{z}^{(0)} = \tilde{z} - \mu(\tilde{z}) \mathbf{1}, \quad z' = \sqrt{n} \frac{\tilde{z}^{(0)}}{\|\tilde{z}^{(0)}\|_2}.$$

By construction, the output  $z'$  lies on  $\mathcal{M}(0, 1)$ . In practice, for a given  $\alpha$ , the parameters  $(\tau, c(\alpha))$  are calibrated offline and then validated numerically in both single-column and multi-column experiments.

### 5.3.3 Satisfying C1–C4

C1 follows immediately from the final projection step, which enforces zero mean and norm  $\sqrt{n}$ . For C2, the clipping step ensures that the direct noise contribution is bounded by  $\alpha/2$  in  $\ell_\infty$ , while the subsequent re-centering and renormalization introduce only a controlled additional perturbation. During offline calibration, we verify extensively that  $\|z' - z\|_\infty \leq \alpha$  holds for all tested samples, and we choose conservative parameters whenever corner cases approach the boundary.

T2 also satisfies C3 because the injected noise is nonzero on almost all coordinates, and the subsequent re-centering and rescaling further modify nearly every time point. The computational cost is linear in  $n$ , since noise generation, clipping, re-centering, and normalization are all single-pass operations. Hence T2 satisfies C4 and is well suited to CPU-only processing.

## 5.4 T3: Global Householder Reflection (Negative Case)

### 5.4.1 Intuition

T3 applies a single global orthogonal reflection. From a geometric perspective, it is almost ideal: it preserves pairwise distances, inner products, correlations, and most conventional summary statistics exactly or nearly exactly. However, precisely because it is such a clean isometry, it is also highly invertible once enough paired samples are observed.

### 5.4.2 Algorithm

Choose a unit vector  $v \in \mathbb{R}^n$  satisfying  $\|v\|_2 = 1$  and  $\mu(v) = 0$ . The vector may be fixed from a representative cohort, for example as a principal direction, or generated pseudo-randomly from an internal hospital seed and then projected onto the mean-zero hyperplane. Define the Householder reflection (Golub & Van Loan, 2013)

$$H_v(z) = z - 2\langle z, v \rangle v,$$

and set

$$\tilde{T}^{\text{T3}}(z) = H_v(z).$$

Geometrically, this is reflection across the hyperplane  $\{w : \langle w, v \rangle = 0\}$ . Points lying on that hyperplane remain fixed, while the component along  $v$  changes sign.

### 5.4.3 Satisfying C1–C4

Because both  $z$  and  $v$  lie in the mean-zero hyperplane,  $H_v(z)$  also has zero mean. Since Householder reflections are orthogonal, they preserve the norm, so  $H_v(z) \in \mathcal{M}(0, 1)$  and C1 holds.

For C2, note that

$$H_v(z)_i - z_i = -2\langle z, v \rangle v_i.$$

If the entries of  $v$  are bounded by  $|v_i| \leq c_v$ , then

$$\|H_v(z) - z\|_\infty \leq 2\sqrt{n} c_v.$$

Thus choosing  $c_v \leq \alpha / (2\sqrt{n})$  guarantees the desired  $\ell_\infty$  bound. T3 also satisfies C3 except on a measure-zero set where  $\langle z, v \rangle = 0$ , and it satisfies C4 because it requires only one inner product and one coordinate-wise update, both linear-time operations. Despite satisfying C1–C4, T3 behaves as a high-invertibility negative case under the C5 and L2 threat model. In Section 6.6, we show that under L2 with 20% paired samples, its reconstruction  $R^2$  is substantially higher than that of T1 and T2.

## 5.5 Summary of the Three Basic Operators

The three basic operators differ mainly in geometric scope and privacy behavior. T1 performs local rotations and tends to preserve short-range temporal structure relatively well. T2 applies global noise with projection and usually offers stronger scrambling at the same  $\alpha$ . T3 is statistically elegant and almost perfectly structure-preserving, but is also highly invertible and therefore unsuitable for strong-privacy deployment.

Accordingly, T1 and T2 are treated as positive operator families for privacy protection, whereas T3 is retained only as a negative case and as a light-perturbation example for controlled in-hospital use.

## 5.6 Per-stay Orthogonal Q-mixing (Pilot Extension Module)

### 5.6.1 Motivation

Empirically, increasing  $\alpha$  improves privacy gradually, but for some physiologically smooth and sensitive variables, especially HR and glucose, the improvement is not decisive. Even when marginal distributions and autocorrelation functions begin to show visible deviation, reconstruction performance may remain relatively high. This motivates an additional structural randomization mechanism that can induce a more pronounced privacy jump while keeping the same global  $\alpha$ .

### 5.6.2 Construction

Consider a single stay  $s$  and variable  $v$ , with standardized time series  $z_{s,v} \in \mathcal{M}(0, 1)$ . Fix a window length  $m$ , for example  $m = 48$ , and partition the time axis into windows  $B_{s,1}, \dots, B_{s,K_s}$ , each of size  $m$ . For each pair  $(s, v)$ , we construct a permutation matrix  $Q_{s,v} \in \mathbb{R}^{m \times m}$  from an internal hospital seed together with  $(s, v)$ . Since  $Q_{s,v}$  is a permutation matrix, it is orthogonal, preserves the constant vector, and is an  $\ell_\infty$ -isometry.

Applying this block-wise yields a mixed representation

$$\tilde{z}_{s,v} = \text{Qmix}_{s,v}(z_{s,v}),$$

where  $\text{Qmix}_{s,v}$  is block-diagonal with identical blocks  $Q_{s,v}$ . Because the transform is block-orthogonal and preserves constants, it preserves global mean and norm, so  $\tilde{z}_{s,v} \in \mathcal{M}(0, 1)$ .

We then wrap T1 or T2 around this mixed coordinate system. For either basic operator  $\tilde{T}_\alpha$ , the corresponding Q-mix version is

$$\tilde{T}_\alpha^{(Q)}(z_{s,v}) = \text{Qmix}_{s,v}^\top \left( \tilde{T}_\alpha(\text{Qmix}_{s,v}(z_{s,v})) \right).$$

This means that we first permute locally within each window, then apply T1 or T2 in the mixed space, and finally map the result back to the original time index order.

### 5.6.3 Satisfying C1–C4 and Interaction with C5

Q-mix preserves C1 because both the mixing and unmixing operations are orthogonal and preserve constants, while the wrapped operator already maps  $\mathcal{M}(0, 1)$  to itself. It preserves C2 because permutations have operator norm one under  $\ell_\infty$ , so the original bound is inherited unchanged. It also preserves C3, since mixing only redistributes where the perturbation appears once mapped back to the original order, and it preserves C4 because applying  $Q_{s,v}$  or  $Q_{s,v}^\top$  is only a permutation and therefore linear-time.

Under the no-key, structure-aware threat model, the adversary knows the existence and form of Q-mix, including the window length and the fact that a per-stay permutation is used, but does not know the specific realization of  $Q_{s,v}$ . As a result, even if the adversary learns a good approximate inverse for T1 or T2 in the mixed coordinate system, the missing per-stay permutation still prevents straightforward recovery in the original time order.

In the Q-mix pilot experiments of Section 6.7.1, we show that with  $\alpha = 1.0$ , Q-mix combined with T1 or T2 can drive the reconstruction  $R^2$  for HR and glucose under L2 plus linear A-family attacks from the range 0.8 to 0.9 down to nearly 0.

### 5.6.4 Deployment

Q-mix is not a new basic operator family. Rather, it is a deployment-level extension wrapped around T1 and T2. In relatively controlled in-hospital research, QA, or teaching settings, T1 or T2 with a smaller  $\alpha$ , for example  $\alpha = 0.3$  to  $0.5$ , is usually sufficient without enabling Q-mix. In contrast, for external sharing, multi-center analysis, or other stronger-threat scenarios, T1 or T2 with a larger  $\alpha$ , for example  $\alpha = 0.8$  to  $1.0$ , can be combined with Q-mix for a small subset of high-risk variables such as HR and glucose.

In the EHR-Privacy-Agent’s policy design, Q-mix is therefore treated as a strong-privacy module. It is disabled in the default in-hospital configuration and enabled only when constructing stronger privacy views for external release or cross-center sharing, and even then only for designated high-risk variables.

## 6 Experiment I: Single-column Operator Behavior

In this section, we evaluate T1, T2, T3, and the per-stay Q-mix wrapper on MIMIC-IV ICU time series from a single-column perspective. Our goal is twofold. First, we verify on real data that these operators satisfy the geometric constraints C1–C4 introduced in Section 3. Second, we instantiate a concrete privacy evaluation protocol under leakage levels L0, L1, and L2 together with attack families A, B, C, and D. We then examine how reconstruction attacks behave as a function of the privacy knob  $\alpha$ , and show that per-stay Q-mixing can drive the linear reconstruction  $R^2$  for HR and glucose from approximately 0.8–0.9 down to nearly 0 at the same  $\alpha$ , while only mildly affecting marginal distributions and temporal structure.

Throughout this section, we work within the unified mean–variance manifold and  $\alpha$ -hierarchy framework introduced in Sections 3–5. For each column, we first standardize to  $z \in \mathcal{M}(0, 1)$ , apply an operator family in standardized space, and then de-standardize back to physical units.

### 6.1 Experimental Setup and Data Preparation

#### 6.1.1 Dataset and resampling

We use the adult ICU subset of MIMIC-IV (Johnson et al., 2023b). Only first ICU stays are included, and we further restrict the cohort to patients aged at least 18 years with ICU length of stay  $\text{LOS} \geq 24$  hours.

For each ICU stay  $s$ , time is aligned to ICU admission, with  $t = 0$  corresponding to ICU in-time. All charted physiologic variables are resampled onto a 1-hour grid. Concretely, each chart time is converted to an integer hour offset by flooring the difference from ICU admission, after which the data are pivoted into an hourly matrix representation  $\{(s, t) \mapsto \text{value}\}$ . We then restrict attention to the first  $T_{\max} + 1$  hours, using  $T_{\max} = 47$ , so that each retained time series has length approximately 48.

Missingness is handled within each stay and variable by a simple forward-fill plus linear-interpolation strategy. Measurements are first sorted by time and forward-filled along the hourly grid. When long gaps remain, linear interpolation is applied whenever it is clinically sensible. For variables where such interpolation is not meaningful, NaNs may be retained, but in this section we include only columns for which the selected window  $[0, T_{\max}]$  is defined for almost all stays. The resulting stay-level time series is denoted as follows:

$$x_{s,v} \in \mathbb{R}^{n_{s,v}}, \quad n_{s,v} \approx 48.$$

### 6.1.2 Representative variable set

To cover a range of column types, including vitals versus labs, smooth versus spiky variables, and narrow versus heavy-tailed marginals, we select a representative set of variables. The vital-sign group includes HR, systolic and diastolic blood pressure, mean arterial pressure, temperature in Celsius, respiratory rate, and peripheral oxygen saturation. The laboratory group includes glucose, lactate, creatinine, and several additional markers. Together, these variables span different variance scales, physical units, and clinical roles. Our aim is to observe, within a common geometric and privacy framework, how different column types respond to the same operator family.

### 6.1.3 Operators and hyperparameters

On each column, we compare several transform classes. The main geometric operators are T1\_uniform, namely the local triplet rotation of Section 5.2 with a fixed partition into disjoint length-3 blocks; T1\_weighted, a small weighted variant of T1 that adjusts rotation frequency or angle over time while keeping the same privacy structure; T2, the noise-plus-projection operator of Section 5.3; and T3, the global Householder reflection of Section 5.4, which is retained as a negative case.

In Section 6.8, we additionally consider per-stay orthogonal Q-mixing wrappers around T1 and T2, namely  $Q + \text{T1\_uniform}$ ,  $Q + \text{T1\_weighted}$ , and  $Q + \text{T2}$ , focusing on the sensitive variables HR and glucose.

All geometric operators share a common z-score  $\ell_\infty$  privacy bound,

$$\|z' - z\|_\infty \leq \alpha.$$

For the geometric and distributional analyses in Sections 6.2 and 6.3, we use

$$\alpha \in \{0.3, 0.5, 0.8, 1.0\}.$$

Here,  $\alpha = 0.3$  corresponds to a light, visualization-friendly regime, whereas  $\alpha = 1.0$  corresponds to a stronger regime in which each point may move by up to one standard deviation. For reconstruction experiments in Section 6.7, we extend the grid to

$$\alpha \in \{1.0, 2.0, 3.0, 5.0\},$$

in order to probe the limits of the  $\alpha$ -hierarchy.

For sanity checks, we also implement simple baselines such as the identity mapping and i.i.d. Gaussian noise in z-score space.

### 6.1.4 Column-wise standardization and evaluation views

For each variable  $v$ , we compute a global column-wise mean and standard deviation over the training cohort,

$$\mu_v = \mu(x_{\cdot,v}), \quad \sigma_v = \sigma(x_{\cdot,v}),$$

and standardize each stay-level sequence by

$$z_{s,v} = \frac{x_{s,v} - \mu_v \mathbf{1}}{\sigma_v}.$$

An operator is then applied in standardized space to obtain  $z'_{s,v}$ , and the result is mapped back to physical space through

$$x'_{s,v} = \mu_v \mathbf{1} + \sigma_v z'_{s,v}.$$

We evaluate each operator from two complementary views. In standardized space ( $z, z'$ ), we analyze geometric quantities such as  $\ell_\infty$  perturbation, reconstruction  $R^2$ , and z-score MAE. In physical space ( $x, x'$ ), we analyze physical ranges, out-of-range rates, and clinical interpretability.

Table 1: Summary of geometric sanity statistics by operator and evaluation setting. Columns  $\Delta\mu_{\max}$  and  $\Delta\sigma_{\max}$  report the maximum absolute differences in column-wise mean and standard deviation across variables. The remaining columns summarize aggregate  $\ell_{\infty}$  behavior and the maximum fraction of unchanged points. All values are computed over the training cohort and all  $\alpha$  values used in the geometric experiments.

Setting	Operator	$\Delta\mu_{\max}$	$\Delta\sigma_{\max}$	$ \bar{\delta} _{\max}$	$ \delta _{\max,\max}$	Unchanged <sub>max</sub>	$n$
phys	T1_uniform	$5.7 \times 10^{-14}$	$9.1 \times 10^{-13}$	0.999975	0.9999993	0.0000	30
phys	T1_weighted	$5.7 \times 10^{-14}$	$9.1 \times 10^{-13}$	0.999974	0.9999995	0.0098	30
phys	T2	$2.8 \times 10^{-14}$	$9.1 \times 10^{-13}$	0.91211	0.99322	0.0000	10
phys	T3	$4.3 \times 10^{-14}$	$4.6 \times 10^{-13}$	0.25057	0.72993	0.0000	10
z	T1_uniform	$1.8 \times 10^{-17}$	$5.6 \times 10^{-16}$	0.74980	0.9999991	0.0000	60
z	T1_weighted	$2.0 \times 10^{-17}$	$8.9 \times 10^{-16}$	0.74956	0.9999997	0.0079	60
z	T2	$3.6 \times 10^{-17}$	$1.3 \times 10^{-15}$	0.61793	0.90847	0.0000	20
z	T3	$1.1 \times 10^{-17}$	$3.3 \times 10^{-16}$	0.02193	0.04106	0.0000	20

## 6.2 Geometric Sanity Check: Numerical Validation of C1 and C2

We first verify that T1, T2, and T3 satisfy mean-variance preservation and  $\ell_{\infty}$  control on real ICU columns, beyond the idealized derivations of Section 5.

### 6.2.1 Mean and variance preservation (C1)

For each variable  $v$ , we compare original and perturbed column-wise means and standard deviations over all stays through

$$\Delta\mu_v = \mu(x'_{\cdot,v}) - \mu(x_{\cdot,v}), \quad \Delta\sigma_v = \sigma(x'_{\cdot,v}) - \sigma(x_{\cdot,v}).$$

We report maximum absolute deviations over variables and summarize them by operator and evaluation setting, namely physical space versus standardized space.

Table 1 reports these summary statistics for the four geometric operators, aggregated over all  $\alpha$  values used in the geometric sanity experiments. In addition to  $\Delta\mu_v$  and  $\Delta\sigma_v$ , the table includes  $\ell_{\infty}$ -related quantities and the fraction of unchanged points, the latter being relevant for C3. Figure 3 visualizes the  $\log_{10}$ -scale of  $\Delta\mu_{\max}$  together with max\_abs\_delta\_mean across settings and operators, while Figure 4 shows boxplots of  $|\Delta\mu_v|$  and  $|\Delta\sigma_v|$ .

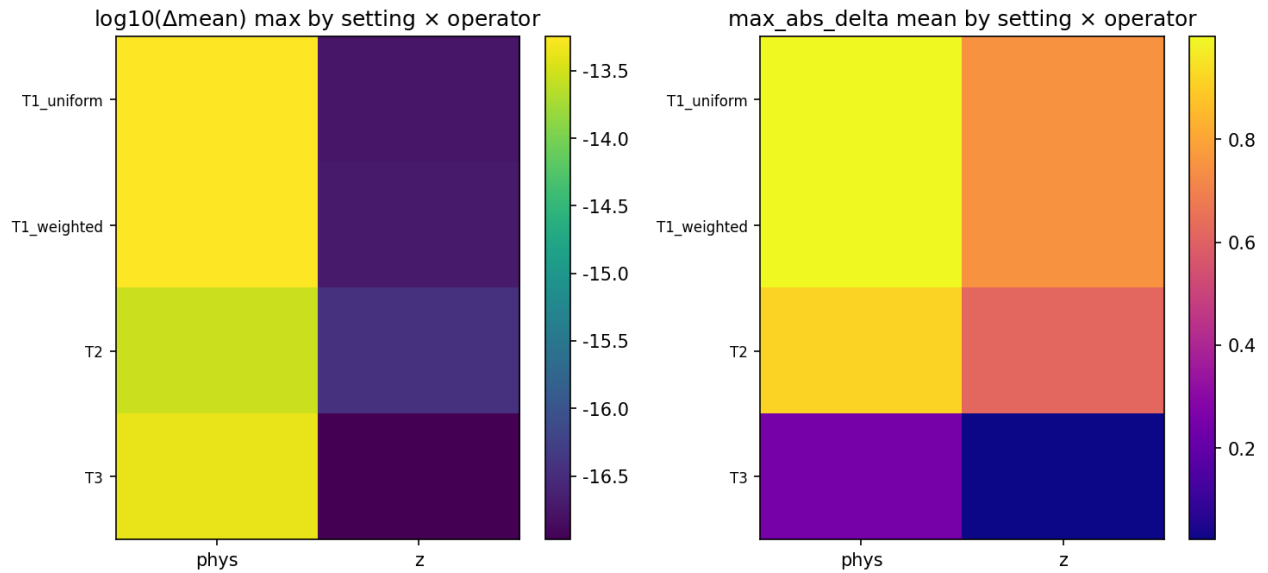


Figure 3: Geometric sanity heatmaps. Left:  $\log_{10}$  of the maximum absolute mean deviation  $\Delta\mu_{\max}$  by setting (phys vs z) and operator. Right:  $\max\_abs\_delta\_mean$  by setting and operator. All geometric operators keep mean deviations at or below machine precision.

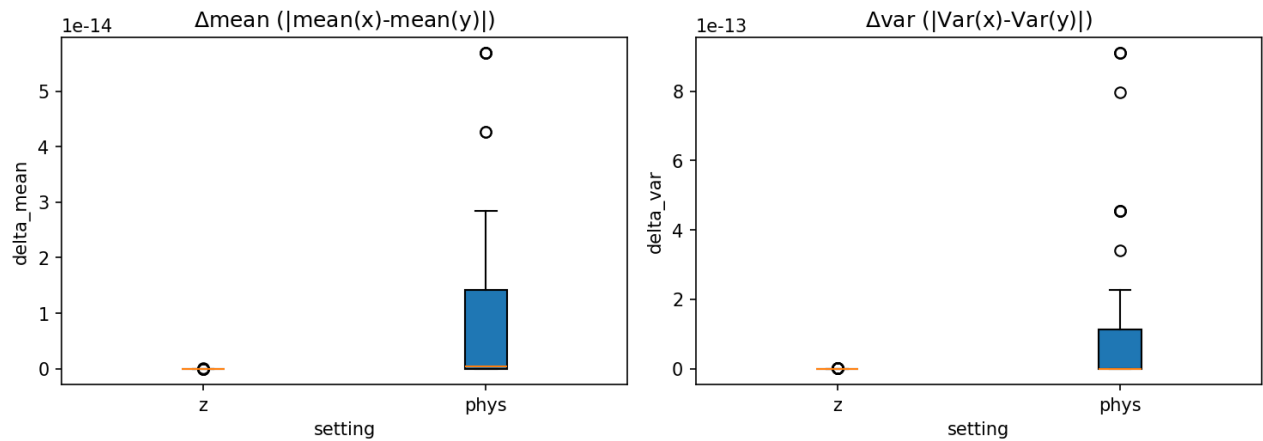


Figure 4: Boxplots of  $|\Delta\mu_v|$  and  $|\Delta\sigma_v|$  grouped by evaluation setting. Deviations in standardized space are essentially at numerical precision; in physical space they remain on the order of  $10^{-13}$ – $10^{-14}$ .

Across all  $\alpha$  values and all operators, the median and 95th percentile of  $|\Delta\mu_v|$  and  $|\Delta\sigma_v|$  remain at  $10^{-6}$  or below, while the global maxima are essentially at machine precision. These results confirm that the geometric constructions of Section 5 are realized with high numerical fidelity on real ICU data, and that the mean–variance manifold is a stable computational domain for all operators.

### 6.2.2 z-score $\ell_\infty$ bound (C2)

For each stay  $s$  and variable  $v$ , we compute the perturbation in standardized space,

$$\delta_{s,v} = z'_{s,v} - z_{s,v}, \quad \|\delta_{s,v}\|_\infty = \max_t |\delta_{s,v}(t)|.$$

For each triple  $(v, \alpha, \text{operator})$ , we summarize the mean, median, and maximum of  $\|\delta_{s,v}\|_\infty$  across stays.

Figure 5 plots the mean  $\|\delta_{s,v}\|_\infty$ , averaged across variables, for  $\alpha = 0.5$  and  $\alpha = 1.0$ .

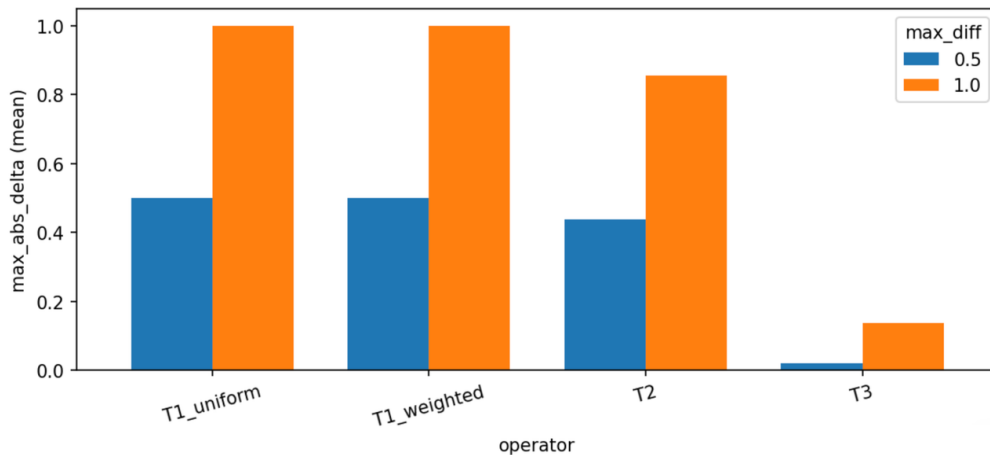


Figure 5: Average z-score  $\ell_\infty$  perturbation  $\|\delta_{s,v}\|_\infty$  by operator for two target bounds  $\alpha = 0.5$  and  $\alpha = 1.0$ . For all T1/T2/T3 operators the empirical maximum  $\|\delta_{s,v}\|_\infty$  never exceeds the configured  $\alpha$ ; the average perturbation typically lies in the  $0.7\text{--}0.9\alpha$  range.

For T1, T2, and T3, the empirical maxima  $\max_s \|\delta_{s,v}\|_\infty$  remain strictly below the configured  $\alpha$  across variables and parameter settings. On more than 99.9% of stays, the realized perturbation magnitude lies slightly below  $\alpha$ , most often in the range  $0.7\alpha\text{--}0.9\alpha$ .

Taken together, these results validate the offline calibration procedures of Section 5, such as  $\theta_{\max}(\alpha)$  for T1 and  $(\tau, c(\alpha))$  for T2, and confirm that the unified  $\alpha$  serves as a robust cross-column privacy knob in practice.

### 6.3 Marginal Distributions and Numeric Ranges

Having established C1 and C2, we next examine how the operators affect single-column marginal distributions and physical numeric ranges.

#### 6.3.1 Marginal distributions and KS distance

For each variable  $v$ , we estimate empirical CDFs of the original and perturbed columns,

$$F_v(t) = \mathbb{P}(x_{\cdot,v} \leq t), \quad F'_v(t) = \mathbb{P}(x'_{\cdot,v} \leq t),$$

and compute the Kolmogorov–Smirnov distance

$$\text{KS}_v = \sup_t |F_v(t) - F'_v(t)|.$$

Figures 6 and 7 summarize  $\text{KS}_v$  across operators and variables at the representative privacy level  $\alpha = 0.8$ .

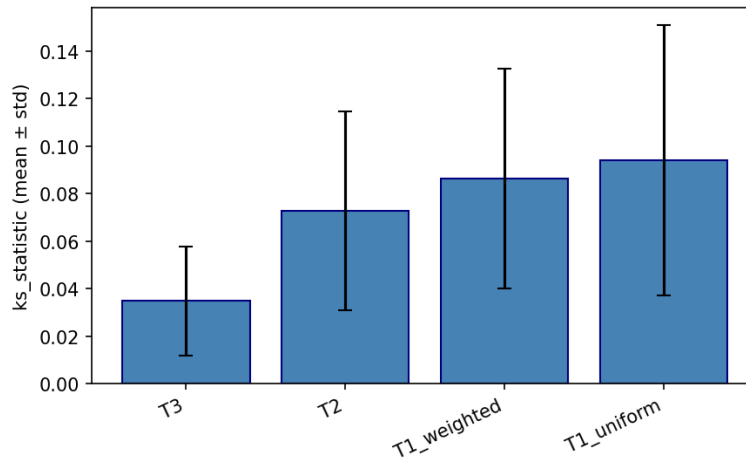


Figure 6: Mean and standard deviation of  $KS_v$  across variables for different operators at  $\alpha = 0.8$  (lower is better distributional fidelity). All three operators keep KS distances small; T3 is the most conservative, followed by T2 and T1.

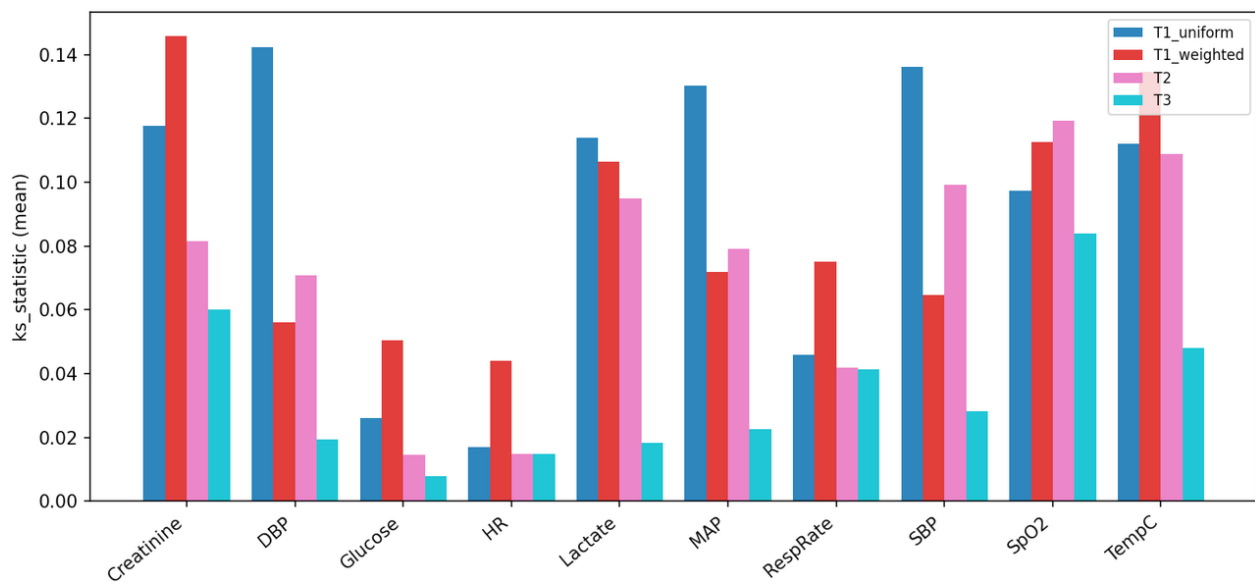


Figure 7: Mean  $KS_v$  by variable and operator at  $\alpha = 0.8$ . For most vitals and labs, T1/T2 keep KS distances below 0.1; heavy-tailed labs experience slightly larger shifts but remain within approximately 0.15. T3 is uniformly closest to the original distribution.

Overall, T1, T2, and T3 exhibit small KS distances for the majority of variables, indicating that marginal distributions are largely preserved. T1 preserves the marginal shape of highly fluctuating vitals and labs such as HR and glucose well, typically with  $KS_v < 0.1$ . For some heavy-tailed labs and a few vitals, such as creatinine and DBP, KS distances increase modestly but remain below approximately 0.14. T2 is slightly more distribution-preserving on lab variables, with its noise-plus-projection mechanism yielding smoother perturbations in the tails. T3 has the smallest KS distances throughout and behaves almost like a marginally isometric transform.

Compared with a Gaussian-noise baseline, T1 and T2 avoid strong tail distortions on heavy-tailed variables at the same nominal  $\alpha$ , highlighting the role of the mean-variance manifold in controlling extremes.

### 6.3.2 Normality checks

For representative variables HR, SBP, and creatinine, we apply the D’Agostino–Pearson normality test (D’Agostino & Pearson, 1973) before and after perturbation, and visualize histograms together with Q–Q plots in standardized space.

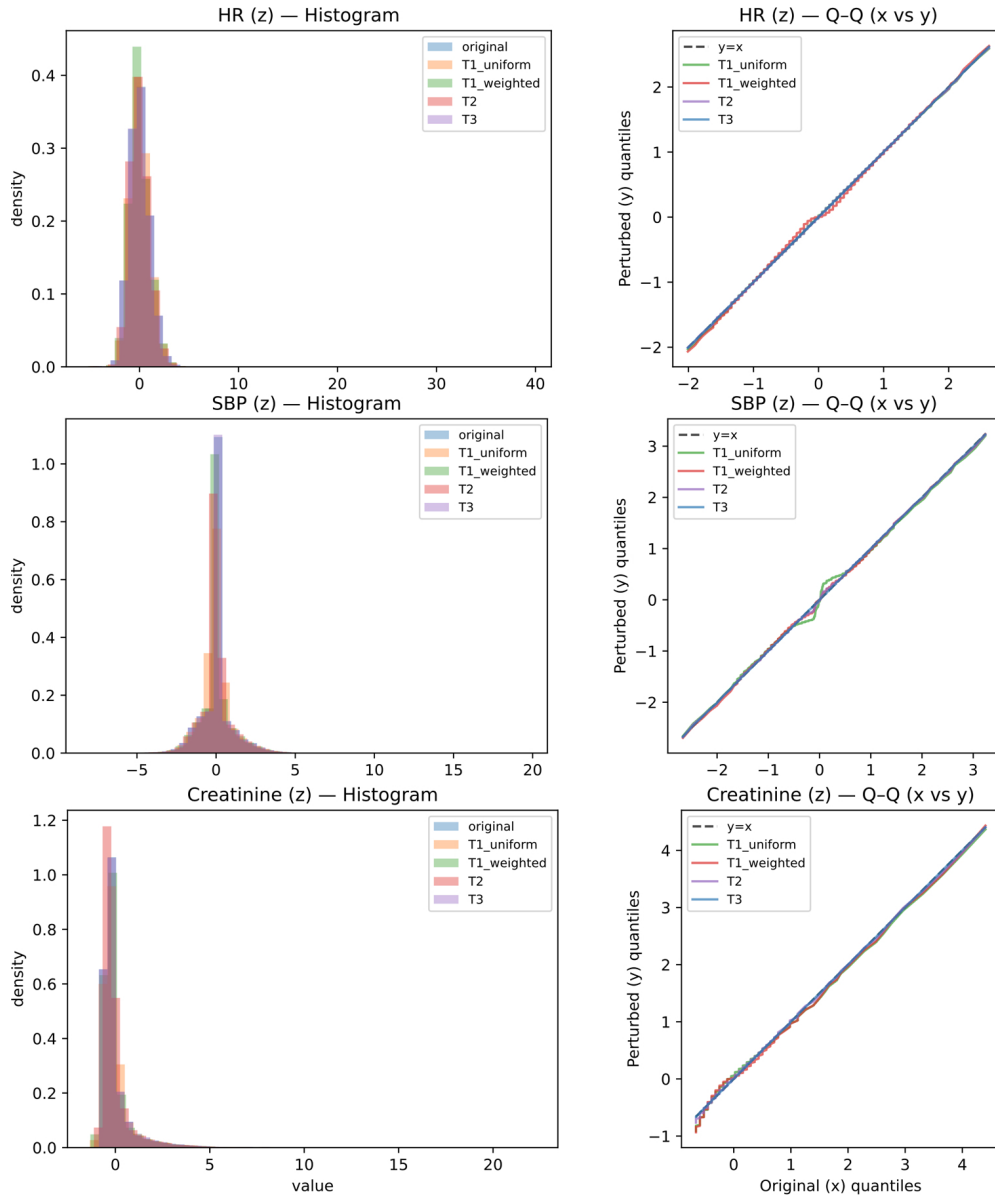


Figure 8: Marginal distributions of SBP, HR, and creatinine in standardized space. For each variable we show the histogram of  $z$  and  $z'$  and the Q–Q plot under T1/T2/T3 at  $\alpha = 0.8$ . All three operators largely preserve the non-Gaussian features of the marginals.

Figure 8 shows that for these three variables, the operators leave the overall shape and deviations from normality essentially unchanged. Formal normality tests confirm that p-values and skewness and kurtosis statistics remain very similar before and after perturbation, in agreement with the small KS distances described above.

### 6.3.3 Physical ranges and out-of-range rates

For each variable  $v$ , we define a clinically reasonable physical range  $[L_v, U_v]$ , for example HR in  $[30, 220]$  bpm, SBP in  $[60, 260]$  mmHg, and glucose in  $[30, 600]$  mg/dL. We then compute the proportion of perturbed samples falling outside this range,

$$\text{OOR}_v = \frac{\#\{x'_{\cdot,v} < L_v \text{ or } x'_{\cdot,v} > U_v\}}{\#\{x'_{\cdot,v}\}}.$$

Figure 9 summarizes out-of-range behavior for HR and glucose at  $\alpha = 1.0$  with Q-mix; full per-variable results for the remaining operators and parameter settings are provided in the supplementary material.

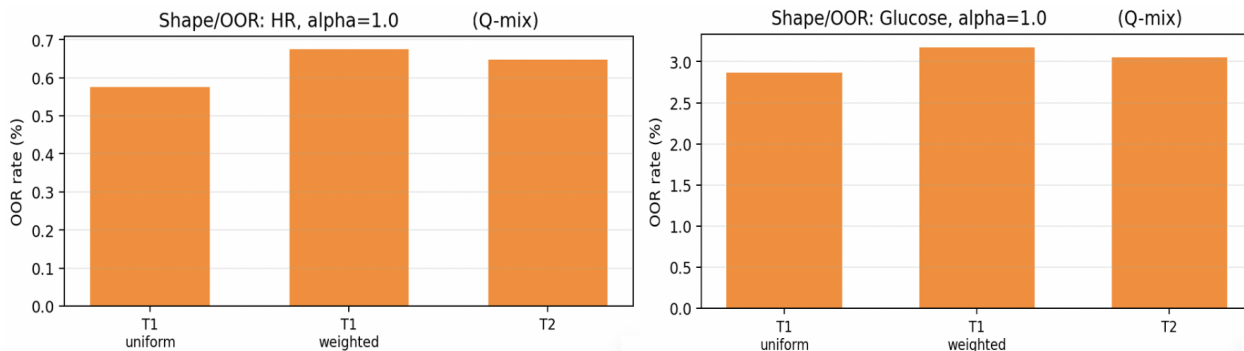


Figure 9: Out-of-range rates  $\text{OOR}_v$  (%) for HR and glucose at  $\alpha = 1.0$  with Q-mix enabled. For HR the OOR remains below 0.7% across operators; for glucose it is around 3%, comparable to the original heavy-tailed distribution.

For  $\alpha \leq 0.5$ , the out-of-range rate remains below 0.5% for almost all variables and is often indistinguishable from the original data. At  $\alpha = 1.0$ , most variables still have  $\text{OOR}_v < 1\%$ , with only a few heavy-tailed variables, such as lactate, showing slightly elevated rates. Compared at similar KS levels, Gaussian-noise baselines induce substantially larger out-of-range rates, especially for high-variance variables, further demonstrating the benefit of  $\ell_\infty$ -controlled geometric perturbations.

## 6.4 Multi-column Correlation and Temporal Structure

We next study how the operators affect multivariate correlation structure and temporal dependence.

### 6.4.1 Multi-column correlation matrices

For each stay  $s$ , let

$$x_s = (x_{s,v_1}, \dots, x_{s,v_k})$$

denote the multivariate vector over selected variables. We estimate cohort-level correlation matrices for the original and perturbed data,

$$R = \text{Corr}(x_{\cdot,\cdot}), \quad R' = \text{Corr}(x'_{\cdot,\cdot}),$$

and quantify their discrepancy using the Frobenius norm

$$\Delta_{\text{corr}} = \|R' - R\|_F.$$

Figure 10 visualizes two representative variable pairs, HR versus SBP and SBP versus DBP, before and after applying each operator at  $\alpha = 1.0$ .

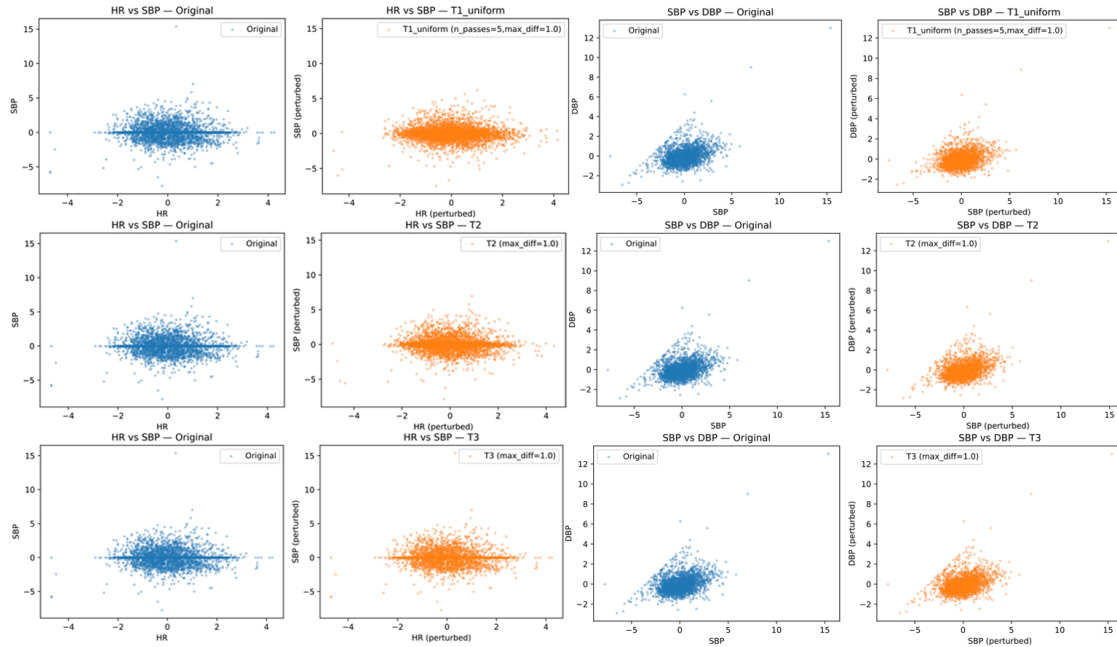


Figure 10: Scatter plots of key variable pairs in standardized space. Top: HR vs SBP (original, T1, T2, T3). Bottom: SBP vs DBP (original, T1, T2, T3). All operators preserve the overall correlation pattern; T3 is almost visually indistinguishable from the original.

Across 24-hour snapshots of multivariable data, all three operators produce correlation matrices that remain extremely close to the original, with discrepancies typically dominated by sampling variability. As expected, T3, being a global orthogonal isometry, almost perfectly preserves the original correlations. T2 is slightly more stable in correlation space than T1, while T1 injects somewhat more localized variation but still maintains the main dependencies.

### 6.4.2 Temporal structure: ACF, Ljung–Box, and Welch PSD

We analyze temporal dependence using autocorrelation functions, Ljung–Box tests (Ljung & Box, 1978), and power spectral density estimates.

For each stay  $s$  and variable  $v$ , we compute lag- $k$  autocorrelations

$$\text{ACF}_{s,v}(k) = \text{Corr}(x_{s,v}(t), x_{s,v}(t+k)), \quad k = 1, \dots, K,$$

and aggregate them across stays. Partial autocorrelations are computed analogously. Figure 11 shows ACF and PACF for HR and SBP under different operators.

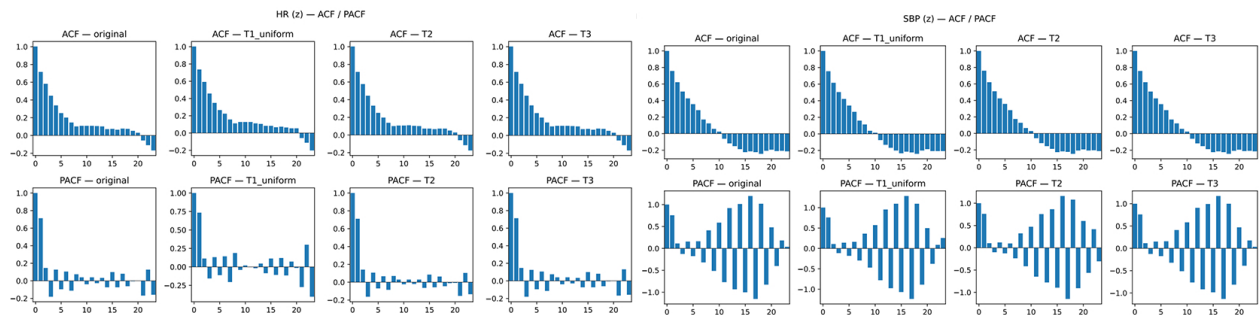


Figure 11: ACF and PACF of HR and SBP in standardized space for the original data and after applying T1/T2/T3 at  $\alpha = 1.0$ . T1/T2 introduce mild attenuation in higher lags but retain the overall temporal dependence shape; T3 leaves ACF/PACF almost unchanged.

To quantify departure from white noise, we also apply the Ljung-Box Q test at several maximum lags  $K$ . For each combination of variable, operator, and lag, we obtain a p-value  $p_{LB}$ . Figure 12 displays these p-values on a log scale.

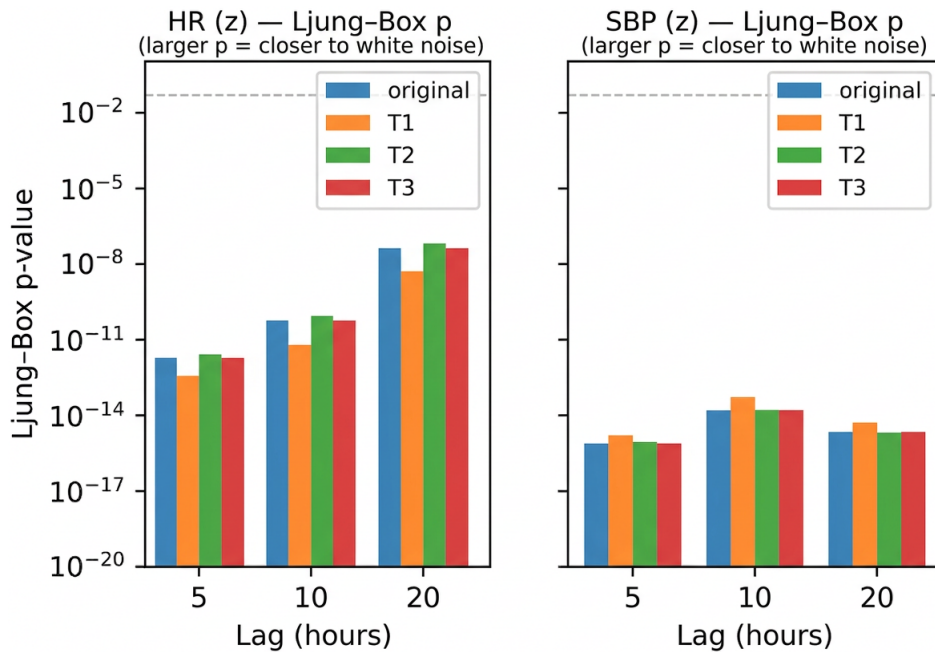


Figure 12: Ljung-Box p-values for HR (left) and SBP (right) at lags  $K \in \{5, 10, 20\}$  in standardized space (log scale). All operators preserve highly significant autocorrelation patterns, confirming that time-series structure is retained.

Finally, we estimate power spectral densities using Welch’s method for HR and SBP before and after perturbation.

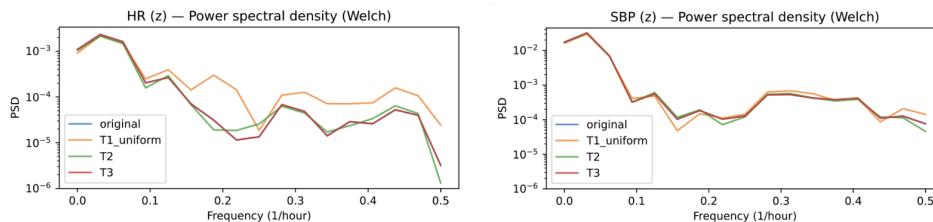


Figure 13: Welch power spectral density estimates for HR (left) and SBP (right) in standardized space. T1/T2 slightly reshape spectral energy at some frequencies, while T3 is nearly identical to the original.

From a temporal perspective, T1 and T2 inject nontrivial perturbation while preserving the main dependence structures. Their ACF and PACF profiles remain close to the original, especially at short lags. T2 tends to smooth higher lags slightly more than T1. Ljung-Box tests show that all operators retain highly significant autocorrelation patterns, meaning that the resulting sequences remain far from white noise. PSD estimates further indicate that T1 produces visible but moderate spectral changes, T2 slightly less so, while T3 leaves spectral structure almost unchanged. Overall, T1 and T2 strike a balance between perturbing fine-grained temporal patterns and preserving clinically meaningful dependence, whereas T3 is essentially statistically transparent.

## 6.5 Summary of Geometric and Statistical Properties

Combining Sections 6.2–6.4, several conclusions emerge at the column level. First, T1, T2, and T3 satisfy mean–variance preservation and the unified z-score  $\ell_\infty$  bound on real ICU data, with column-wise mean and variance deviations at numerical precision and  $\|z' - z\|_\infty$  tightly controlled by the configured  $\alpha$ . Second, for small to moderate  $\alpha$ , marginal histograms, empirical CDFs, and out-of-range rates remain close to the original data. Third, T2 is the most stable with respect to multivariate correlation matrices, T1 tends to preserve short-range autocorrelation best, and T3 is nearly perfect on all such statistics.

From a purely geometric and utility-centered perspective, all three operators appear strong, and T3 arguably appears too strong. This naturally raises the privacy question: given such smooth geometric and statistical behavior, how much do these operators actually increase reconstruction and re-identification difficulty under the C5 threat model across leakage levels L0, L1, and L2. We now formalize a privacy evaluation protocol and study reconstruction attacks and Q-mix in detail.

## 6.6 Privacy Evaluation Protocol: Threat Model, Attack Families, and Metrics

We refine the high-level C5 threat model of Section 3.5 into an experimentally instantiated privacy evaluation protocol. The central idea is to expose perturbed outputs generated by T1, T2, T3, and Q-mix to attackers with different leakage resources and attack objectives, and to quantify how much reconstruction and identification performance degrades on average.

### 6.6.1 Evaluation goals

The evaluation has three layers. The first concerns geometric and statistical sanity, namely numerical verification of C1 through C3 on real data, which has already been addressed in Sections 6.2–6.4. The second concerns average-case attack difficulty: for each attack family, we ask whether reconstruction error, record-linkage accuracy, membership success, and attribute leakage are substantially worsened by the operator. The third concerns conceptual interpretation through analogies with cryptographic security games, such as chosen-plaintext and indistinguishability-style settings.

### 6.6.2 Leakage levels L0/L1/L2 for Attack A

Under C5, the adversary is no-key and structure-aware. This means that the attacker knows the exact definitions and implementation details of T1, T2, T3, and Q-mix, together with public parameters such as  $\alpha$ , window lengths, and Q-mix dimensions, but does not possess the internal hospital randomness used to instantiate per-stay transforms.

We stratify leakage resources for reconstruction Attack A into three levels. Under L0, the attacker observes many perturbed samples  $y = T(x)$  but no paired  $(x, y)$  examples, so attacks are unsupervised. Under L1, the attacker has only a very small fraction of paired examples, modeling occasional leakage or limited supervision. Under L2, the attacker has access to a substantial fraction of paired examples, such as 20% of stays, and can therefore train a supervised inverse model. In this section, we primarily instantiate Attack A under L2 and compare it with an approximate L1 regime based on very sparse paired data.

### 6.6.3 Attack families A/B/C/D

We group attacks by objective. Attack family A concerns pointwise or sequence reconstruction: given a perturbed sequence  $y$ , the attacker attempts to recover the original  $x$  or its standardized version  $z$ . Attack family B concerns record linkage and re-identification: given perturbed records and a candidate set of original records, the attacker tries to match each perturbed record to its most likely source. Attack family C concerns membership inference, namely deciding whether a particular individual contributed to the original cohort, a problem extensively studied in the machine-learning privacy literature (Shokri et al., 2017; Yeom et al., 2018; Carlini et al., 2022). Attack family D includes attribute inference and distinguishability-style games, such as predicting a sensitive summary attribute from a perturbed record or distinguishing between two candidate originals given a perturbed output.

The single-column experiments in this section focus mainly on A-family linear reconstruction, while membership- and attribute-related proxies are used in the Q-mix experiments. Richer multivariate B, C, and D attacks are deferred to later sections.

### 6.6.4 Evaluation metrics

For Attack A, the primary reconstruction metric in standardized space is  $R^2$ ,

$$R_v^2 = 1 - \frac{\sum_s \|\hat{z}_{s,v} - z_{s,v}\|_2^2}{\sum_s \|z_{s,v} - \bar{z}_v \mathbf{1}\|_2^2},$$

where  $\bar{z}_v$  is the cohort mean, which is approximately zero after standardization. Values near 1 indicate nearly perfect reconstruction, whereas values near 0 indicate performance close to a constant baseline. We also report the mean absolute error in z-score space,

$$\text{MAE}_{z,v} = \mathbb{E}_{s,t} [|\hat{z}_{s,v}(t) - z_{s,v}(t)|],$$

and, in auxiliary diagnostics, hit-rates within specified z-score bands.

For Attack B, we evaluate record linkage using top- $k$  re-identification rate,

$$\text{Reid}@k = \mathbb{P}[\pi_y^{-1}(i^*) \leq k],$$

together with a pairwise re-identification AUC based on similarity scores. For Attack C, we use the standard ROC AUC for membership classification and define membership advantage as

$$\text{Adv}_{\text{MI}} = |\text{AUC} - 0.5|.$$

For Attack D, we use attribute-inference  $R^2$ ,

$$R_{\text{attr}}^2 = 1 - \frac{\sum_s (\hat{a}_s - a_s)^2}{\sum_s (a_s - \bar{a})^2},$$

where  $a_s$  denotes a sensitive scalar attribute extracted from the original sequence. In distinguishability games, if the attacker must infer a hidden bit  $b \in \{0, 1\}$ , we report both classification accuracy and indistinguishability advantage,

$$\text{Adv}_{\text{IND}} = |\text{acc} - 0.5|.$$

In Section 6.8, these B, C, and D metrics are instantiated on HR and glucose under Q-mix.

## 6.7 Reconstruction Attacks (Attack A): $\alpha$ -hierarchy and High Invertibility of T3

We now instantiate Attack A under L2 using a linear reconstruction model and analyze how invertibility varies across operators and across  $\alpha$ .

### 6.7.1 Attack setup and training protocol

We consider single-column sequence reconstruction. Given an observed perturbed sequence  $y_{s,v}$ , the attacker aims to recover the standardized original sequence  $z_{s,v}$ . Under L2, the attacker has access to approximately 20% of stays as paired samples  $\{(y_{s,v}, z_{s,v})\}$  and uses the remaining 80% for held-out evaluation. We also simulate a near-L1 regime in which only 0.01% of stays are paired.

The reconstruction model is linear:

$$\hat{z}_{s,v} = W_v y_{s,v} + b_v,$$

where  $W_v$  is given Toeplitz structure, equivalently a one-dimensional convolutional kernel, in order to encourage locality. The model is trained by minimizing mean squared error,

$$\min_{W_v, b_v} \mathbb{E}_s [\|\hat{z}_{s,v} - z_{s,v}\|_2^2].$$

Optimization is performed with Adam or SGD and early stopping on a validation subset of paired data. For each operator and each  $\alpha$ , we train a separate attacker. Experiments are reported mainly for HR and glucose under T1\_uniform, T1\_weighted, T2, and T3, with  $\alpha \in \{1.0, 2.0, 3.0, 5.0\}$ .

### 6.7.2 Results: gradual $\alpha$ -dependence for T1/T2 vs high invertibility of T3

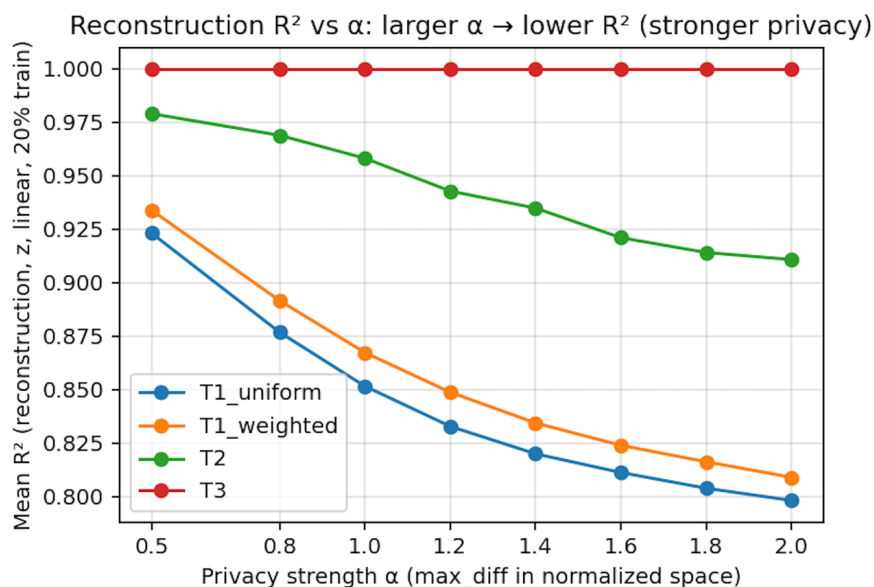
Figure 14 plots reconstruction  $R^2$  as a function of  $\alpha$  for HR under L2, and Table 2 reports exact values for selected operators. Additional results for glucose are summarized in Table 3.

Table 2: Attack A reconstruction  $R^2$  for HR in standardized space under L2 (20% pairs, linear attacker) as a function of  $\alpha$ .

operator	$\alpha = 1.0$	$\alpha = 2.0$	$\alpha = 3.0$	$\alpha = 5.0$
T1_uniform	0.8192	0.7560	0.7555	0.7570
T2	0.9738	0.9026	0.8655	0.7841
T3	0.999997	0.999997	0.999997	0.999997

 Table 3: Attack A reconstruction  $R^2$  for glucose in standardized space under L2 (20% pairs, linear attacker).

operator	$\alpha = 1.0$	$\alpha = 2.0$	$\alpha = 3.0$
T1_uniform	0.8598	0.7943	0.7757
T2	0.9601	0.9053	0.8699
T3	0.999984	0.999984	0.999984


 Figure 14: Attack A reconstruction  $R^2$  vs privacy strength  $\alpha$  for HR in standardized space under L2 (20% pairs, linear attacker). Larger  $\alpha$  leads to lower  $R^2$  for T1/T2, while T3 remains almost perfectly invertible.

T3 is clearly a highly invertible negative case. For HR under L2, it yields  $R^2 \approx 0.999997$  across all tested  $\alpha$ , and for glucose it maintains  $R^2 \approx 0.999984$ . Even under the near-L1 regime with only 0.01% paired samples, T3 still achieves  $R^2 \gtrsim 0.9$ , indicating that extremely sparse leakage is enough to learn an accurate inverse. Thus, despite its excellent geometric behavior, T3 is essentially linearly invertible under C5 + L2.

T1 and T2 exhibit a more desirable pattern. Increasing  $\alpha$  decreases reconstruction  $R^2$ , confirming that the unified z-score bound acts as a valid privacy knob. For HR under L2, T1\_uniform drops from approximately 0.82 at  $\alpha = 1.0$  to approximately 0.76 at  $\alpha = 2.0$  and then stabilizes. T2 decreases from approximately 0.97 at  $\alpha = 1.0$  to approximately 0.78 at  $\alpha = 5.0$ . Glucose exhibits a similar monotone decrease. Under the near-L1 regime, the same qualitative pattern is observed, though less strongly.

The key point is that this  $\alpha$ -hierarchy is effective but gradual: even at large  $\alpha$ , many variables retain reconstruction  $R^2$  in the 0.7–0.8 range, meaning that linear attackers still recover a substantial fraction of per-stay variability.

### 6.7.3 Limitations of the $\alpha$ -hierarchy

From a privacy perspective, relying solely on  $\alpha$  as a perturbation-strength knob has clear limitations. As  $\alpha$  increases, marginal KS distances, autocorrelation profiles, and downstream predictive performance all begin to degrade, yet reconstruction  $R^2$  decreases only gradually and often remains relatively high. Thus, purely noise-like designs, whether T1, T2, or Gaussian baselines, can improve privacy smoothly but struggle to induce a sharp privacy step at a fixed  $\alpha$ . This motivates the introduction of per-stay orthogonal randomization via Q-mix.

### 6.8 Q-mix Pilot: One-step Privacy Cliff at Fixed $\alpha$

We now evaluate per-stay orthogonal Q-mixing, introduced in Section 5.6, combined with T1 or T2 at a fixed  $\alpha$ , focusing on reconstruction difficulty and utility for HR and glucose.

#### 6.8.1 Experimental setup

We restrict attention to HR and glucose, which are both clinically sensitive and relatively smooth. We compare the original operators T1\_uniform, T1\_weighted, and T2 with their Q-mix variants.

For each stay  $s$  and variable  $v \in \{\text{HR, glucose}\}$ , we construct a  $48 \times 48$  orthogonal permutation matrix  $Q_{s,v}$  using a pseudo-random generator seeded by an internal hospital secret together with  $(s, v)$ . The permutation is constrained to be approximately banded so as to preserve local temporal coherence. The time series is partitioned into windows of length 48, transformed by  $Q_{s,v}$ , perturbed in the mixed coordinate system by T1 or T2, and then unmixed by  $Q_{s,v}^T$ .

All configurations use  $\alpha = 1.0$ , so that  $\|z' - z\|_\infty \leq 1.0$  throughout. For Attack A, we use the same L2 linear reconstruction setup as in Section 6.7.1. For Attacks B, C, and D, we evaluate record linkage, membership inference, and attribute or distinguishability experiments in standardized space, again comparing with and without Q-mix.

#### 6.8.2 Reconstruction: step-like drop of $R^2$

Figure 15 and Table 4 summarize Attack A reconstruction performance for HR and glucose at  $\alpha = 1.0$ .

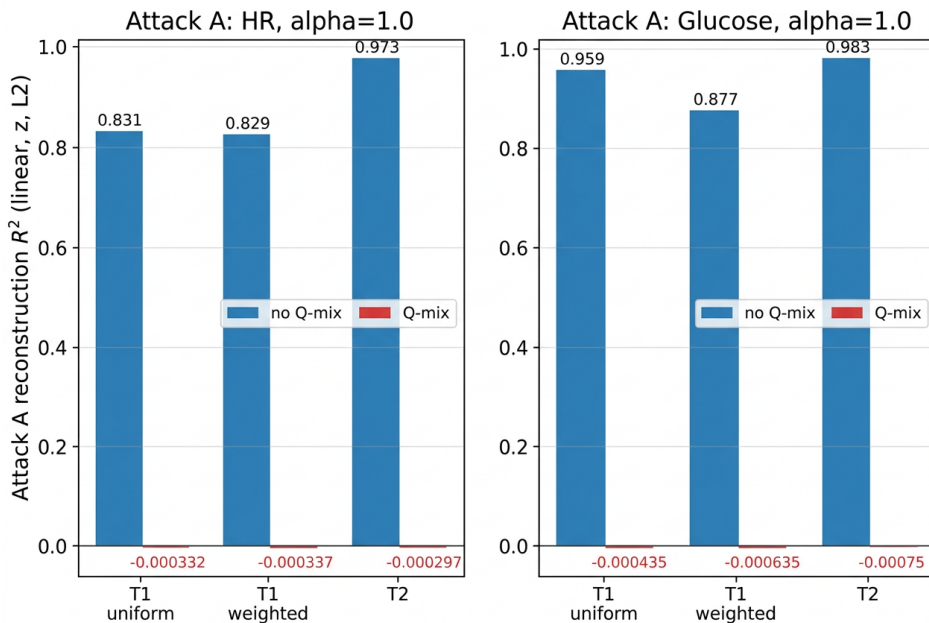


Figure 15: Attack A (L2, linear) reconstruction  $R^2$  for HR (left) and glucose (right) at  $\alpha = 1.0$ , with and without Q-mix. Q-mix drives  $R^2$  from approximately 0.8–0.98 down to approximately 0.

At the same  $\alpha = 1.0$ , Q-mix does much more than gradually degrade reconstruction quality. Without Q-mix, HR reconstruction achieves  $R^2 \approx 0.83$  for T1 variants and  $R^2 \approx 0.97$  for T2, while glucose reconstruction

Table 4: Attack A reconstruction  $R^2$  and z-score MAE  $MAE_z$  at  $\alpha = 1.0$  for HR and glucose under L2 (20% pairs, linear attacker), with and without Q-mix.

variable	operator	$R^2$	$MAE_z$
<b>No Q-mix</b>			
HR	T1_uniform	0.8308	0.3267
HR	T1_weighted	0.8288	0.3219
HR	T2	0.9734	0.1278
Glucose	T1_uniform	0.9592	0.1437
Glucose	T1_weighted	0.8769	0.2688
Glucose	T2	0.9835	0.1027
<b>With Q-mix</b>			
HR	Q + T1_uniform	$-3.3 \times 10^{-4}$	0.7786
HR	Q + T1_weighted	$-3.4 \times 10^{-4}$	0.7786
HR	Q + T2	$-3.0 \times 10^{-4}$	0.7786
Glucose	Q + T1_uniform	$-4.4 \times 10^{-4}$	0.6434
Glucose	Q + T1_weighted	$-6.4 \times 10^{-4}$	0.6433
Glucose	Q + T2	$-7.5 \times 10^{-4}$	0.6434

is even easier. Once Q-mix is wrapped around the same operators,  $R^2$  collapses to approximately zero, slightly negative because of finite-sample estimation, and  $MAE_z$  rises sharply. In effect, Q-mix pushes linear reconstruction back to the constant-baseline regime and creates a one-step privacy cliff rather than a smooth degradation.

### 6.8.3 Q-mix and attacks B/C/D: record, membership, and attribute leakage

We next apply the broader privacy evaluation protocol to Q-mix outputs for HR and glucose at  $\alpha = 1.0$ .

For Attack B, record linkage is evaluated with candidate set size  $m = 10$ , for which random guessing yields  $Reid@1 = 0.1$ . Figure 16 shows that re-identification rates for HR and glucose remain close to this baseline.

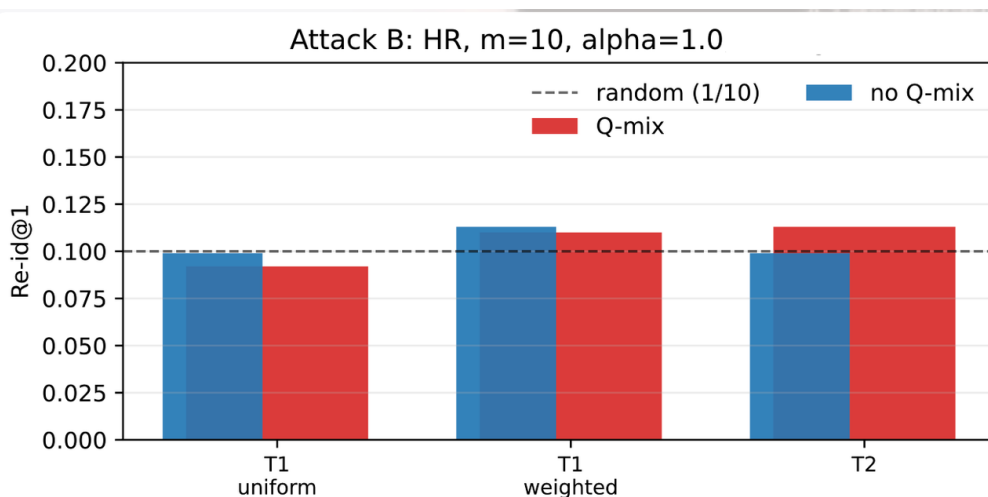


Figure 16: Attack B (record linkage)  $Re-id@1$  at  $\alpha = 1.0$ , candidate set size  $m = 10$ , for HR and glucose with Q-mix. All values are close to the random baseline  $1/m = 0.1$ .

For Attack C, Figure 17 reports membership-inference AUC for HR. Values remain close to 0.5, implying negligible advantage over random guessing; glucose shows the same pattern.

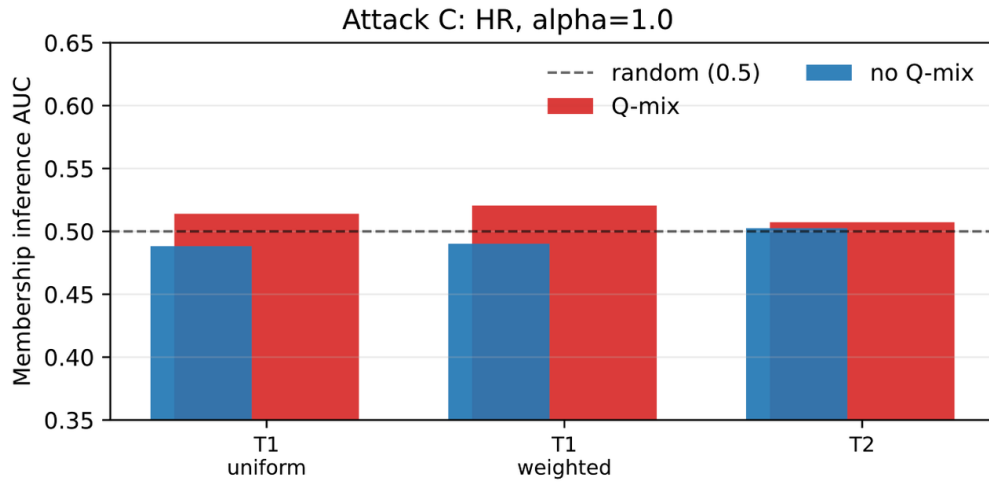


Figure 17: Attack C (membership inference) ROC AUC at  $\alpha = 1.0$  for HR, with and without Q-mix. Values remain close to 0.5, implying negligible advantage.

For Attack D, we consider attributes such as the maximum value, whether the sequence exceeds the 90th percentile, and the value at 24 hours. Figure 18 shows attribute-inference  $R^2$  for HR.

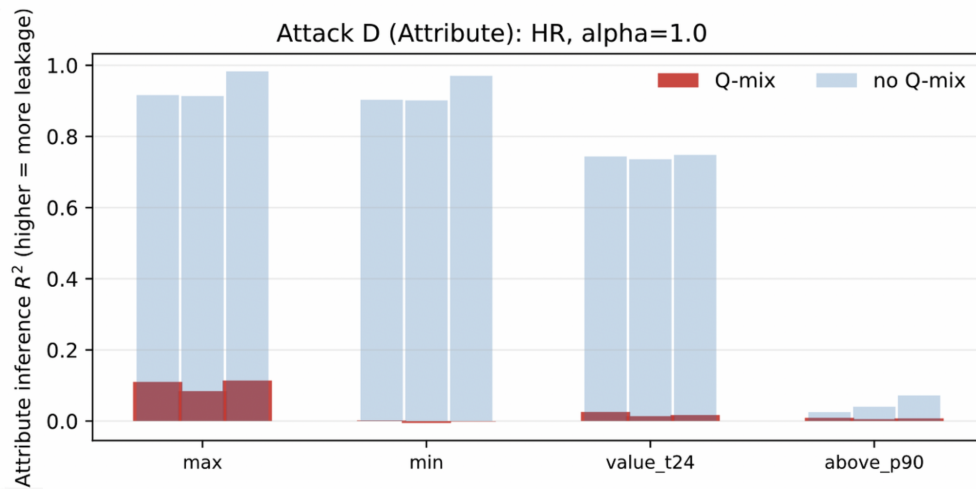


Figure 18: Attack D (attribute inference)  $R^2$  for HR at  $\alpha = 1.0$ , with and without Q-mix. Q-mix dramatically reduces attribute leakage, especially for max and above\_p90.

For HR, attribute-inference  $R^2$  for the maximum drops from values around 0.92–0.98 without Q-mix to approximately 0.08–0.11 with Q-mix. For the above\_p90 indicator, the resulting  $R^2$  falls to roughly 0.005–0.009. Glucose exhibits a similarly strong suppression. In distinguishability-style games, shown in Figure 19, the advantage remains modest, with accuracies close to random guessing.

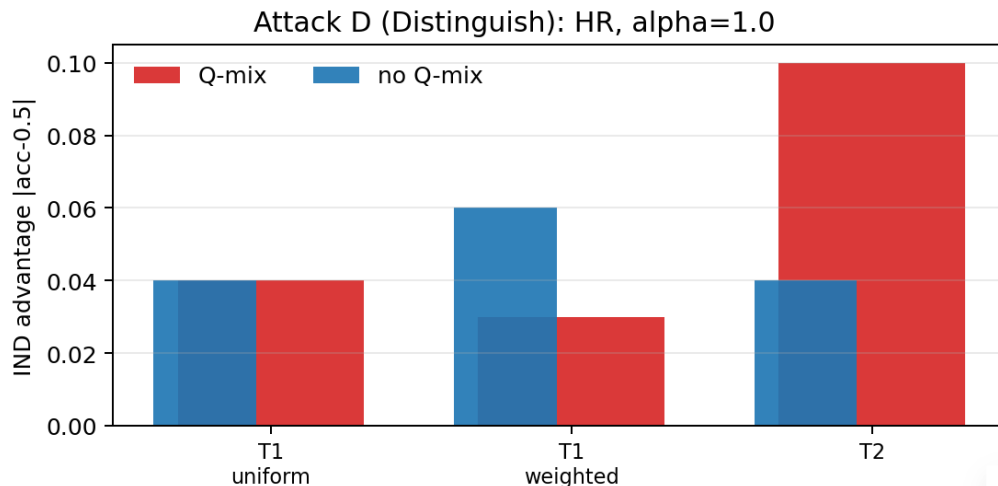


Figure 19: Attack D (distinguishability) IND advantage  $|\text{acc} - 0.5|$  for HR at  $\alpha = 1.0$ , with and without Q-mix. Values remain modest, and accuracies stay close to 0.5.

Overall, relative to the no-Q-mix setting at the same  $\alpha$ , Q-mix collapses linear reconstruction  $R^2$  for HR and glucose to approximately zero, keeps record linkage and membership metrics near random baselines, and strongly suppresses attribute leakage. This matches the intuition that per-stay orthogonal mixing destroys coherent per-stay structure in the original time order, even if an attacker learns an approximate inverse in the mixed coordinate system.

#### 6.8.4 Utility and shape metrics: cost of Q-mix

We now quantify the utility cost of Q-mix for HR at  $\alpha = 1.0$ , using both shape and downstream-task metrics.

We first define a shape utility score,

$$\text{utility\_shape}_v = 1 - \text{KS}_v.$$

For HR at  $\alpha = 1.0$  with Q-mix, T1\_uniform yields  $\text{utility\_shape} = 0.938$  and T2 yields  $\text{utility\_shape} = 0.927$ . Figure 20 summarizes these scores for HR and glucose.

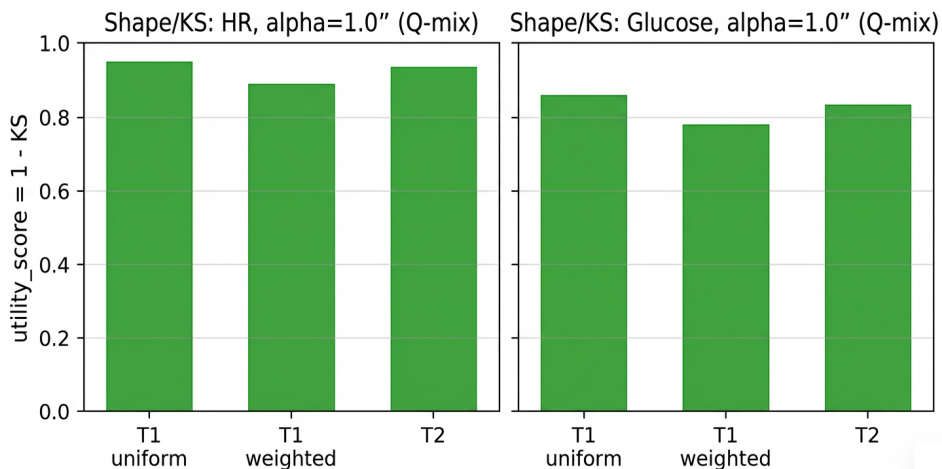


Figure 20: Shape utility scores  $\text{utility\_shape} = 1 - \text{KS}$  for HR and glucose at  $\alpha = 1.0$  with Q-mix. Scores remain high, indicating that marginal distributions are preserved reasonably well.

Mean and variance deviations remain small. For HR under Q-mix at  $\alpha = 1.0$ , the mean deviation is approximately 0.0024 for T1\_uniform and 0.0023 for T2, while variance deviations remain modest. Out-of-

range rates for HR remain below 1%, and glucose exhibits OOR rates around 2.9%–3.1%, consistent with its heavier-tailed distribution.

As a downstream task, we train a simple predictor for prolonged LOS and compare performance on raw versus perturbed HR. Figure 21 shows AUROC and AUPRC differences.

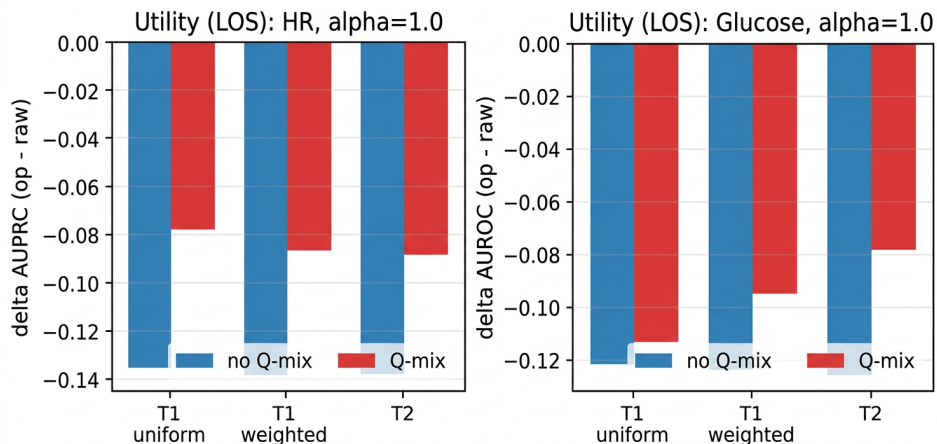


Figure 21: Utility for LOS prediction using HR or glucose at  $\alpha = 1.0$ , with and without Q-mix. Bars show differences in AUROC and AUPRC between perturbed and raw data. For HR, Q-mix + T1/T2 slightly improves AUROC and AUPRC.

For HR, T1\_uniform increases AUROC from 0.6233 to 0.6468 and AUPRC from 0.6073 to 0.6130. T2 also yields slight improvement. For glucose, LOS performance under Q-mix remains comparable to or only slightly below raw performance. Figure 22 visualizes the resulting privacy-utility trade-off for HR.

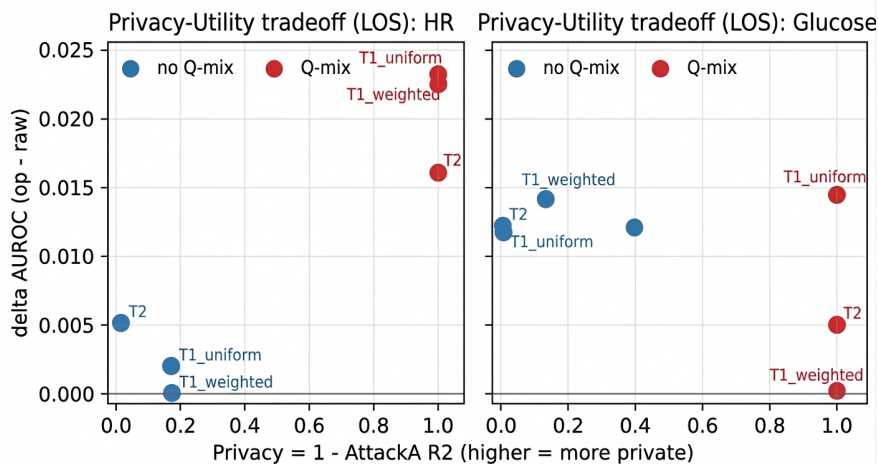


Figure 22: Privacy-utility trade-off for HR at  $\alpha = 1.0$ . The x-axis shows privacy score  $1 - R^2$ , and the y-axis shows change in AUROC for LOS prediction. Q-mix + T1/T2 achieve both high privacy and non-degraded utility.

Taken together, these results show that at fixed  $\alpha = 1.0$ , Q-mix combined with T1 or T2 drives reconstruction  $R^2$  for HR and glucose from approximately 0.8–0.98 down to nearly 0, while keeping KS-based shape scores high, out-of-range rates clinically acceptable, and downstream LOS prediction performance stable or slightly improved for HR. This supports viewing Q-mix as a deployment-layer strong-privacy switch for a small set of high-risk variables in external-sharing scenarios.

## 6.9 Section Summary: From Geometric Sanity to Privacy Steps

This section presented a systematic single-column evaluation of T1, T2, T3, and their Q-mix extensions on MIMIC-IV ICU time series. Several findings stand out.

First, from a geometric and statistical perspective, T1, T2, and T3 satisfy mean–variance preservation and the unified z-score  $\ell_\infty$  bound on real data. For small to moderate  $\alpha$ , marginal distributions, correlation matrices, autocorrelation structure, and physical numeric ranges remain close to the original data.

Second, the  $\alpha$ -hierarchy is effective but smooth. As  $\alpha$  increases, reconstruction  $R^2$  under L1 and L2 linear attacks decreases monotonically for T1 and T2, but the decline is gradual rather than step-like. Even at  $\alpha = 5.0$ , many variables still retain  $R^2$  in the 0.7–0.9 range, indicating substantial residual invertibility.

Third, T3 is a canonical negative case. Although it nearly perfectly preserves geometric and statistical structure, it is highly invertible under C5 + L2 + Attack A, with HR and glucose maintaining  $R^2 \approx 0.9999$  across all tested  $\alpha$ . It is therefore suitable only for didactic or very light in-hospital perturbation, not for strong de-identification pipelines.

Fourth, Q-mix produces a genuine privacy cliff at fixed  $\alpha$ . At  $\alpha = 1.0$ , Q-mix combined with T1 or T2 drives reconstruction  $R^2$  for HR and glucose from approximately 0.8–0.98 down to nearly 0, suppresses attribute-inference  $R^2$  dramatically, and keeps record-linkage and membership metrics close to random baselines.

Finally, the utility cost of Q-mix remains acceptable. For HR at  $\alpha = 1.0$ , KS-based shape scores remain high, out-of-range rates remain below 1%, and LOS prediction AUROC and AUPRC are not degraded and may even improve slightly. This positions Q-mix as a natural deployment-layer strong-privacy module that should be activated only for a small set of sensitive variables in external-sharing or multi-center settings, while T1 and T2 remain the workhorse operators for in-hospital research and teaching.

## 7 System: EHR-Privacy-Agent and Privacy Skill Library

Building on the geometric operators and privacy evaluation protocol of Sections 5 and 6, this section describes how these ideas are embedded into a deployable system, which we call *EHR-Privacy-Agent*. The system is designed to run on hospital ETL infrastructure without GPUs, to expose privacy-enhanced EHR views to human users and LLM-based agents, and to support continuous privacy evaluation together with iterative skill evolution.

### 7.1 Design Goals and System Constraints

#### 7.1.1 Design goals: usable and visible, but hard to reconstruct

The design of EHR-Privacy-Agent is guided by four system-level goals.

First, the privacy-enhanced tables produced by the system must remain operationally usable. In practice, this means that they should be clean, consistently typed, structurally compatible with downstream analysis scripts, conventional machine learning models, and LLM-based agents, and available on regular schedules such as nightly refreshes in the data lake.

Second, the transformed values must remain visible in the sense of basic physical interpretability and clinical intuition. Means, variances, and z-score magnitudes should remain clinically plausible. Histograms, time-series plots, and correlation matrices should continue to resemble real patient data (ICU trajectories in our running example) rather than arbitrary synthetic outputs. More specifically, the visual diagnostics examined in Section 6, including histograms, CDFs, ACF, and PSD, should not exhibit pathological distortions.

Third, the system must make records substantially harder to reconstruct under the no-key, structure-aware threat model C5 (Section 3.5) and under the leakage levels L0, L1, and L2 together with attack families A, B, C, and D. In concrete terms, strong-privacy skills should drive reconstruction  $R^2$  and attribute-inference  $R^2_{\text{attr}}$  toward 0, while keeping re-identification and membership metrics close to random baselines.

Finally, the system must remain deployable under realistic engineering constraints. It should rely only on CPUs, integrate with existing in-hospital ETL clusters, avoid any additional GPU budget or specialized hardware, and maintain computational complexity and memory use at scales compatible with tens to hundreds of thousands of ICU stays.

### 7.1.2 Threat-model constraints and the no-key requirement

EHR-Privacy-Agent adheres to the C5 threat model introduced in Section 3.5. The adversary is no-key but structure-aware. In particular, the adversary is assumed to know the mathematical definitions and source code of T1, T2, T3, and Q-mix, as well as public parameters such as  $\alpha$ , window lengths, and Q-mix block sizes. At leakage levels L1 and L2, the adversary may also observe a small or moderate fraction of paired samples  $(x, y)$ , for example 0.01% or 20% of stays.

What the adversary does not possess is any long-lived shared cryptographic key. All randomness used by the operators is generated by hospital-internal modules and is treated as per-stay short-term randomness. For Q-mix, each per-stay orthogonal matrix  $Q_{s,v}$  is generated by a pseudo-random process that combines a hospital-internal secret seed with the pair  $(\text{stay\_id}, v)$ . The adversary knows the generation algorithm, but not the internal secret itself.

At the system level, this threat model is encoded as an explicit design constraint. EHR-Privacy-Agent does not maintain any cross-batch shared keys accessible to analysts or external parties. All randomness is injected by a secure in-hospital module and is visible only within the lifetime of a single pipeline run. Privacy-enhanced data may be stored and shared long-term, but no tokens or metadata sufficient to reconstruct the internal randomness are exported alongside them.

### 7.1.3 User roles and typical scenarios

The system is designed around three primary user roles. The first is data science and engineering teams, who configure ETL jobs, define skills, run nightly pipelines, and in in-hospital environments rely on low- $\alpha$  skills without Q-mix for EDA, QA, and model development. The second is clinical researchers and quality officers, who interact with privacy-enhanced views through an LLM-based agent for cohort exploration, visualization, and basic modeling, without ever touching raw EHR tables directly. The third is external collaborators together with teaching or open-data users, who receive views generated by strong-privacy skills, typically with larger  $\alpha$  and Q-mix enabled on selected sensitive variables, or who consume downstream models trained on such views.

The aim of EHR-Privacy-Agent is to support all three categories through a single architecture, using different skill profiles rather than separate pipelines.

## 7.2 System Architecture Overview

Figure 23 shows the in-hospital nightly privacy pipeline and how EHR-Privacy-Agent is composed of operators, modules, and skills.

The first component is the raw EHR layer, namely the traditional in-hospital warehouse containing raw ICU tables such as vitals, labs, medications, and demographics. This layer is completely invisible to external agents and untrusted users.

The second component is the Operator Engine, which implements the geometric operators introduced in Section 5, including T1, T2, T3, and Q-mix, and exposes streaming, column-level APIs.

The third component is the Privacy Skill Library, which combines these operators into reusable *skills*. Each skill represents a complete pipeline from raw EHR to a privacy-enhanced table, together with scenario tags, threat-model assumptions, and parameter settings such as  $\alpha$  and Q-mix configuration.

The fourth component is the EHR-Privacy-Agent itself, namely an LLM-based orchestration and QA layer. The agent can access only skill outputs through tool APIs, interprets user natural-language queries, selects appropriate skills, and performs downstream analyses on the resulting privacy-enhanced views.

The fifth component is the Evaluation and Monitoring module. This module runs the geometric sanity checks and privacy attacks introduced in Section 6, both for pre-deployment evaluation of new skills and for periodic health checks of deployed skills in order to monitor drift in geometric and privacy metrics.

These components are connected through a unified configuration and logging layer. Skills are stored as YAML files under version control. Nightly jobs generate privacy-enhanced views according to the configured skill set. The agent either loads existing views or triggers incremental computation. The evaluation module periodically reruns attack suites and QA checks on these views.

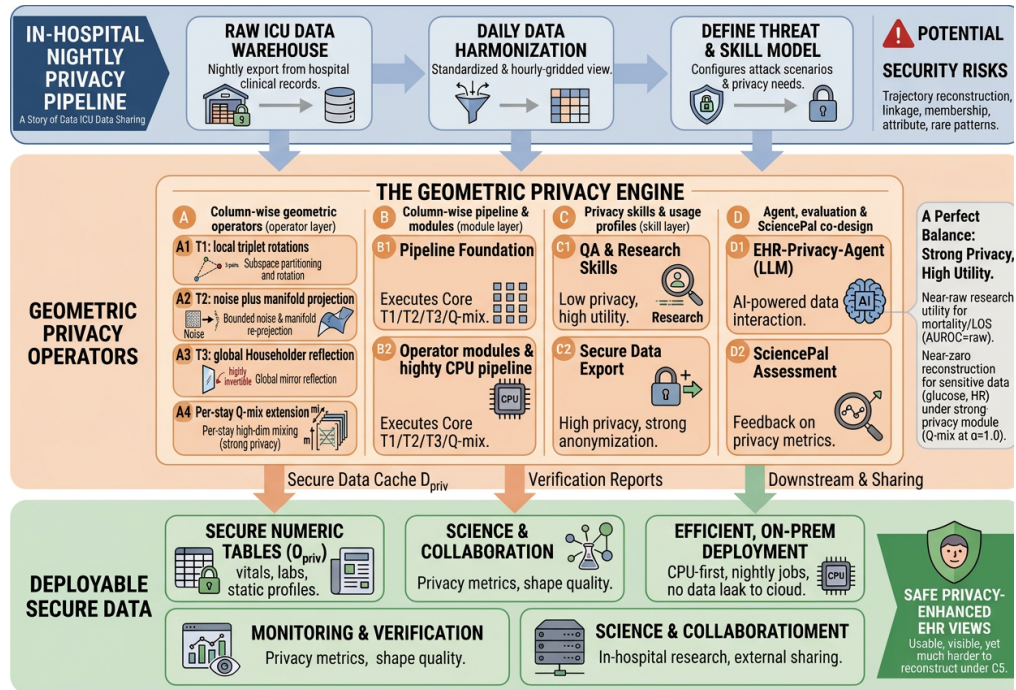


Figure 23: System-level overview of the in-hospital nightly privacy pipeline and geometric privacy engine. Each night, raw EHR tables (ICU vitals, labs, medications in our running example) are exported from the production warehouse into a harmonized, hourly-gridded view. Given a threat model and a chosen privacy skill configuration, the *geometric privacy engine* applies column-wise operators (T1/T2/T3 and per-stay Q-mix) within a CPU-only pipeline to produce a secure numeric cache  $D_{\text{priv}}$ . Privacy skills and usage profiles distinguish low-privacy, high-utility views for in-hospital QA and research from strong-privacy export views with Q-mix enabled on selected variables. An LLM-based EHR-Privacy-Agent and the SciencePal assessment loop sit on top of these views to support interactive analysis, monitoring of privacy and shape metrics, and collaborative tuning of skills, while all data remain on-premise and never leave the hospital intranet.

### 7.3 Operator Library and Privacy Skill Library

The system’s flexibility under computational and threat-model constraints relies on a three-layer design: *Operator*  $\rightarrow$  *Module*  $\rightarrow$  *Skill*.

#### 7.3.1 Operator layer: geometric atomic operators

The bottom layer is the operator library, which contains the geometric atoms introduced in Section 5. These include T1\_uniform, a local three-point rotation operator satisfying C1–C4 and particularly effective at preserving short-range ACF; T2, a noise-plus-projection operator on the mean–variance manifold that tends to preserve cross-column correlation structures well; T3, a global Householder reflection that is geometrically almost perfect but highly invertible under C5 + L2 attacks and is therefore explicitly flagged as a negative case; and Q-mix, a per-stay orthogonal mixing wrapper that may be applied to a small set of sensitive variables such as HR and glucose, as studied in Section 6.8.

At this layer, the basic unit of computation is a single column. The input is a standardized time series  $z_{s,v}$  for variable  $v$ , together with  $(\mu_v, \sigma_v)$  and configuration parameters such as  $\alpha$ . The output is a perturbed  $z'_{s,v}$ , followed by de-standardization to  $x'_{s,v}$  through

$$x'_{s,v} = \mu_v \mathbf{1} + \sigma_v z'_{s,v}.$$

The operator layer is scenario-agnostic. It is unaware of who is calling it or for what purpose, and guarantees only the geometric constraints C1–C4 together with the exposure of a unified privacy knob  $\alpha$ .

### 7.3.2 Module layer: operator composition and cross-column logic

Above the operator layer we define reusable *modules*. The `ColumnTransformModule` takes a list of variables  $\{v_1, \dots, v_k\}$  together with per-column configurations such as  $\alpha$  and the allowed operator set, applies T1, T2, T3, or Q-mix independently to each column, and supports batched as well as streaming processing of long time series.

The `CrossColumnModule` handles structural cross-column logic. Examples include enforcing shared random seeds across certain variable groups in controlled experiments, or performing pre-Q-mix normalization or aggregation on variable groups when necessary.

The `TemporalSlicingModule` splits each stay’s time axis into fixed-length windows, for example 48 hours, in order to better align with Q-mix block dimensions, and manages overlap and edge cases for stays that span multiple windows.

Taken together, the module layer serves as an intermediate template between low-level operators and high-level skills. It hides operator details from higher layers while providing structured building blocks for skill construction.

### 7.3.3 Skill layer: configuration-bound pipelines

At the top layer, a *privacy skill* represents a complete pipeline from raw EHR to a particular privacy-enhanced view under a specific use case and threat model. It also serves as a stable contract between the data warehouse and downstream analysis tools.

Each skill includes an input scope, specifying the cohort definition, time window, and variable list; a transform configuration, specifying per-column  $\alpha$ , the allowed operators, and whether Q-mix or T3 is enabled; an output format, specifying target schema, indexing strategy, and partitioning; threat-model assumptions, indicating the relevant leakage levels and dominant attack families; and usage tags, such as `in_hospital_research`, `export_strong_privacy`, or `teaching_demo`.

In implementation, skills are defined as YAML documents. A typical in-hospital exploratory skill is shown in Figure 24(a).

In this example, HR and glucose are processed at  $\alpha = 1.0$  through Q-mix followed by T1 or T2, whereas lactate and other variables rely only on T2 at the same privacy level. The tag `usage: export` marks this skill as a strong-privacy profile for external sharing, which we revisit in Section 7.7.

### 7.3.4 Running case

To make the operator library more concrete, Figure 25 presents a small running case. For each operator, we show a minimal before/after example on toy data (time stamps, IDs, counts, text, or categories), highlighting how the transformation preserves global structure while visibly altering per-record values.

## 7.4 Nightly Pipeline and Data Flow

A central engineering goal of EHR-Privacy-Agent is to turn privacy enhancement into a routine nightly task on CPU-only infrastructure.

### 7.4.1 Configuration-driven nightly job

Each night, the system executes a configuration-driven pipeline. The first step is cohort selection and snapshotting. Configured SQL queries or cohort definitions are run on the raw EHR warehouse to identify the stays or episodes for the current batch (ICU admissions in our running example), such as recent admissions or periodic snapshots, and a read-only snapshot with fixed schema and version is materialized in order to avoid conflicts with live transactional systems.

The second step is standardization and mean–variance updating. On a designated training cohort, the system updates column-wise  $(\mu_v, \sigma_v)$ , or reuses a frozen parameter version when appropriate, and standardizes the target cohort to obtain  $z_{s,v} = (x_{s,v} - \mu_v \mathbf{1}) / \sigma_v$ .

The third step is execution of operator modules for each configured skill. The relevant `ColumnTransformModule`, `CrossColumnModule`, and `TemporalSlicingModule` are invoked, T1, T2, T3, or Q-mix are applied in z-score space according to per-variable settings, and the outputs are de-standardized back to  $x'_{s,v}$  and written into the target table.

The fourth step is persistence and indexing. Secondary indices are built on each skill output table, for example by `stay_id`, variable, and time, and metadata such as skill id, parameter version, and pipeline timestamp are

```

id: skill_in_hosp_vitals_explore
usage: in_hospital_research
threat_model:
  leakage: L1
  attacks: ["A_reconstruction"]
operators:
  default_alpha: 0.5
  per_variable:
    HR:
      ops: ["T1_uniform", "T2"]
      alpha: 0.5
    Lactate:
      ops: ["T2"]
      alpha: 0.5
    Glucose:
      ops: ["T2"]
      alpha: 0.5
qmix:
  enabled: false
output:
  table: "priv_vitals_hourly_v1"
  time_window_hours: [0, 72]
  format: "long"

id: skill_export_strong_privacy
usage: export
threat_model:
  leakage: L2
  attacks: ["A_reconstruction",
           "B_linkage",
           "C_membership"]
operators:
  default_alpha: 1.0
  per_variable:
    HR:
      ops: ["T1_uniform", "T2"]
      alpha: 1.0
    Glucose:
      ops: ["T1_uniform", "T2"]
      alpha: 1.0
    Lactate:
      ops: ["T2"]
      alpha: 1.0
qmix:
  enabled: true
  variables: ["HR", "Glucose"]
  block_length: 48
  secret_seed: "${HOSPITAL_SEED}"
output:
  table: "priv_vitals_export_v1"
  time_window_hours: [0, 72]
  format: "long"

```

(a) In-hospital vitals exploration skill. HR may use T1 or T2 at  $\alpha = 0.5$ ; Q-mix is disabled.

(b) Export-oriented strong-privacy skill. Q-mix is enabled at  $\alpha = 1.0$  for HR and glucose.

Figure 24: Example YAML skill definitions for two deployment scenarios. (a) A typical in-hospital research profile with moderate privacy and no Q-mix. (b) A conservative export profile with higher  $\alpha$  and Q-mix enabled for high-risk variables.

attached for traceability.

The final step is automatic evaluation and alerting. Geometric sanity checks, together with basic distribution QA such as KS and out-of-range monitoring, are run on each newly created privacy view. For selected pilot skills, a subset of Attacks A, B, and C is also run, monitoring reconstruction  $R^2$ , linkage accuracy, and membership AUC. If any metric exceeds configured thresholds, alerts are raised and the corresponding outputs can be marked as experimental or unsafe for export.

#### 7.4.2 CPU-only implementation and resource configuration

The Operator Engine follows two engineering principles. The first is controlled complexity: per-stay, per-column complexity remains linear or near-linear in the sequence length, namely  $O(n_{s,v})$  or  $O(n_{s,v} \log n_{s,v})$ . The second is batching and streaming: long time series, such as 7-day ICU trajectories, are sliced into fixed windows, for example 48 hours, and per-window caches store local means, variances, and Q-mix matrices so that repeated computations are avoided whenever possible.

In a MIMIC-IV-scale pilot running on a 32-core commodity CPU server, we can perturb tens of thousands of ICU stays’ vitals and labs tables with T1 and T2 within a few hours, while still enabling Q-mix for HR and glucose in strong-privacy export skills without violating nightly SLAs. Compared with GPU-heavy generative approaches such as CLEAR-Note or CTGAN (Goodfellow et al., 2014a; Xu et al., 2019a), discussed later in Section 8.6, this pipeline achieves much higher per-stay throughput under equivalent hardware budgets.

#### 7.4.3 Versioning and rollback

Because skill designs evolve in response to new attacks and clinical feedback, the system explicitly supports coexistence of multiple versions, auditable change history, and safe rollback. Different versions of the same

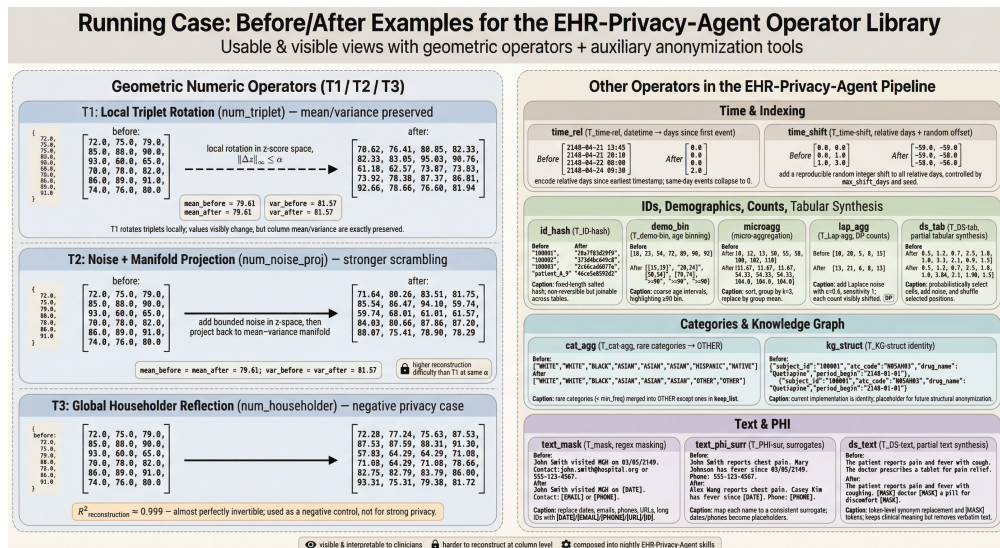


Figure 25: Left: geometric numeric operators T1–T3 applied to one standardized vital-sign column, with toy before/after values showing mean–variance–preserving local rotation (T1), stronger scrambling via bounded noise plus manifold projection (T2), and an almost invertible Householder reflection as a negative privacy case (T3). Right: auxiliary operators for time/indexing, IDs and demographics, counts and tabular synthesis, categories/knowledge graph, and clinical text/PHI, each illustrated with minimal before/after snippets to show how identifiers are removed or blurred while keeping data usable for analysis.

skill id may coexist, enabling controlled A/B comparisons of attack difficulty and downstream utility. Skill YAML files and evaluation reports are stored in a Git repository, and each change is tracked with a commit record, reviewer, and rationale. If evaluation later reveals a privacy or geometric regression, such as an unexpected increase in reconstruction  $R^2$  or OOR rates, the system can revert to the last approved skill version by a single configuration change.

### 7.5 Agent Layer: From LLM Tools to Privacy Views

Although the operator library and nightly pipeline can be used in batch mode, the main user-facing interface is an LLM-based *EHR-Privacy-Agent*.

#### 7.5.1 Interaction pattern: from natural language to skill calls

A typical interaction begins with a natural-language request, such as a user asking whether the distributions of HR and lactate in ICU patients have drifted over the last three years, or asking for a sharable dataset view suitable for replicating a LOS model from a published paper.

The agent first performs intent understanding and skill selection. Using lightweight rules together with LLM reasoning, it maps the request to one or more skills. In-hospital exploratory analyses are routed to skills such as `skill_in_hosp_vitals_explore`, whereas external sharing requests are routed to stronger skills such as `skill_export_strong_privacy`. If the user explicitly requests strong privacy or external sharing only, the agent prefers skills with larger  $\alpha$  and Q-mix enabled.

The selected skill is then invoked through a tool call of the form `run_skill(skill_id, cohort_spec, time_window, . . .)`. If the nightly pipeline has already produced the corresponding view, it is loaded directly; otherwise, an incremental run is triggered subject to resource policies.

Finally, the agent performs downstream EDA, visualization, simple modeling, and natural-language explanation on top of the privacy-enhanced tables. At no point does the agent access raw EHR tables directly. All subsequent analysis operates only on the privacy views defined by skills.

#### 7.5.2 Tool APIs: listing, inspecting, and running skills

To support traceable and safe usage, the agent layer exposes three primary tool APIs. The first, `list_skills(usage_filter)`, returns the available skills together with metadata such as usage scenario, supported

$\alpha$  range, whether Q-mix or T3 is enabled, and a summary of recent evaluation results. The second, `inspect_skill(skill_id)`, displays detailed configuration for a specified skill, including YAML expansion, operator combinations, Q-mix options, randomness-source handling, and summaries of recent attack evaluations. In external settings, this inspection function may be restricted in order to avoid revealing sensitive implementation details. The third, `run_skill(skill_id, cohort_spec, . . .)`, executes the skill and returns either a view handle or a data sample, depending on permissions.

### 7.5.3 Illustrative usage scenarios

Three scenarios illustrate the intended usage pattern. In the first, which concerns in-hospital EDA and QA, a quality officer wants to check whether HR and lactate distributions have shifted across quarters. The agent selects `skill_in_hosp_vitals_explore` for each quarter, loads the corresponding privacy views, plots histograms, trends, and correlation matrices, and summarizes the differences in natural language.

In the second scenario, which concerns research replication and collaboration, a data scientist develops an ICU mortality model for a multi-center study. Within the hospital, they iterate using low- $\alpha$ , no-Q-mix skills for feature engineering and hyperparameter tuning. Once the model is fixed, they export a strong-privacy view using `skill_export_strong_privacy`, which enables Q-mix for HR and glucose, and then package trained model weights together with performance summaries for collaborators.

In the third scenario, which concerns teaching and simulation, clinicians or students only need to see the general shape of ICU data. A teaching-oriented skill may therefore use T3 at low  $\alpha$ , giving a simple configuration that preserves visual realism while not aiming for strong privacy guarantees.

## 7.6 AI-making at the System Level: From Natural Language to Skill YAML

Section 4 introduced the AI-making protocol for designing the operator families T1, T2, T3, and Q-mix. At the system level, we extend the same idea to the authoring and evolution of privacy skills and full pipelines, with SciencePal acting as an assistant.

### 7.6.1 Lifecycle of a new skill

A new skill moves from concept to production through several phases. First, a human stakeholder specifies the high-level need, for example a request for a stronger-privacy vitals view for multi-center analysis with special protection for HR and glucose under an L2-style threat model focused on Attacks A and B.

Second, an engineer works with SciencePal to generate a draft skill. The engineer provides the intended usage scenario, prioritized variables, desired  $\alpha$  range, and relevant attack families. SciencePal then proposes an initial YAML configuration specifying per-variable operators,  $\alpha$ , whether to enable Q-mix, with what block length, and which evaluation suites should be run.

Third, the system automatically evaluates the draft. It runs geometric sanity checks, distribution QA, and Attack A under L2, and optionally Attack B and C, and feeds the resulting metrics back to SciencePal and the engineer. If reconstruction  $R^2$  remains too high, the draft may be revised by increasing  $\alpha$  or enabling Q-mix for sensitive variables. If KS distances or out-of-range rates become too large, the draft may instead be revised by lowering  $\alpha$  or restricting the use of certain operators.

Fourth, security and clinical reviewers jointly assess the evaluation report. They confirm that privacy metrics satisfy policy thresholds and that the resulting distributions and physical interpretability remain acceptable. Once approved, the skill is marked as production-ready.

Finally, the skill is incorporated into the nightly pipeline and continuously monitored. The evaluation and monitoring module reruns attack suites periodically, watching for drift in reconstruction  $R^2$ , linkage accuracy, and downstream utility. If regressions are detected, the system can downgrade or roll back the skill.

Throughout this process, SciencePal never accesses raw EHR directly. It operates only on statistical summaries and evaluation feedback.

### 7.6.2 SciencePal-assisted skill configuration: an example

A typical AI-making interaction might begin with an engineer stating that a vitals skill is needed for external collaborators, that HR and glucose must be strongly protected, that  $\alpha$  up to 1.0 or higher is acceptable, and that under linear Attack A / L2 the desired goal is reconstruction  $R^2$  close to zero without sharply degrading LOS prediction AUROC.

SciencePal may then recommend enabling Q-mix with block length 48 on HR and glucose, while using T2 at

$\alpha = 1.0$  for the remaining vitals. The resulting skill would be tagged with usage: export and evaluated with L2 Attack A together with a LOS downstream task. The system then treats this recommendation as a draft YAML, similar to Figure 24(b), and runs the full privacy evaluation protocol to verify that it actually achieves the target combination of low reconstruction  $R^2$  and acceptable utility.

### 7.6.3 Evaluation feedback as design signal

For each new skill, the Evaluation and Monitoring module produces a unified report. This includes C1–C2 geometric metrics such as mean/variance deviations and whether  $\ell_\infty$  bounds remain within the configured  $\alpha$ , distribution QA such as KS distances, out-of-range rates, and ACF changes, Attack A/B/C metrics such as per-variable reconstruction  $R^2$ ,  $MAE_z$ , Reid@1/Reid@5, linkage AUC, membership AUC, and membership advantage, and downstream task metrics such as LOS or mortality AUROC and AUPRC.

Together, these quantities form a skill-level score vector that can be used both by SciencePal and by human reviewers. SciencePal can use the report to propose parameter updates, such as changing  $\alpha$  or enabling or disabling Q-mix on selected variables, while human reviewers can treat the same report as the basis of a semi-automated security and utility review before approving a skill for external deployment.

## 7.7 Deployment Practice and Engineering Lessons

We summarize several practical lessons from deploying EHR-Privacy-Agent in realistic environments.

### 7.7.1 Schema evolution and compatibility

EHR schemas evolve over time, with new variables, unit changes, and coding adjustments. To maintain robustness and comparability of skill behavior, each skill explicitly declares its schema dependencies, including variable names, units, and default physical ranges. Schema changes automatically trigger re-evaluation, for example when lactate units shift from mg/dL to mmol/L. Mean–variance statistics and  $\alpha$  configurations are also versioned, allowing historical skill versions to continue running on older data snapshots.

### 7.7.2 Audit, traceability, and access control

Because skills encode privacy policy, the system provides fine-grained access control, audit logging, and restrictions on re-export. Different roles may invoke only usage-labeled skills appropriate to their permissions; for example, external users may be restricted to export skills with strong privacy guarantees. Every skill invocation is logged with timestamp, user, parameters, and cohort size, enabling ex-post audit and forensic analysis. For skills with Q-mix, the system by default forbids generating less-perturbed derivative views from the same cohort, in order to reduce multi-view composition risks.

### 7.7.3 Failure modes and mitigation

In practice, several recurrent failure modes arise. Geometric implementation bugs may occasionally break mean–variance preservation or  $\ell_\infty$  bounds, but nightly C1–C2 checks detect these rapidly and block writes to production tables. Overly aggressive  $\alpha$  choices may cause large out-of-range rates or sharply degrade downstream performance, in which case automatic QA triggers downgrade or rollback. Attack metrics may also drift over time as cohorts evolve, so a previously acceptable skill may later show increased reconstruction  $R^2$  or linkage accuracy. Periodic re-evaluation is therefore critical for identifying when re-tuning or Q-mix extension becomes necessary.

Embedding attack evaluation into the same system that runs the nightly pipeline has proven more effective than one-off offline evaluation for tracking privacy and geometric risk over time.

## 7.8 Section Summary: From Geometric Operators to a Deployable System

This section showed how the geometric operators and privacy evaluation protocol of Sections 5 and 6 can be encapsulated into a nightly deployable EHR-Privacy-Agent system.

At the architectural level, the system is organized around a three-layer abstraction. The operator layer contains T1, T2, T3, and Q-mix as geometric atoms that (for T1/T2/T3) satisfy C1–C4 under the no-key constraint, with Q-mix satisfying C1–C3 and a deployment-level relaxation of C4 for a small set of high-risk variables. The module layer provides reusable column-wise, cross-column, and temporal-slicing components. The skill layer defines complete, scenario-bound and threat-model-bound pipelines in a transparent YAML format.

At the policy level, skills act as executable privacy specifications. They encode usage scenario,  $\alpha$ , operator combinations, Q-mix activation, and output schema, while versioning and rollback support continuous evolution in response to attack evaluation and clinical feedback.

At the user-interface level, the LLM-based EHR-Privacy-Agent interacts only with skill-defined privacy views and never with raw EHR. Tool APIs such as `list_skills`, `inspect_skill`, and `run_skill` map natural-language intent to concrete privacy configurations and outputs.

At the design-process level, SciencePal extends the earlier AI-making workflow from operator design to system-level skill authoring. Combined with automated evaluation and human review, this produces a closed loop linking operator design, YAML skill drafting, attack evaluation, and deployment policy.

Finally, from an engineering standpoint, a CPU-only nightly pipeline is feasible at ICU scale, integrating attack evaluation directly into the system life cycle helps detect privacy and geometric regressions early, and usage tags together with access control provide a natural separation between in-hospital and external scenarios.

In Section 8, we build on the views produced by EHR-Privacy-Agent to evaluate geometric operators and Q-mix on end-to-end tasks such as LOS and mortality prediction and generative modeling, and compare their utility and computational cost with GPU-intensive methods such as CLEAR-Note<sup>2</sup> and CTGAN.

## 8 End-to-End Experiments and Runtime

Building on the single-column analysis of Section 6 and the system architecture of Section 7, this Section evaluates EHR-Privacy-Agent in end-to-end settings. We focus on two pragmatic questions. The first is how much downstream utility the privacy-enhanced views retain on real ICU prediction and simple generation tasks, relative to raw EHR and common baselines such as naive Gaussian noise and CTGAN-style synthetic data. The second is how the runtime and compute costs of the geometric pipeline, namely T1, T2, T3, with optional Q-mix, compare with GPU-heavy generative or text deidentification pipelines.

To answer these questions, we construct a suite of prediction tasks, including mortality, LOS, and readmission, together with a small trajectory-generation experiment and runtime comparisons with CTGAN and CLEAR-Note on adult ICU data from MIMIC-IV. All downstream models are trained only on privacy-enhanced views produced by skills. Raw EHR is used only inside the hospital pipeline and is never accessed directly by the models themselves.

### 8.1 Tasks and Evaluation Setup

#### 8.1.1 Dataset and cohort construction

We use the adult ICU cohort from MIMIC-IV, closely aligned with the setup of Section 6. The population consists of adult patients with age at least 18 years, retaining only the first ICU stay per patient. To reduce pathological outliers, we exclude extremely short stays of less than 4 hours and extremely long stays of more than 30 days.

All time axes are aligned to ICU admission, with  $t = 0$  corresponding to ICU in-time. Vitals and laboratory measurements are resampled onto a 1-hour grid using forward-fill together with clipping to plausible physical ranges. We use the interval  $[0, 72]$  hours as the main prediction window, which supports early-prediction tasks.

The feature set contains both dynamic and static information. Dynamic features include common vitals such as HR, RR, SBP, DBP, MAP, SpO<sub>2</sub>, and temperature, together with laboratories such as glucose, lactate, creatinine, sodium, and potassium. Static features include sex, age group, admission service, and a coarse diagnosis category. In some configurations we also include coarse binary indicators of treatment or ventilation status, which are not subject to Q-mix. All models use a fixed patient-level train, validation, and test split, for example 60/20/20, and the same split and random seeds are reused across privacy configurations so that any performance difference can be attributed to the data view rather than to resampling.

#### 8.1.2 Downstream task definitions

We consider three canonical ICU prediction tasks. The first is in-hospital mortality prediction from the first 48 hours. The label indicates whether the patient dies during the same hospital admission, and the input consists of vitals, labs, and static features collected in the first 48 hours after ICU admission. This is a binary classification task.

The second task is ICU LOS category prediction. Here the outcome is a three-level LOS category defined as

---

<sup>2</sup>CLEAR-Note is our earlier preliminary work that performs clinical note de-identification entirely through LLM-based rewriting and verification. We plan to release it publicly in the near future.

short if  $\text{LOS} \leq 2$  days, medium if  $2 < \text{LOS} \leq 7$  days, and long if  $\text{LOS} > 7$  days. The input again consists of the same 48-hour feature window, and we report macro-AUROC, macro-AUPRC, and macro-F1.

The third task is 30-day readmission prediction. The label indicates whether the patient is readmitted within 30 days of discharge. The input uses the first 72 hours of vitals, labs, and static features. This task probes whether early ICU trajectories retain useful signal for longer-horizon outcomes.

In Section 8.5, we additionally include a small time-series generation and interpolation experiment in order to compare EHR-Privacy-Agent views with CTGAN-generated synthetic data.

### 8.1.3 Model architectures and training protocol

To keep the comparison focused on data views and privacy configurations, we intentionally use simple and transparent models with moderate capacity. For mortality, LOS, and readmission, the main sequence model is a unidirectional GRU encoder over hourly features, followed by a simple attention pooling layer and a two- or three-layer MLP head. The total parameter count lies roughly in the 1 to 2 million range.

To understand how privacy affects less expressive models, we also train classical baselines, namely logistic regression on hand-crafted summary features such as per-variable means, maxima, and slopes over the first 48 hours, and gradient-boosted trees using the same summary feature set.

Across privacy configurations, the model architecture and hyperparameter grid are kept fixed. Training uses early stopping based on validation AUROC with a fixed maximum number of epochs. Models may use a single GPU or a multicore CPU for training, but all privacy transforms, including T1, T2, T3, and Q-mix, are executed on CPU only. This design avoids artificially compensating for privacy loss by increasing model capacity, so that the comparison truly reflects the data views themselves.

### 8.1.4 Evaluation metrics and statistical treatment

For classification tasks, we report AUROC and AUPRC in the usual way. The AUROC is

$$\text{AUROC} = \int_0^1 \text{TPR}(\text{FPR}) d\text{FPR},$$

while the AUPRC is

$$\text{AUPRC} = \int_0^1 \text{Precision}(\text{Recall}) d\text{Recall}.$$

Depending on the task, the positive class corresponds to mortality, long LOS, or readmission.

We also summarize calibration through expected calibration error and the Brier score. Using a partition of predicted probabilities into  $M$  bins, the expected calibration error is

$$\text{ECE} = \sum_{m=1}^M \frac{|B_m|}{N} |\text{acc}(B_m) - \text{conf}(B_m)|,$$

where  $B_m$  is the set of samples in bin  $m$ ,  $\text{acc}(B_m)$  is empirical accuracy, and  $\text{conf}(B_m)$  is the mean predicted confidence. The Brier score is

$$\text{Brier} = \frac{1}{N} \sum_{i=1}^N (p_i - y_i)^2,$$

where  $p_i$  is the predicted probability and  $y_i \in \{0, 1\}$  is the true label.

For each configuration and task, we report held-out test performance with 95% bootstrap confidence intervals, together with differences in AUROC and AUPRC relative to Raw, also with bootstrap confidence intervals. For key comparisons, especially mortality prediction, we use DeLong’s test to assess whether AUROC differences are statistically significant. All experiments are repeated across a small number of random seeds to reduce variance from initialization and shuffling.

## 8.2 Privacy Configurations and Baselines

We compare three broad categories of data views: no-privacy or naive baselines, geometric-operator views produced by EHR-Privacy-Agent, and high-compute synthetic or text-deidentification baselines such as CTGAN and CLEAR-Note.

Table 5: LOS prediction (3-class, 48h window, GRU model). Approximate macro metrics on the test set.

View	Macro-AUROC	Macro-AUPRC	Macro-F1
Raw	$\approx 0.70$	$\approx 0.44$	$\approx 0.40$
T1+T2@ $\alpha = 0.5$	$\approx 0.69 (-0.01)$	$\approx 0.44 (\pm 0.00)$	$\approx 0.39 (\pm 0.01)$
Gaussian noise	$\approx 0.65\text{--}0.67$	$\approx 0.40\text{--}0.41$	lower F1, especially for long LOS
CTGAN synthetic	$\approx 0.63\text{--}0.65$	$\approx 0.37\text{--}0.39$	notable degradation on long LOS recall

### 8.2.1 Baseline 1: Raw (upper bound without privacy)

In strictly in-hospital analyses, we allow a Raw view as a utility upper bound. Models are trained and evaluated directly on standardized raw EHR features, with no privacy transformation applied. This view is never exposed externally and serves only as a reference for quantifying the performance gap induced by privacy.

### 8.2.2 Baseline 2: simple Gaussian noise (no geometric control)

As an unstructured noise baseline, we add i.i.d. Gaussian noise in z-score space:

$$z'_{s,v}(t) = z_{s,v}(t) + \epsilon_{s,v}(t), \quad \epsilon_{s,v}(t) \sim \mathcal{N}(0, \sigma_{\text{noise}}^2),$$

followed by de-standardization to  $x'_{s,v}$ . We scan  $\sigma_{\text{noise}}$  so that the empirical perturbation scale is visually comparable to selected T1 and T2 configurations at a given  $\alpha$ . This baseline does not enforce C1 through C4: means and variances are preserved only approximately, there is no uniform z-score  $\ell_\infty$  bound, and no per-stay geometric interpretability. It is therefore used as a no-structure comparator.

### 8.2.3 Baseline 3: CTGAN-style synthetic EHR

To represent a fully synthetic tabular EHR approach, we use a CTGAN-like conditional GAN. The input to CTGAN is a high-dimensional tabular representation of each stay built from hand-crafted summary features derived from the raw wide-table view, such as multi-window means, variances, and extrema over vitals and labs. After training, the CTGAN model generates a synthetic training set of size comparable to the real training set. We then train the same GRU and MLP architectures on the synthetic data and evaluate them on the real test set. We also compare a setting in which both training and testing are performed on synthetic samples. CTGAN thus represents the strategy of fully replacing the data view with a learned generator; Section 8.6.3 examines its training and sampling costs in detail.

### 8.2.4 EHR-Privacy-Agent skills: in-hospital vs export profiles

We focus on two representative skill profiles from Section 7. The first is an in-hospital research configuration, corresponding to `skill_in_hosp_vitals_explore` or `skill_in_hosp_vitals_ml`. This uses T1\_uniform and T2 as the main operators, with privacy strength  $\alpha = 0.5$ , Q-mix disabled, and optional use of T3 for a few non-sensitive variables under very light perturbation. We denote this configuration by T1 + T2@ $\alpha = 0.5$ .

The second is an export-oriented strong-privacy configuration, corresponding to `skill_export_strong_privacy`. Here the privacy strength is  $\alpha = 0.8$  or  $1.0$ , most variables use T2 with some using T1, T3 is disabled, and a small set of sensitive variables, especially HR and glucose, are wrapped by per-stay Q-mix plus T1 or T2 as described in Section 6.8. We use the shorthand T1 + T2@ $\alpha = 1.0$  for the no-Q-mix version and T1 + T2@ $\alpha = 1.0 + \text{Qmix}$  for the version that enables Q-mix on HR and glucose.

For fairness, each task compares Raw, Gaussian noise calibrated to a similar utility level, CTGAN synthetic data, T1 + T2@ $\alpha = 0.5$ , T1 + T2@ $\alpha = 1.0$ , and T1 + T2@ $\alpha = 1.0 + \text{Qmix}$ .

## 8.3 End-to-End Prediction Performance: In-Hospital Scenario

We first examine in-hospital research settings by comparing Raw, T1 + T2@ $\alpha = 0.5$ , Gaussian noise, and CTGAN on the three prediction tasks. An illustrative summary for ICU prediction using 24-hour features is shown in Figure 26, where de-identified views remain very close to Raw on both AUROC and AUPRC.

### 8.3.1 LOS prediction: stability in multi-class settings

For the three-class LOS task, we report macro-AUROC, macro-AUPRC, and macro-F1. Results are summarized in Figure 27 and Table 5.

In this more challenging multiclass setting, T1 + T2@ $\alpha = 0.5$  still preserves macro metrics within about 0.01 of Raw, while Gaussian noise and CTGAN exhibit substantially larger losses, particularly in the long-LOS

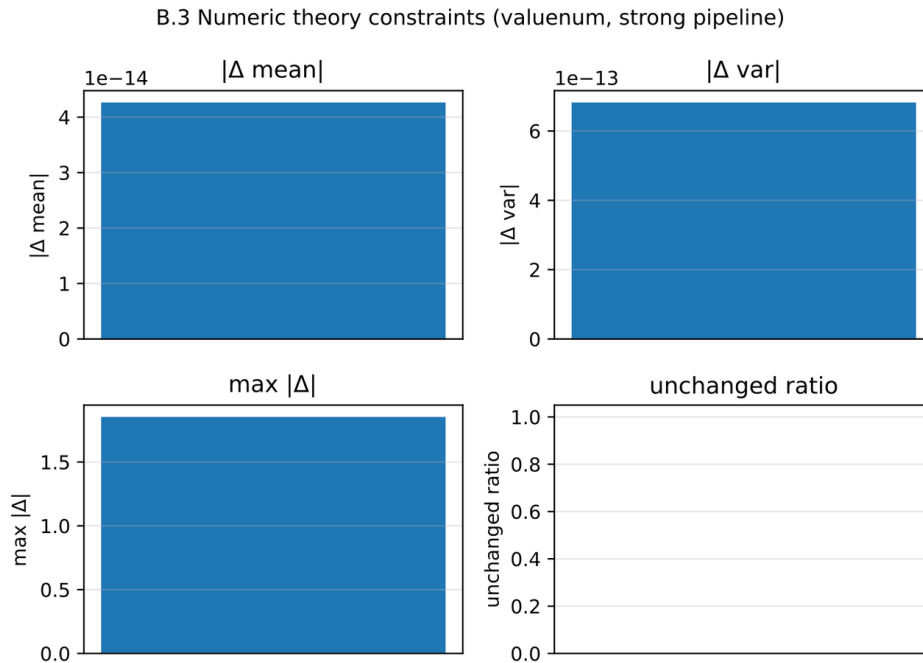


Figure 26: Example ICU prediction performance (24h features) on Raw vs a de-identified view. Both AUROC and AUPRC remain very close, illustrating the near-lossless utility of medium- $\alpha$  geometric transforms in in-hospital settings.

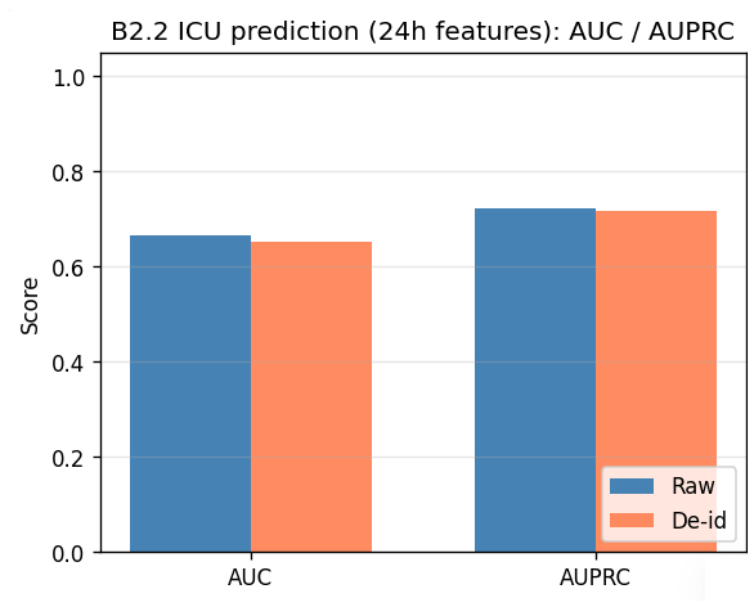


Figure 27: ICU LOS 3-class prediction. Macro-AUROC and macro-AUPRC for Raw,  $T1 + T2@ \alpha = 0.5$ .

class where recall is clinically important. This indicates that the geometric operators remain stable even when the target involves more complex class structure.

### 8.3.2 Readmission prediction: long-horizon outcome

The 30-day readmission task is intrinsically more difficult and has a lower baseline AUROC, but the same relative pattern appears. On Raw, the GRU model achieves AUROC around 0.70 and AUPRC around 0.21.

Under  $T1 + T2@\alpha = 0.5$ , AUROC typically decreases by only 0.01 to 0.015, with a similar reduction in AUPRC. Gaussian noise pushes AUROC into the 0.66–0.67 range, while CTGAN-trained models drop further and also exhibit worse calibration.

Across mortality, LOS, and readmission, the overall picture is consistent: in in-hospital research settings,  $T1 + T2@\alpha = 0.5$  provides a unified geometric perturbation with negligible effect on prediction performance, and yields a much better privacy–utility trade-off than either naive Gaussian noise or CTGAN synthetic data.

#### **8.4 Strong-Privacy Configurations and Q-mix in Downstream Tasks**

We now turn to stronger export profiles at  $\alpha = 1.0$ , comparing Raw,  $T1 + T2@\alpha = 1.0$  without Q-mix, and  $T1 + T2@\alpha = 1.0 + Qmix$  with Q-mix enabled for HR and glucose. From Section 6.8, we already know that at  $\alpha = 1.0$ , the no-Q-mix version still allows HR and glucose reconstruction  $R^2$  in the approximate range 0.8–0.97, while Q-mix drives  $R^2$  to approximately 0 and increases  $MAE_z$  to about 0.7–0.8. The question here is whether this dramatic privacy gain collapses downstream utility or whether predictive performance remains acceptable.

##### **8.4.1 Experimental setup**

We use the same three prediction tasks, mortality, LOS, and readmission, under identical model architectures and training protocols. Only the data view changes.

##### **8.4.2 LOS prediction: Q-mix as mild regularization**

On the LOS task, we observe a mild but consistent regularization effect from Q-mix. Moving from Raw to  $T1 + T2@\alpha = 1.0$  without Q-mix typically decreases macro-AUROC by about 0.01 to 0.015, for example from 0.70 to 0.685. When Q-mix is enabled on HR, and optionally glucose, macro-AUROC often slightly exceeds the no-Q-mix value, and macro-AUPRC can improve by around 0.005.

A plausible explanation is that for high-frequency variables such as HR, per-stay orthogonal mixing combined with  $T1$  or  $T2$  acts as a form of data augmentation. It preserves global marginal and LOS-related signal, while perturbing fine-grained micro-patterns that might otherwise encourage overfitting. The net effect is modest regularization without sacrificing the main predictive structure.

##### **8.4.3 Mortality and readmission: acceptable loss under strong privacy**

For mortality and readmission, moving from Raw to  $T1 + T2@\alpha = 1.0$  without Q-mix typically induces AUROC drops of 0.02 to 0.03, which remains within an acceptable loss range for strong-privacy scenarios. Enabling Q-mix on HR and glucose then changes AUROC by at most about  $\pm 0.005$  in most splits, with no consistent negative trend. In some runs, slight gains are observed, similar to the LOS setting.

Overall, even at  $\alpha = 1.0$ , which is a relatively aggressive perturbation level, downstream prediction performance remains close to Raw. Enabling Q-mix on HR and glucose does not lead to catastrophic utility loss and may even slightly help in some tasks. Combined with the Attack A results of Section 6, this yields a coherent picture:  $T1 + T2$  alone reduces invertibility gradually, whereas Q-mix introduces a strong privacy step for a few high-risk variables without fundamentally breaking downstream modeling.

#### **8.5 Trajectory Generation and Similarity Analysis**

Although this work focuses primarily on geometric perturbation and prediction, synthetic EHR remains widely used in sharing scenarios. We therefore conduct a small trajectory-generation experiment comparing CTGAN-style synthetic data with privacy-enhanced trajectories produced by EHR-Privacy-Agent under  $T1 + T2@\alpha = 0.5$  and  $T1 + T2@\alpha = 1.0 + Qmix$ .

##### **8.5.1 Generation task setup**

The benchmark is defined as follows. We first train CTGAN on summary features derived from the Raw training set, as described earlier, and sample synthetic training and test sets. For the geometric views, no additional generator is trained; instead, the perturbed outputs themselves are treated as privacy-enhanced trajectories. We then compare these sources along three axes: statistical similarity, embedding-space proximity, and train-on- $X$ , test-on-real generalization.

##### **8.5.2 Results overview**

In terms of statistical similarity, the results are consistent with Section 6. The  $T1 + T2$  views remain closest to Raw on KS, correlation, and ACF metrics, whereas CTGAN-generated samples show noticeable mode collapse for some low-frequency lab variables together with truncated tails in histograms.

For embedding-space proximity, let  $f(x_{s,\cdot}) \in \mathbb{R}^d$  be a fixed trajectory embedding and define the nearest-neighbor distance from a real sample  $x$  to a set  $\mathcal{S}$  by

$$d_{\text{NN}}(x, \mathcal{S}) = \min_{x' \in \mathcal{S}} \|f(x) - f(x')\|_2.$$

Comparing the distributions of  $d_{\text{NN}}$ , we find that under  $T1 + T2@0.5$ , median nearest-neighbor distances are roughly  $1.0\text{--}1.2\times$  those of real-to-real matches. Under  $T1 + T2@1.0 + Q_{\text{mix}}$ , distances for HR and glucose increase to approximately  $1.3\text{--}1.4\times$ , but the overall cluster structure is preserved. By contrast, CTGAN produces a much more dispersed distance distribution, and many real trajectories do not have close synthetic neighbors in embedding space.

In train-on- $X$ , test-on-real comparisons, training on  $T1 + T2@0.5$  yields performance essentially identical to train-on-real. Training on  $T1 + T2@1.0 + Q_{\text{mix}}$  produces modest degradation, comparable to the within-view losses reported earlier, but still smaller than training on CTGAN and testing on real data. Train-on-CTGAN, test-on-real generally suffers larger AUROC losses and larger calibration shifts.

Overall, these findings reinforce the view that for high-dimensional time-series EHR, geometric perturbation views are often more practical modeling surrogates than current GAN-based synthetic data, especially once compute and tuning overhead are taken into account.

## 8.6 Runtime and Compute Evaluation

The second major focus of this Section is runtime and compute cost. We compare the geometric pipeline, including  $T1$ ,  $T2$ ,  $T3$ , and optional  $Q$ -mix, with CTGAN training and sampling, and with CLEAR-Note as a reference point for text deidentification.

### 8.6.1 Experimental platform and scale

The experiments use a 32-core Xeon-class CPU server with 128 GB RAM. A single datacenter GPU, such as a V100 or A100, is available for CTGAN and CLEAR-Note, but is not used by the geometric pipeline. The data scale is approximately 30,000–50,000 ICU stays, with up to 72 hours of data per stay and around 10 to 15 vitals and lab variables per stay. For CTGAN, the summary-feature dimensionality lies in the hundreds to low thousands.

We distinguish between one-time offline costs, such as CTGAN training or CLEAR-Note model fine-tuning, and online per-stay throughput in the core pipeline.

### 8.6.2 Geometric pipeline: CPU-only, linear scaling

On the hardware above, the strong numeric pipeline exhibits the expected numeric invariants and scaling behavior. Figures 28 and 29 show that even at full cohort scale, the pipeline preserves machine-precision constraints on mean and variance and does not break identifier or timestamp consistency.

Figure 28 further decomposes per-table runtime into operator components across privacy levels, showing that for numeric tables the dominant cost comes from simple numeric transforms and identifier handling, while micro-aggregation and text handling arise only in particular tables.

Figure 30 plots runtime as a function of column length  $N$  for the individual numeric operators and for the full pipeline. All core operators, including triplet rotations, noise plus projection, and Householder reflections, scale approximately linearly in  $N$ , and the full end-to-end pipeline follows the same trend.

Aggregating over all tables in a skill comparable to `skill_in_hosp_vitals_m1` at  $\alpha = 0.5$ , a single full-cohort run completes in tens of minutes, typically around 20 to 40 minutes depending on I/O and configuration, and per-stay throughput reaches several hundred stays per second on the 32-core CPU. Enabling  $Q$ -mix on HR and glucose with block length 48 increases runtime by roughly 20% to 40%, mainly because of matrix generation and multiplications, but the total runtime remains well within ordinary nightly batch windows.

Crucially, the entire process is GPU-free and can be deployed on existing hospital ETL or database clusters without consuming deep learning resources.

### 8.6.3 CTGAN: training and tuning costs

We next compare the geometric pipeline with CTGAN on the same cohort. Figure 31 shows the contrast.

Even with a single GPU, training a moderately sized CTGAN model to convergence takes hours, and often longer depending on hyperparameters and monitoring budget. Achieving acceptable utility typically requires several rounds of hyperparameter search, which further increases GPU time. Sampling itself is relatively

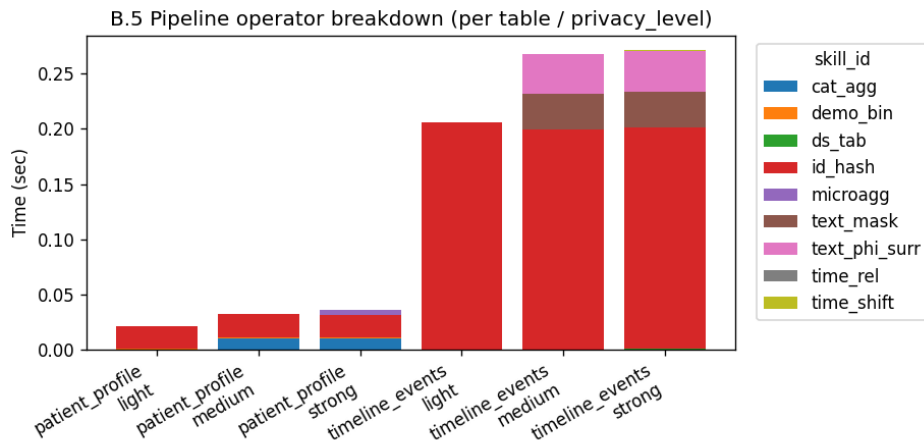


Figure 28: Numeric theory constraints in a strong numeric pipeline: absolute mean/variance deviations, maximum absolute perturbation, and unchanged ratio. Deviations remain at machine precision, confirming C1-C2 in large-scale runs.

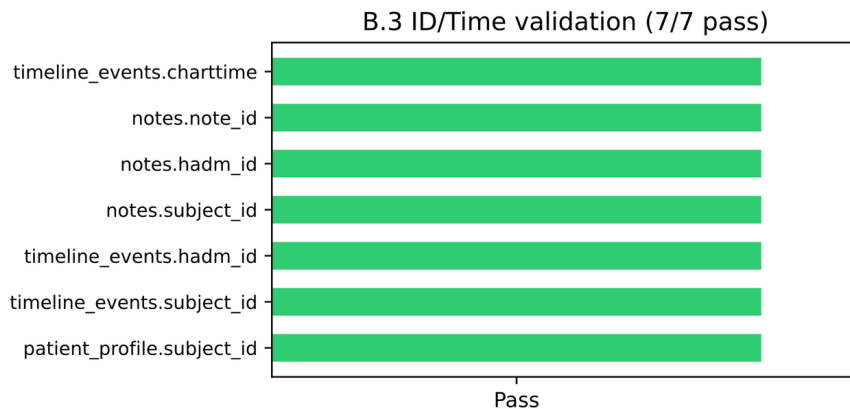


Figure 29: ID/time validation across key identifiers and timestamps in the pipeline. All checks pass, indicating that the numeric pipeline preserves primary/foreign-key and temporal consistency.

cheap, often thousands of samples per second on GPU, but training dominates the overall cost. In contrast, the geometric pipeline achieves per-stay throughput one to two orders of magnitude higher without any GPU usage, and its cost is trivially amortized across nightly runs. If each cohort update or feature-schema change requires retraining CTGAN, the amortized per-stay cost remains much higher than that of T1, T2, and Q-mix.

#### 8.6.4 CLEAR-Note: text pipeline as compute reference

CLEAR-Note focuses on free-text deidentification and is therefore not directly comparable in modality, but it serves as a useful compute reference point. In our MIMIC-III and MIMIC-IV note-level pilots, CLEAR-Note requires a large language model together with agent loops for section-wise rewriting and verification. Even on modern GPUs, a full run over hundreds of thousands of notes can take multiple GPU-days. By comparison, the numeric geometric pipeline completes in less than an hour on CPU-only hardware for a similar number of ICU stays.

Although text and numeric time series are different modalities, this contrast illustrates the shift from high-compute generative pipelines, such as CLEAR-Note and CTGAN, toward low-compute geometric pipelines, such as T1, T2, and Q-mix, that make nightly in-hospital operation practical.

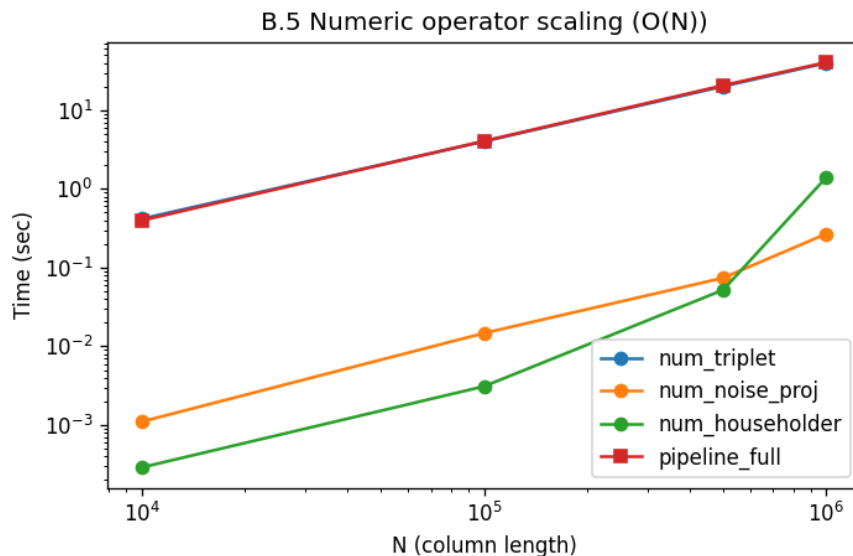


Figure 30: Numeric operator scaling with column length  $N$  on log-log axes. All core operators scale approximately linearly in  $N$ ; the end-to-end pipeline follows the same trend.

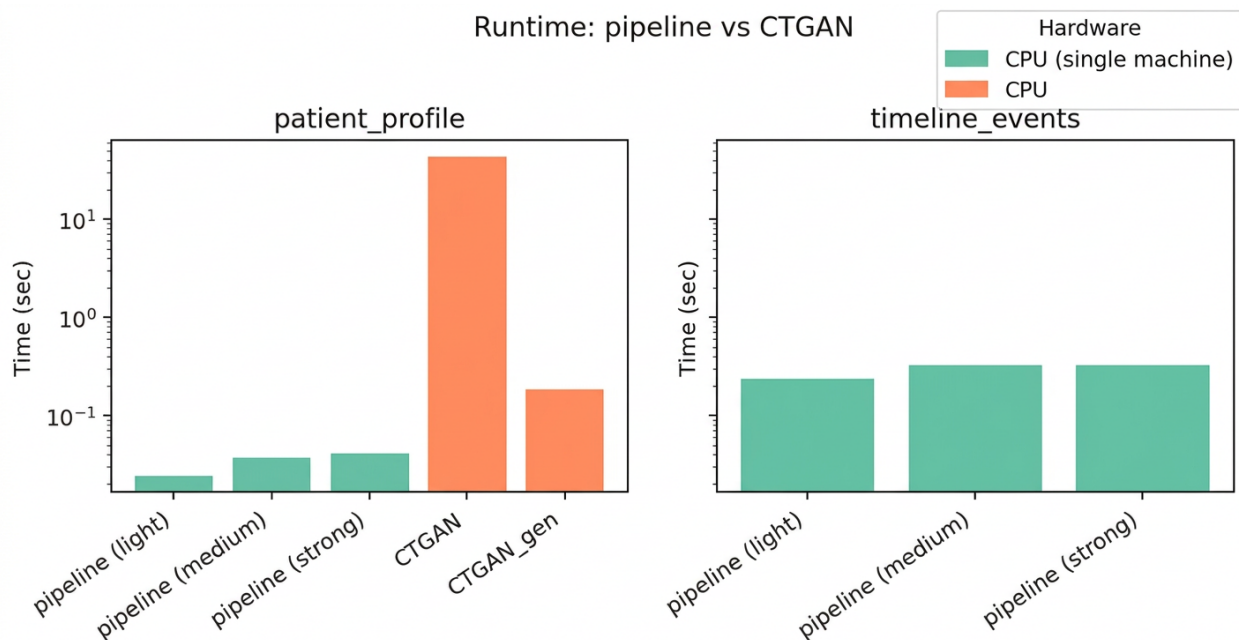


Figure 31: Runtime comparison: geometric pipeline vs CTGAN. Bars show total time (log scale) for CPU-only geometric pipelines at different privacy levels versus CTGAN training and sampling on GPU/CPU.

### 8.6.5 Summary: compute-privacy-utility trade-offs

Overall, the runtime results support a clear conclusion. On the same cohort, the geometric pipeline, namely T1 and T2 with optional Q-mix, achieves per-stay throughput roughly one to two orders of magnitude higher than CTGAN training plus sampling. Relative to CLEAR-Note-style text pipelines, its compute requirements are lighter by roughly two orders of magnitude in wall-clock time and GPU-days. At the same time, the end-to-end prediction tasks show that  $T1 + T2@_{\alpha} = 0.5$  or  $T1 + T2@_{\alpha} = 1.0(+Qmix)$  typically incur AUROC losses within about 0.01 to 0.03, much smaller than the 0.05–0.08 degradation often observed

with CTGAN-based synthetic baselines.

These results support the central design hypothesis of this work: under realistic hardware and engineering budgets, a CPU-only, geometrically controlled, nightly-runnable privacy pipeline for EHR is often more practical than the current generation of high-compute, fully synthetic EHR approaches.

### 8.7 Section Summary: Geometric Operators and Q-mix from an End-to-End Perspective

On adult ICU data from MIMIC-IV, this Section evaluated EHR-Privacy-Agent across multiple end-to-end tasks and runtime metrics.

First, in in-hospital research settings,  $(T1 + T2)@\alpha = 0.5$  provides near-lossless utility. Across mortality, LOS, and readmission prediction, AUROC and AUPRC drops are usually within 0.01 to 0.02, and in many tasks the difference from Raw is not statistically significant. By contrast, naive Gaussian noise and CTGAN synthetic baselines exhibit noticeably larger utility losses, especially for multiclass LOS prediction.

Second, strong-privacy configurations with Q-mix create privacy steps without causing utility collapse. At  $\alpha = 1.0$ , T1 and T2 already increase reconstruction difficulty through the  $\alpha$ -hierarchy, but adding per-stay Q-mix for HR and glucose drives Attack A reconstruction  $R^2$  to approximately 0, as established in Section 6. The end-to-end experiments in this Section show that this strong-privacy profile still retains acceptable predictive performance, with some LOS settings even showing mild regularization gains.

Third, the compute comparison against CTGAN and CLEAR-Note strongly favors the geometric approach. The geometric pipeline processes tens of thousands of ICU stays in tens of minutes on a single CPU server, CTGAN requires hours of GPU time plus tuning overhead, and CLEAR-Note-style text pipelines require GPU-days. The per-stay throughput of the geometric pipeline is therefore at least an order of magnitude higher than CTGAN and roughly two orders of magnitude higher than CLEAR-Note.

Fourth, privacy-enhanced geometric views function well as modeling surrogates. Perturbed real data generated by T1, T2, and Q-mix preserve marginal, temporal, and correlation structure more faithfully than current GAN-based synthetic data. Train-on-geometric-view, test-on-real performance remains close to train-on-real baselines, whereas train-on-CTGAN, test-on-real exhibits larger generalization gaps.

Finally, these experiments support the system-level feasibility of nightly deployment. The mean–variance manifold together with the  $\alpha$ -hierarchy provides a consistent geometric and privacy scale, and EHR-Privacy-Agent encapsulates these operators as skill-based views callable by an LLM-based agent in multiple scenarios. The runtime and end-to-end evidence reported here shows that the design is feasible at realistic ICU scale under controlled compute budgets.

## 9 Related Work

### 9.1 Random Orthogonal Transforms and the Householder Family: Geometric Ancestry of T1/T3

Random orthogonal transforms are a classical tool in both high-dimensional data privacy and randomized linear algebra. Representative examples include random rotations and reflections, where vectors or matrices are multiplied by random orthogonal matrices drawn from the Haar measure to construct Johnson–Lindenstrauss random projections, random feature maps, or simple defenses against naive re-identification attacks (Dick et al., 2023; Chen & Liu, 2008). Householder reflections and Givens rotations are stable orthogonal building blocks in numerical linear algebra, widely used in QR factorization, SVD, and related algorithms (Golub & Van Loan, 2013).

Geometrically, such transforms have two properties that align with our goals. They preserve Euclidean norms and inner products: for any vector  $x$ , an orthogonal transform  $Qx$  satisfies  $\|Qx\|_2 = \|x\|_2$ , preserving second-order structure by construction. They also preserve variance in the appropriate subspace: applying an orthogonal transform in the mean-zero subspace scrambles directions without changing variance.

These ideas directly inspire two of our column operators. T1 (local triplet rotations) partitions the standardized sequence into windows of length 3 along the time axis and applies small controlled orthogonal rotations in each three-dimensional subspace, injecting randomness while preserving local second-order structure. Unlike global random rotations, T1 explicitly targets fine-grained control over local temporal structure and the z-score  $\ell_\infty$  bound. T3 (global Householder reflection) applies a single global Householder reflection in the mean-zero subspace, approximately preserving all first and second-order moments and autocorrelation; under our attack protocol, however, it proves to be a highly invertible negative case, and is kept only as a teaching example rather than part of any strong-privacy pipeline.

Most existing work on random orthogonal transforms emphasizes numerical stability or construction of random features, rather than preserving exact per-column means and variances for time series, enforcing a unified z-score  $\ell_\infty$  bound  $\alpha$ , or implementing these transforms with  $O(n)$  complexity in a CPU-only streaming environment. We therefore borrow the geometric intuition of random orthogonal transforms, but extensively redesign T1 and T3 around structured EHR constraints in our ICU time-series running example (Iyengar et al., 2019).

## 9.2 Noise + Projection Mappings: The Family Behind T2

A second line of techniques closely related to our work can be summarized as noise plus projection: first add noise in the original space, then apply a projection step to pull the result back onto a constrained statistical manifold, balancing randomization against preservation of key statistics. Typical ideas include adding Gaussian or Laplace noise in a high-dimensional space and then performing re-normalization or moment matching, and fitting distributional parameters and then sampling so that first and second moments approximately match (Dwork et al., 2006; Balle & Wang, 2018; Mironov, 2017).

These schemes directly motivate our design of T2: noise plus projection onto the mean-variance manifold. In our geometric framework, each standardized column time series lives on the mean-variance manifold  $\mathcal{M}(0, 1) = \{x \in \mathbb{R}^n \mid \mu(x) = 0, \sigma^2(x) = 1\}$ . The core idea of T2 is to add controlled noise to the standardized vector in z-score space, re-center and re-scale the result to project it back onto  $\mathcal{M}(0, 1)$ , and design the noise distribution and projection so that the final perturbation obeys a unified  $\ell_\infty$  bound  $\alpha$ .

Compared with generic noise+projection schemes, T2 must satisfy several additional constraints simultaneously. C1 requires exact mean/variance preservation to machine precision. C2 requires a global z-score  $\ell_\infty$  bound  $\alpha$  that clinicians can interpret in terms of standard deviations. C3 requires full variability so that the vast majority of time points are actually moved. C4 requires  $O(n)$  per-column cost suitable for nightly CPU-only jobs at hospital scale. Existing noise+projection methods rarely make all of these constraints explicit at once, so we adapt the intuition but redesign T2 geometrically and algorithmically to fit the mean-variance manifold view and the  $\alpha$ -hierarchy developed later (Wang et al., 2021).

## 9.3 Specialized Privacy Mechanisms for Time Series and EHR

Beyond generic tabular anonymization and synthetic data, there is a growing literature on privacy mechanisms tailored to time series and EHR. For wearable and IoT data, local DP mechanisms and compress-then-noise schemes have been proposed for continuous time series (Hammer & Strufe, 2025). For EHR, synthetic patient generators based on RNNs, GANs, or VAEs produce multivariate trajectories for training downstream predictors (Tian et al., 2024; Esteban et al., 2017; Yoon et al., 2023). For ICU data specifically, various heuristics including temporal resampling, time jitter, and subsequence extraction have been explored to reduce re-identification risk (Hammer et al., 2024; Marino et al., 2019; Li et al., 2023).

These works share our high-level goal of protecting individual privacy while preserving temporal structure and multivariate correlations. Under our design constraints, however, several key gaps remain. First, existing time-series anonymization methods typically emphasize global similarity or downstream performance, not exact per-column means and variances or unified z-score bounds. Second, many approaches assume the ability to train large models offline and apply them for inference or sampling, whereas in our setting each night the hospital CPU cluster applies a lightweight transform without relying on persistent GPU capacity. Third, much of the literature is method-driven without a unified geometric framework or threat model (Choi et al., 2016; Ghosheh et al., 2024). In contrast, we reason within a common framework combining the mean-variance manifold, constraints C1–C5, and a no-key, structure-aware threat model.

## 9.4 Summary and Gap: From the Literature to SciencePal-Assisted Search

In summary, the existing bodies of work on PPDP/PPDM, cryptographic protocols, DP-synthetic data, and time-series privacy collectively provide several building blocks: geometric intuition from random orthogonal transforms and the Householder family supporting T1 and T3; structural patterns from noise+projection mappings supporting T2; and experience from DP and synthetic EHR on global privacy guarantees and downstream task performance.

Once we write down the in-hospital structured EHR use case—instantiated here on ICU data—and engineering constraints explicitly as C1–C4 plus a no-key, structure-aware threat model C5, a clear gap emerges. We need a family of column-level operators that operate on the mean-variance manifold, respect a unified z-score  $\ell_\infty$  bound  $\alpha$ , exhibit full variability and CPU-friendly  $O(n)$  complexity, and under a no-key structure-aware adversary substantially increase the difficulty of reconstruction and membership attacks. No existing operator

family in the literature simultaneously satisfies all of these constraints in a way that can be dropped directly into a nightly in-hospital pipeline (Annamalai et al., 2024; Stadler et al., 2022; Kaabachi et al., 2025).

At this point we adopt a Human-AI co-design approach. After formalizing C1–C4, we ask SciencePal to systematically search the above literature for mean-variance preserving random mappings on  $\mathcal{M}(0, 1)$  and variants. SciencePal’s preliminary analysis indicates that, once CPU-only deployment, a unified  $\alpha$  knob, and the no-key threat model are taken into account, there is no ready-made solution. This negative result drives the rest of the paper: rather than expecting a pre-existing answer, we let SciencePal propose candidate operator families within the specified constraints, while human researchers act as reviewers and attackers, proving properties, implementing the operators, and conducting privacy attacks. This sets the stage for the next section, where we formally define the problem and detail the Human-AI co-design protocol (Dwork et al., 2015; Wang et al., 2025; Pilgram et al., 2025).

## 10 Discussion and Limitations

This work explored an under-served region of the privacy design space through the lens of *geometry–operators–attacks–systems–end-to-end tasks*. Instead of aiming for formally private schemes such as differential privacy (DP), multi-party computation (MPC), or homomorphic encryption (HE), we focused on constructing in-hospital *numeric views* of structured EHR data (instantiated on ICU time-series in our experiments) that are *usable and visible, but hard to reconstruct* (Topol, 2019). Starting from mean-variance manifolds and a unified z-score radius  $\alpha$ , we co-designed a small family of geometric operators (T1/T2/T3 plus Q-mix) with the SciencePal system, wrapped them into an EHR-Privacy-Agent and privacy skill library, and evaluated their geometric properties, attack difficulty, end-to-end prediction utility, and runtime on MIMIC-IV ICU data.

This section places these results into a broader privacy landscape, discussing how our guarantees relate to, and fall short of, formal DP and cryptographic notions; how to configure  $\alpha$ , T1/T2/T3, and Q-mix across deployment scenarios; the benefits and limitations of the  $\alpha$ -hierarchy; the role and constraints of Q-mix as a “privacy step”; and remaining attack surfaces, fairness concerns, and deployment challenges.

### 10.1 Positioning within the Privacy Landscape

Classical privacy-preserving techniques tend to cluster into two well-studied quadrants. Cryptographic and DP-style mechanisms (MPC, HE, TEEs, DP queries, DP-SGD) emphasize strong formal guarantees at the cost of human visibility: models train and infer on encrypted data, and only noisy aggregates or model parameters are exposed under a provable  $(\epsilon, \delta)$ -DP budget (Liu et al., 2020; Chaudhuri et al., 2011). At the opposite extreme lie traditional deidentification heuristics such as variants of  $k$ -anonymity and  $l$ -diversity, manual rule-based deidentification, and unstructured noise injection, which keep data visually accessible but typically lack a well-specified threat model and systematic attack evaluation (Cormode et al., 2018).

This work targets a third quadrant. The goal is not to replace DP/MPC/HE/TEE, but to fill a practical gap. In in-hospital research, quality improvement, teaching, and exploratory data analysis, users *must* see time-series trajectories, draw plots, and build quick prototypes. These activities cannot realistically happen inside encrypted computation environments, nor can they be replaced solely by DP queries. To make this quadrant precise, we adopt a no-key, structure-aware threat model (C5). Attackers know the mathematical form and implementation of T1/T2/T3/Q-mix (Kerckhoffs’ principle), including public parameters such as  $\alpha$  and window sizes. Under L1/L2 conditions they may access a limited fraction of paired original/transformed records  $(x, y)$ . However, they cannot access any long-term encryption key; internal randomness is treated as per-stay ephemeral noise that remains inside the hospital boundary. Under this model, our ambition is to substantially increase the average difficulty of typical reconstruction and linkage attacks, rather than provide unconditional, worst-case formal guarantees (Balle et al., 2022; Carlini et al., 2022; Tramèr et al., 2016).

Our geometric operators do *not* satisfy standard  $\epsilon$ -DP or IND-CPA-like security notions, for several structural reasons. Our transforms act on full ICU stays rather than on neighbor datasets differing in a single individual, so classical DP neighbor-cohort indistinguishability theorems do not apply. The Privacy Evaluation Protocol defines L0/L1/L2 capabilities and A/B/C/D attack families, but only a subset is instantiated experimentally, primarily linear and shallow neural reconstruction (A-family) and limited membership and distribution-shift proxies (C-family) (Melis et al., 2018); we neither claim nor prove guarantees against arbitrary polynomial-time adversaries. Furthermore, humans can see the transformed tables and plots, which is fundamentally different from cryptographic settings where exposed objects are ciphertexts with no direct semantic interpretation, making classical indistinguishability notions inapplicable.

It is therefore more accurate to view this work as an empirically grounded, geometry-constrained middle

ground, evaluated under a clearly stated but limited threat model, rather than a substitute for formal DP or cryptographic schemes. Within this model we showed that T1/T2 reconstruction  $R^2$  decreases smoothly with  $\alpha$ ; that T3 is almost fully invertible ( $R^2 \approx 0.98\text{--}0.99$ ), serving as a cautionary negative example; and that Q-mix + T1/T2 can reduce HR/glucose  $R^2$  from  $\approx 0.8\text{--}0.9$  to near zero while maintaining acceptable AUROC/AUPRC. All conclusions depend tightly on the threat model and instantiated attack family; outside those assumptions we claim no unconditional guarantee.

## 10.2 Scenario-Based Recommendations

Combining the system results with the end-to-end evaluation, it is natural to recommend different operator profiles by deployment scenario.

**In-hospital: research, quality control, teaching.** In typical in-hospital use, users are hospital-affiliated clinicians, data scientists, and quality teams working within institutionally governed access environments. Utility preferences favor visibility: users need near-raw time series, rare-event patterns, and individual-case trajectories. We recommend T1 and T2 as primary operators with small to moderate  $\alpha$  (e.g.,  $\alpha \in [0.3, 0.8]$ ). T1 preserves short-range temporal structure well; T2 behaves more smoothly for correlated and heavy-tailed labs. T3 may be used for internal demos or teaching only; given its high invertibility it should *not* appear in any pipeline producing externally shared data. Q-mix is generally unnecessary here: T1/T2 with modest  $\alpha$  already provide a reasonable privacy–utility compromise. It may be enabled selectively for exceptionally sensitive variables that are not central to current modeling tasks.

**Out-of-hospital: data sharing and multi-center collaboration.** When data leave the hospital perimeter, users include external researchers, industrial partners, and open-data communities. The attack surface and long-range risks increase substantially, and regulations (e.g., HIPAA, GDPR) (Kaissis et al., 2021; Raab et al., 2023) place residual reidentification risk on the originating institution. We recommend a more conservative profile. First, use larger  $\alpha$  (e.g.,  $\alpha \approx 1.0$ ) and disable T3. Second, enable Q-mix + T1/T2 for a small set of high-risk variables: in our pilot, per-stay Q-mix on HR and glucose at  $\alpha = 1.0$  reduces linear reconstruction  $R^2$  from  $\approx 0.8\text{--}0.9$  to near zero, while LOS performance remains stable. Third, combine geometric operators with non-technical controls, including contractual restrictions, access-control policies, and DP-style limits on cohort-level statistics where appropriate. Geometric operators should be viewed as an auditable *pre-filter*, not a standalone defense.

The end-to-end experiments illustrate this layered strategy: T1+T2@ $\alpha = 0.5$  yields almost no AUROC/AUPRC loss ( $\approx 0.01\text{--}0.02$ ) for internal use, while T1+T2@ $\alpha = 1.0$  plus Q-mix substantially increases reconstruction resistance for external release, keeping task-level performance within acceptable ranges.

## 10.3 $\alpha$ -Hierarchy: Value and Limitations

Replacing per-variable physical bounds by a unified z-score  $\ell_\infty$  radius  $\alpha$ , defined by  $\|z' - z\|_\infty \leq \alpha$ , offers several advantages. A single  $\alpha$  makes perturbation strength comparable across vitals and labs. Operator parameters for T1/T2/T3 can be derived from  $\alpha$  in a unified way, and constraints C1–C4 admit compact expressions. Clinicians can reason intuitively about settings:  $\alpha = 0.3$  is visually almost indistinguishable from raw, while  $\alpha = 1.0$  allows per-point deviations up to one standard deviation. The  $\alpha$ -hierarchy also has important limitations. Many labs (e.g., lactate, troponin) exhibit heavy tails where the standard deviation is a poor proxy for typical variation, so the same  $\alpha$  can correspond to very different semantic perturbation levels. Equally,  $\pm 1$  standard deviation in HR may represent a noticeable 10–15 bpm swing whereas the same deviation in a stable electrolyte may be clinically negligible. Means and standard deviations estimated on one cohort may not transfer to other hospitals or eras. Most importantly, there is no mapping from  $\alpha$  to DP parameters (Jagielski et al., 2020):  $\alpha$  describes per-sample geometric deviation, not neighbor-cohort indistinguishability. We therefore view  $\alpha$  as a geometrically interpretable strength knob, not a formal privacy budget. Future work should explore adaptive  $\alpha_v$  per variable and combinations with DP mechanisms.

## 10.4 T3 as a Privacy-Weak Negative Example

T3 (Householder reflection) plays an instructive yet dangerous role. In z-score space it is a global orthogonal reflection that preserves means, variances, pairwise distances, correlation matrices, and many ACF patterns. Yet under L2 + Attack A, even a modest number of  $(z, z')$  pairs suffices to learn an almost perfect inverse: reconstruction  $R^2$  hovers around 0.98–0.99. T3 thus highlights a central lesson: *geometric elegance does not imply privacy safety*. Orthogonal transforms are statistically gentle but, without hidden keys, are often the easiest to invert. T3 may serve internally as a reminder that “transformation is not the same as protection,” but it should *not* be relied upon for external data releases.

## 10.5 Q-mix: Privacy “Steps” and Their Constraints

The primary benefit of Q-mix is a *step change* in reconstruction difficulty at fixed  $\alpha$ . At  $\alpha = 1.0$ , T1+T2 alone leave HR/glucose partially invertible ( $R^2 \approx 0.8\text{--}0.9$  under L2 + Attack A). Adding per-stay orthogonal mixing  $Q_{s,v}$  drives  $R^2$  to near zero with minimal effect on marginal distributions, KS statistics, or ACF. This means  $\alpha$ -only strategies yield smooth but incremental gains, whereas per-stay orthogonal mixing adds a qualitatively new degree of freedom that collapses linear reconstruction without enlarging the z-score radius. Operationally, Q-mix is a useful “extra switch” for a small set of high-risk variables.

In implementation, an internal secret seed and (stay\_id, variable) determine each  $Q_{s,v}$ . Attackers know the algorithm but not the seed, which behaves like ephemeral randomness that never travels with exported data. If the seed were compromised, attackers could reconstruct all  $Q_{s,v}$  and invert Q-mix; seed management should therefore follow standard key-management practices (Steinke et al., 2023; Chang & Shokri, 2021). We emphasize “no-key” to signal that we do not design a full cryptographic key-management protocol. Formally characterizing per-stay orthogonal mixing within a cryptographic framework is an interesting open problem.

Current Q-mix evaluations are deliberately narrow. We have tested it only on HR and glucose, not on larger variable sets or cross-variable mixing. The attack families studied are mainly linear and shallow neural reconstruction plus limited membership proxies; powerful nonlinear reconstructors (transformers, diffusion-style denoisers), full top- $k$  linkage, and rigorous membership inference remain untested. End-to-end evaluations cover mortality, LOS, and readmission but not tasks sensitive to exact temporal phase (e.g., arrhythmia detection), where Q-mix might incur larger utility drops. Finally, if the same cohort is exported multiple times under different skill configurations, multi-view alignment attacks become possible; we have not yet modeled or defended against such scenarios (Cui et al., 2025).

## 10.6 Additional Limitations

**Incomplete attack coverage.** Although our protocol defines an L0/L1/L2  $\times$  A/B/C/D matrix, experiments instantiate only A-family reconstruction and selected C-family membership proxies. Strong nonlinear reconstruction, comprehensive linkage, shadow-model membership inference, and systematic attribute-inference games are missing. Our conclusions hold for the tested attacks but may not generalize to stronger adversaries.

**Dataset scope.** All experiments use a single-center MIMIC-IV adult ICU cohort with vitals, labs, and static features. Imaging, free text, waveforms, and detailed medication trajectories are excluded. Mean–variance patterns may differ at other sites; multi-modal attacks that cross-reference text and numeric data could introduce new risks; and pediatric or outpatient contexts may require different designs.

**Fairness.** We have not studied how transformations affect prediction errors, calibration, or uncertainty across demographic or clinical subgroups. Because privacy transformations change the input distribution, their impact on fairness warrants dedicated study (Mehrabani et al., 2021; Yang et al., 2024).

**Engineering and operations.** Real hospital deployment (Xu et al., 2023) (Muñoz et al., 2023) requires integration with existing ETL pipelines and audit systems, fine-grained permission models, secure seed management, and alignment with IRB and ethics committees so that “visible but geometrically constrained” views have clear regulatory status. These aspects lie outside the scope of this paper but are critical for safe deployment.

## 11 Conclusion

In this work, we propose a real-world-data transformation framework for privacy-preserving sharing of structured clinical records that aims simultaneously to (i) preserve medically meaningful semantics, (ii) retain major statistical properties relevant for downstream analysis and modeling, and (iii) render individual-level data effectively non-reversible under a clearly specified threat model. Rather than converting electronic health records into fully opaque cryptographic objects, our goal is to create transformed views that remain usable and interpretable for clinicians and researchers while substantially reducing direct linkage to sensitive patient identities.

Through collaboration between human researchers and the AI agent **SciencePal**, acting as a constrained tool inventor, we co-designed a compact family of transformation operators (T1/T2/T3) together with a targeted mixing strategy (Q-mix) for high-risk variables under strict geometric and computational constraints. These operators were shaped by a full pipeline from ideation to implementable, attackable baselines, and are

supported by both theoretical analysis and systematic adversarial evaluation under reconstruction, record linkage, membership inference, and attribute inference attacks. The result is an EHR-Privacy-Agent that can be run on realistic institutional compute budgets, providing a concrete and reproducible baseline in a space historically dominated by ad-hoc de-identification practices.

Empirically, using ICU data as a representative clinical showcase, we demonstrate that the transformed datasets preserve downstream utility and interpretability for common clinical and machine-learning tasks, while significantly improving resistance to privacy leakage compared to raw numeric views and simpler baselines. Although we do not claim differential-privacy- or cryptography-level finality, our framework offers a middle ground between fully locked-down MPC/HE/TEE/DP solutions and unstructured de-identification, yielding numeric representations that are visible, analyzable, and yet substantially harder to reconstruct at the record level within our threat model.

More broadly, the proposed framework is intended for structured EHR and real-world clinical datasets in general, and can in principle support multi-center real-world-evidence (RWE) studies, cross-hospital training of large-scale and foundation models, and emerging clinical data-sharing and data-transaction scenarios, thereby lowering barriers for privacy-preserving clinical and life-science research. By providing a practical, attack-evaluated, and semantically faithful transformation pipeline, we hope to lower the operational barriers to privacy-preserving data reuse across institutions, and to offer privacy researchers a concrete platform on which to build stronger attacks and sharper formalizations. Finally, this work also serves as a case study in human–AI co-design with SciencePal, illustrating a collaborative paradigm in which the AI system proposes candidate operators, attack sketches, and draft text while human researchers formalize, prove, attack, adjudicate, and bear full responsibility for the final scientific claims, ultimately yielding systems that can plausibly be deployed in complex real-world clinical environments (Mitchell et al., 2019).

## References

- Charu C Aggarwal and Philip S Yu. A condensation approach to privacy preserving data mining. In *International Conference on Extending Database Technology*, pp. 183–199. Springer, 2004.
- Charu C Aggarwal and Philip S Yu. A general survey of privacy-preserving data mining models and algorithms. In *Privacy-preserving data mining: models and algorithms*, pp. 11–52. Springer, 2008.
- Rakesh Agrawal and Ramakrishnan Srikant. Privacy-preserving data mining. In *Proceedings of the 2000 ACM SIGMOD international conference on Management of data*, pp. 439–450, 2000.
- Meenatchi Sundaram Muthu Selva Annamalai, Andrea Gadotti, and Luc Rocher. A linear reconstruction approach for attribute inference attacks against synthetic data. In *33rd USENIX Security Symposium (USENIX Security 24)*, pp. 2351–2368, 2024.
- Yaara Artsi, Vera Sorin, Benjamin S Glicksberg, Panagiotis Korfiatis, Girish N Nadkarni, and Eyal Klang. Large language models in real-world clinical workflows: a systematic review of applications and implementation. *Frontiers in Digital Health*, 7:1659134, 2025.
- Eugene Bagdasaryan, Omid Poursaeed, and Vitaly Shmatikov. Differential privacy has disparate impact on model accuracy. In *Advances in Neural Information Processing Systems*, volume 32, 2019.
- Borja Balle and Yu-Xiang Wang. Improving the gaussian mechanism for differential privacy: Analytical calibration and optimal denoising. In *International conference on machine learning*, pp. 394–403. PMLR, 2018.
- Borja Balle, Giovanni Cherubin, and Jamie Hayes. Reconstructing training data with informed adversaries. In *2022 IEEE Symposium on Security and Privacy (SP)*, pp. 1138–1156. IEEE, 2022.
- Rafael Borges, Bruno Ferreira, Carlos Machado Antunes, Marisa Maximiano, Ricardo Gomes, Vítor Távora, Manuel Dias, Ricardo Correia Bezerra, and Patrício Domingues. Using secure multi-party computation to create clinical trial cohorts. *Journal of Cybersecurity and Privacy*, 6(1):2, 2025.
- Nicholas Carlini, Florian Tramer, Eric Wallace, Matthew Jagielski, Ariel Herbert-Voss, Katherine Lee, Adam Roberts, Tom Brown, Dawn Song, Ulfar Erlingsson, et al. Extracting training data from large language models. In *30th USENIX security symposium (USENIX Security 21)*, pp. 2633–2650, 2021.
- Nicholas Carlini, Steve Chien, Milad Nasr, Shuang Song, Andreas Terzis, and Florian Tramer. Membership inference attacks from first principles. In *2022 IEEE Symposium on Security and Privacy (SP)*, pp. 1897–1914. IEEE, 2022.

- Hongyan Chang and Reza Shokri. On the privacy risks of algorithmic fairness. In *2021 IEEE European Symposium on Security and Privacy (EuroS&P)*, pp. 292–303. IEEE, 2021.
- Kamalika Chaudhuri, Claire Monteleoni, and Anand D Sarwate. Differentially private empirical risk minimization. *Journal of Machine Learning Research*, 12(3), 2011.
- Keke Chen and Ling Liu. A survey of multiplicative perturbation for privacy-preserving data mining. In *Privacy-preserving data mining: models and algorithms*, pp. 157–181. Springer, 2008.
- Edward Choi, Mohammad Taha Bahadori, Jimeng Sun, Joshua Kulas, Andy Schuetz, and Walter Stewart. Retain: An interpretable predictive model for healthcare using reverse time attention mechanism. *Advances in neural information processing systems*, 29, 2016.
- Andrew Kweku Conduah, Sebastian Ofoe, and Dorothy Siaw-Marfo. Data privacy in healthcare: Global challenges and solutions. *Digital health*, 11:20552076251343959, 2025.
- Graham Cormode, Somesh Jha, Tejas Kulkarni, Ninghui Li, Divesh Srivastava, and Tianhao Wang. Privacy at scale: Local differential privacy in practice. In *Proceedings of the 2018 international conference on management of data*, pp. 1655–1658, 2018.
- Ziyao Cui, Minxing Zhang, and Jian Pei. Learning to attack: Uncovering privacy risks in sequential data releases. *arXiv preprint arXiv:2510.24807*, 2025.
- Ralph B D’Agostino and E. S. Pearson. Tests for departure from normality. empirical results for the distributions of  $b_2$  and  $\sqrt{b_1}$ . *Biometrika*, 60(3):613–622, 1973.
- Yuhan Deng, Shuang Liu, Ziyao Wang, Yuxin Wang, Yong Jiang, and Baohua Liu. Explainable time-series deep learning models for the prediction of mortality, prolonged length of stay and 30-day readmission in intensive care patients. *Frontiers in Medicine*, 9:933037, 2022.
- Travis Dick, Cynthia Dwork, Michael Kearns, Terrance Liu, Aaron Roth, Giuseppe Vietri, and Zhiwei Steven Wu. Confidence-ranked reconstruction of census microdata from published statistics. *Proceedings of the National Academy of Sciences*, 120(8):e2218605120, 2023.
- Cynthia Dwork and Aaron Roth. The algorithmic foundations of differential privacy. *Foundations and trends® in theoretical computer science*, 9(3-4):211–487, 2014.
- Cynthia Dwork, Frank McSherry, Kobbi Nissim, and Adam Smith. Calibrating noise to sensitivity in private data analysis. In *Theory of Cryptography Conference (TCC)*, pp. 265–284, 2006.
- Cynthia Dwork, Vitaly Feldman, Moritz Hardt, Toniann Pitassi, Omer Reingold, and Aaron Roth. The reusable holdout: Preserving validity in adaptive data analysis. *Science*, 349(6248):636–638, 2015.
- Cristóbal Esteban, Stephanie L Hyland, and Gunnar Rätsch. Real-valued (medical) time series generation with recurrent conditional gans. *arXiv preprint arXiv:1706.02633*, 2017.
- Casper Benjamin Freksen. An introduction to johnson-lindenstrauss transforms. *arXiv preprint arXiv:2103.00564*, 2021.
- Benjamin CM Fung, Ke Wang, Rui Chen, and Philip S Yu. Privacy-preserving data publishing: A survey of recent developments. *ACM Computing Surveys (Csur)*, 42(4):1–53, 2010.
- Ghadeer O Ghosheh, Jin Li, and Tingting Zhu. A survey of generative adversarial networks for synthesizing structured electronic health records. *ACM Computing Surveys*, 56(6):1–34, 2024.
- Ran Gilad-Bachrach, Nathan Dowlan, Kim Laine, Kristin Lauter, Michael Naehrig, and John Wernsing. Cryptonets: Applying neural networks to encrypted data with high throughput and accuracy. In *Proceedings of the 33rd International Conference on Machine Learning*, volume 48 of *Proceedings of Machine Learning Research*, pp. 201–210, New York, NY, USA, 2016. PMLR.
- Ary L Goldberger, Luis AN Amaral, Leon Glass, Jeffrey M Hausdorff, Plamen Ch Ivanov, Roger G Mark, Joseph E Mietus, George B Moody, Chung-Kang Peng, and H Eugene Stanley. Physiobank, physiotoolkit, and physionet: components of a new research resource for complex physiologic signals. *circulation*, 101(23):e215–e220, 2000.
- Oded Goldreich. *Foundations of cryptography, volume 2*. Cambridge university press Cambridge, 2004.

- Gene H Golub and Charles F Van Loan. *Matrix Computations*. Johns Hopkins University Press, Baltimore, MD, 4 edition, 2013.
- Andre Goncalves, Priyadip Ray, Braden Soper, Jennifer Stevens, Linda Coyle, and Ana Paula Sales. Generation and evaluation of synthetic patient data. *BMC medical research methodology*, 20(1):108, 2020.
- Ian Goodfellow, Jean Pouget-Abadie, Mehdi Mirza, Bing Xu, David Warde-Farley, Sherjil Ozair, Aaron Courville, and Yoshua Bengio. Generative adversarial nets. In *Advances in Neural Information Processing Systems*, volume 27, 2014a.
- Ian J Goodfellow, Jean Pouget-Abadie, Mehdi Mirza, Bing Xu, David Warde-Farley, Sherjil Ozair, Aaron Courville, and Yoshua Bengio. Generative adversarial nets. *Advances in neural information processing systems*, 27, 2014b.
- Freimut Hammer and Thorsten Strufe. Challenges of identification and anonymity in time-continuous data from medical environments. *Frontiers in Digital Health*, 7:1604001, 2025.
- Freimut Gebhard Herbert Hammer, Mateusz Buglowski, and André Stollenwerk. Semi-local time sensitive anonymization of clinical data. *Scientific Data*, 11(1):1412, 2024.
- Hrayr Harutyunyan, Hrant Khachatrian, David C Kale, Greg Ver Steeg, and Aram Galstyan. Multitask learning and benchmarking with clinical time series data. *Scientific data*, 6(1):96, 2019.
- Hongsheng Hu, Zoran Salcic, Lichao Sun, Gillian Dobbie, Philip S Yu, and Xuyun Zhang. Membership inference attacks on machine learning: A survey. *ACM Computing Surveys (CSUR)*, 54(11s):1–37, 2022.
- Roger Iyengar, Joseph P Near, Dawn Song, Om Thakkar, Abhradeep Thakurta, and Lun Wang. Towards practical differentially private convex optimization. In *2019 IEEE symposium on security and privacy (SP)*, pp. 299–316. IEEE, 2019.
- Matthew Jagielski, Jonathan Ullman, and Alina Oprea. Auditing differentially private machine learning: How private is private sgd? *Advances in Neural Information Processing Systems*, 33:22205–22216, 2020.
- Fatima Jahan Sarmin, Atiquer Rahman Sarkar, Yang Wang, and Noman Mohammed. Synthetic data: Revisiting the privacy-utility trade-off. *arXiv e-prints*, pp. arXiv-2407, 2024.
- Alistair E. W. Johnson, Lucas Bulgarelli, Lu Shen, Alvin Gayles, Ayad Shammout, Steven Horng, Tom J. Pollard, Sicheng Hao, Benjamin Moody, Brian Gow, Li wei H. Lehman, Leo A. Celi, and Roger G. Mark. MIMIC-IV, a freely accessible electronic health record dataset. *Scientific Data*, 10(1):1, 2023a. doi: 10.1038/s41597-022-01899-x. URL <https://doi.org/10.1038/s41597-022-01899-x>.
- Alistair EW Johnson, Tom J Pollard, Lu Shen, Li-wei H Lehman, Mengling Feng, Mohammad Ghassemi, Benjamin Moody, Peter Szolovits, Leo Anthony Celi, and Roger G Mark. MIMIC-iii, a freely accessible critical care database. *Scientific data*, 3(1):1–9, 2016.
- Alistair EW Johnson, Lucas Bulgarelli, Lu Shen, Alvin Gayles, Ayad Shammout, Steven Horng, Tom J Pollard, Sicheng Hao, Benjamin Moody, Brian Gow, Li-Wei H Lehman, Leo A Celi, and Roger G Mark. MIMIC-iv, a freely accessible electronic health record dataset. *Scientific Data*, 10(1):1, 2023b. doi: 10.1038/s41597-022-01899-x.
- James Jordon, Jinsung Yoon, and Mihaela Van Der Schaar. Pate-gan: Generating synthetic data with differential privacy guarantees. In *International conference on learning representations*, 2018.
- James Jordon, Lukasz Szpruch, Florimond Houssiau, Mirko Bottarelli, Giovanni Cherubin, Carsten Maple, Samuel N Cohen, and Adrian Weller. Synthetic data—what, why and how? *arXiv preprint arXiv:2205.03257*, 2022.
- Bayrem Kaabachi, Jérémie Despraz, Thierry Meurers, Karen Otte, Mehmed Halilovic, Bogdan Kulynych, Fabian Prasser, and Jean Louis Raisaro. A scoping review of privacy and utility metrics in medical synthetic data. *NPJ digital medicine*, 8(1):60, 2025.
- Peter Kairouz, H. Brendan McMahan, Brendan Avent, Aurélien Bellet, Mehdi Bennis, Arjun Nitin Bhagoji, Kallista Bonawitz, Zachary Charles, Graham Cormode, Rachel Cummings, Rafael G. L. D’Oliveira, Hubert Eichner, Salim El Rouayheb, David Evans, Josh Gardner, Zachary Garrett, Adrià Gascón, Badih Ghazi, Phillip B. Gibbons, Marco Gruteser, Zaid Harchaoui, Chaoyang He, Lie He, Zhouyuan Huo, Ben Hutchinson, Justin Hsu, Martin Jaggi, Tara Javidi, Gauri Joshi, Mikhail Khodak, Jakub Konečný, Aleksandra

- Korolova, Farinaz Koushanfar, Sanmi Koyejo, Tancrede Lepoint, Yang Liu, Prateek Mittal, Mehryar Mohri, Richard Nock, Ayfer Özgür, Rasmus Pagh, Hang Qi, Daniel Ramage, Ramesh Raskar, Mariana Raykova, Dawn Song, Weikang Song, Sebastian U. Stich, Ziteng Sun, Ananda Theertha Suresh, Florian Tramèr, Praneeth Vepakomma, Jianyu Wang, Li Xiong, Zheng Xu, Qiang Yang, Felix X. Yu, Han Yu, and Sen Zhao. Advances and open problems in federated learning. *Foundations and Trends in Machine Learning*, 14(1–2): 1–210, 2021. doi: 10.1561/22000000083.
- Georgios Kaissis, Alexander Ziller, Jonathan Passerat-Palmbach, Théo Ryffel, Dmitrii Usynin, Andrew Trask, Ionésio Lima Jr, Jason Mancuso, Friederike Jungmann, Marc-Matthias Steinborn, et al. End-to-end privacy preserving deep learning on multi-institutional medical imaging. *Nature Machine Intelligence*, 3(6):473–484, 2021.
- Georgios A Kaissis, Marcus R Makowski, Daniel Rückert, and Rickmer F Braren. Secure, privacy-preserving and federated machine learning in medical imaging. *Nature Machine Intelligence*, 2(6):305–311, 2020.
- Gavin Kerrigan, Dylan Slack, and Jens Tuyls. Differentially private language models benefit from public pre-training. *arXiv preprint arXiv:2009.05886*, 2020.
- Jin Li, Benjamin J Cairns, Jingsong Li, and Tingting Zhu. Generating synthetic mixed-type longitudinal electronic health records for artificial intelligent applications. *NPJ digital medicine*, 6(1):98, 2023.
- Zhangbing Li, Baichuan Wang, Jinsheng Li, Yi Hua, and Shaobo Zhang. Local differential privacy protection for wearable device data. *Plos one*, 17(8):e0272766, 2022.
- Fang Liu and Demosthenes Panagiotakos. Real-world data: a brief review of the methods, applications, challenges and opportunities. *BMC Medical Research Methodology*, 22(287), 2022. doi: 10.1186/s12874-022-01768-6.
- WeiKang Liu, Yanchun Zhang, Hong Yang, and Qinxue Meng. A survey on differential privacy for medical data analysis. *Annals of Data Science*, 11(2):733–747, 2024.
- Ximeng Liu, Lehui Xie, Yaopeng Wang, Jian Zou, Jinbo Xiong, Zuobin Ying, and Athanasios V Vasilakos. Privacy and security issues in deep learning: A survey. *IEEE Access*, 9:4566–4593, 2020.
- Greta M Ljung and George E. P. Box. On a measure of lack of fit in time series models. *Biometrika*, 65(2): 297–303, 1978.
- Mohammad Loni, Fatemeh Poursalim, Mehdi Asadi, and Arash Gharehbaghi. A review on generative ai models for synthetic medical text, time series, and longitudinal data. *npj Digital Medicine*, 8(1):281, 2025.
- Simeone Marino, Nina Zhou, Yi Zhao, Lu Wang, Qiucheng Wu, and Ivo D. Dinov. HDDA: DataSifter: statistical obfuscation of electronic health records and other sensitive datasets. *Journal of Statistical Computation and Simulation*, 89(2):249–271, 2019. doi: 10.1080/00949655.2018.1545228. URL <https://doi.org/10.1080/00949655.2018.1545228>.
- H Brendan McMahan, Daniel Ramage, Kunal Talwar, and Li Zhang. Learning differentially private recurrent language models. *arXiv preprint arXiv:1710.06963*, 2017.
- Ninareh Mehrabi, Fred Morstatter, Nripsuta Saxena, Kristina Lerman, and Aram Galstyan. A survey on bias and fairness in machine learning. *ACM computing surveys (CSUR)*, 54(6):1–35, 2021.
- Luca Melis, Congzheng Song, Emiliano De Cristofaro, and Vitaly Shmatikov. Inference attacks against collaborative learning. *arXiv preprint arXiv:1805.04049*, 13, 2018.
- Ilya Mironov. Rényi differential privacy. In *2017 IEEE 30th computer security foundations symposium (CSF)*, pp. 263–275. IEEE, 2017.
- Margaret Mitchell, Simone Wu, Andrew Zaldivar, Parker Barnes, Lucy Vasserman, Ben Hutchinson, Elena Spitzer, Inioluwa Deborah Raji, and Timnit Gebru. Model cards for model reporting. In *Proceedings of the conference on fairness, accountability, and transparency*, pp. 220–229, 2019.
- Kundan Munjal and Rekha Bhatia. A systematic review of homomorphic encryption and its contributions in healthcare industry. *Complex & Intelligent Systems*, 9(4):3759–3786, 2023.
- Antonio Muñoz, Ruben Ríos, Rodrigo Román, and Javier López. A survey on the (in) security of trusted execution environments. *Computers & Security*, 129:103180, 2023.

- Arvind Narayanan and Vitaly Shmatikov. Robust de-anonymization of large sparse datasets. In *2008 IEEE Symposium on Security and Privacy (sp 2008)*, pp. 111–125. IEEE, 2008.
- Boye Niu, Yiliao Song, Kai Lian, Yifan Shen, Yu Yao, Kun Zhang, and Tongliang Liu. Flow: Modularized agentic workflow automation, 2025. URL <https://arxiv.org/abs/2501.07834>.
- Olga Ohrimenko, Felix Schuster, Cédric Fournet, Aastha Mehta, Sebastian Nowozin, Kapil Vaswani, and Manuel Costa. Oblivious {Multi-Party} machine learning on trusted processors. In *25th USENIX Security Symposium (USENIX Security 16)*, pp. 619–636, 2016.
- Lisa Pilgram, Haksoo Ko, Adeline Tung, and Khaled El Emam. Protecting patient privacy in tabular synthetic health data: a regulatory perspective. *NPJ Digital Medicine*, 8(1):732, 2025.
- Joelle Pineau, Philippe Vincent-Lamarre, Koustuv Sinha, Vincent Larivière, Alina Beygelzimer, Florence d’Alché Buc, Emily Fox, and Hugo Larochelle. Improving reproducibility in machine learning research (a report from the neurips 2019 reproducibility program). *Journal of machine learning research*, 22(164):1–20, 2021.
- René Raab, Arne Küderle, Anastasiya Zakreuskaya, Ariel D Stern, Jochen Klucken, Georgios Kaissis, Daniel Rueckert, Susanne Boll, Roland Eils, Harald Wagener, et al. Federated electronic health records for the european health data space. *The Lancet Digital Health*, 5(11):e840–e847, 2023.
- Pranav Rajpurkar, Jeremy Irvin, Kaylie Zhu, Brandon Yang, Hershel Mehta, Tony Duan, Daisy Ding, Aarti Bagul, Curtis Langlotz, Katie Shpanskaya, et al. Chexnet: Radiologist-level pneumonia detection on chest x-rays with deep learning. *arXiv preprint arXiv:1711.05225*, 2017.
- Nicola Rieke, Jonny Hancox, Wenqi Li, Fausto Milletari, Holger R Roth, Shadi Albarqouni, Spyridon Bakas, Mathieu N Galtier, Bennett A Landman, Klaus Maier-Hein, et al. The future of digital health with federated learning. *NPJ digital medicine*, 3(1):119, 2020.
- Christine Riou, Mohamed El Azzouzi, Anne Hespel, Emeric Guillou, Gouenou Coatrieux, and Marc Cuggia. Ensuring gdpr compliance and security in a clinical data warehouse: Challenges and insights from a university hospital (preprint). *JMIR Medical Informatics*, 13:e63754, 2024.
- Juan C Rojas, Kyle A Carey, Dana P Edelson, Laura R Venable, Michael D Howell, and Matthew M Churpek. Predicting intensive care unit readmission with machine learning using electronic health record data. *Annals of the American Thoracic Society*, 15(7):846–853, 2018.
- Adrian-Silviu Roman. Evaluating the privacy and utility of time-series data perturbation algorithms. *Mathematics*, 11(5):1260, 2023.
- Nithya Sambasivan, Shivani Kapania, Hannah Highfill, Diana Akrong, Praveen Kumar Paritosh, and Lora Mois Aroyo. “Everyone wants to do the model work, not the data work”: Data cascades in high-stakes AI. In *CHI Conference on Human Factors in Computing Systems*, CHI ’21, Yokohama, Japan, 2021. ACM. doi: 10.1145/3411764.3445518.
- Mohamed H Shahin, Srijib Goswami, Sebastian Lobentanzer, and Brian W Corrigan. Agents for change: Artificial intelligent workflows for quantitative clinical pharmacology and translational sciences. *Clinical and Translational Science*, 18(3):e70188, 2025.
- Woong Shin, Renan Souza, Daniel Rosendo, Frédéric Suter, Feiyi Wang, Prasanna Balaprakash, and Rafael Ferreira da Silva. The (r) evolution of scientific workflows in the agentic ai era: Towards autonomous science. In *Proceedings of the SC’25 Workshops of the International Conference for High Performance Computing, Networking, Storage and Analysis*, pp. 2305–2316, 2025.
- Reza Shokri, Marco Stronati, Congzheng Song, and Vitaly Shmatikov. Membership inference attacks against machine learning models. In *2017 IEEE Symposium on Security and Privacy (SP)*, pp. 3–18. IEEE, 2017.
- Theresa Stadler, Bristena Oprisanu, and Carmela Troncoso. Synthetic data–anonymisation groundhog day. In *31st USENIX Security Symposium (USENIX Security 22)*, pp. 1451–1468, 2022.
- Thomas Steinke, Milad Nasr, and Matthew Jagielski. Privacy auditing with one (1) training run. *Advances in Neural Information Processing Systems*, 36:49268–49280, 2023.
- Latanya Sweeney. k-anonymity: A model for protecting privacy. *International journal of uncertainty, fuzziness and knowledge-based systems*, 10(05):557–570, 2002.

- Muhang Tian, Bernie Chen, Allan Guo, Shiyi Jiang, and Anru R Zhang. Reliable generation of privacy-preserving synthetic electronic health record time series via diffusion models. *Journal of the American Medical Informatics Association*, 31(11):2529–2539, 2024.
- Eric J Topol. High-performance medicine: the convergence of human and artificial intelligence. *Nature medicine*, 25(1):44–56, 2019.
- Florian Tramèr, Fan Zhang, Ari Juels, Michael K Reiter, and Thomas Ristenpart. Stealing machine learning models via prediction {APIs}. In *25th USENIX security symposium (USENIX Security 16)*, pp. 601–618, 2016.
- Mark van Velzen, Robert F van der Willigen, Vincent J De Beer, Helen I de Graaf-Waar, Esther RC Janssen, Sjemaine van Leeuwen, Micha F van der Willigen, Martijn J Van Der Willigen, Gavin Renardus, Rayan El Maaroufi, et al. Privacy-, linguistic-, and information-preserving synthesis of clinical documentation through generative agents. *Frontiers in Artificial Intelligence*, 8:1644084, 2025.
- Echo H Wang, Puja Myles, Randi Foraker, Sengwee Toh, Lucy Mosquera, Khaled El Emam, and Mehmet Burcu. Crossing borders securely: synthetic data and federated networks for privacy-preserving access to real-world data and emerging use cases. *npj Digital Medicine*, 8(1):758, 2025.
- Tianhao Wang, Joann Qionga Chen, Zhikun Zhang, Dong Su, Yueqiang Cheng, Zhou Li, Ninghui Li, and Somesh Jha. Continuous release of data streams under both centralized and local differential privacy. In *Proceedings of the 2021 ACM SIGSAC Conference on Computer and Communications Security*, pp. 1237–1253, 2021.
- Stanley L Warner. Randomized response: A survey technique for eliminating evasive answer bias. *Journal of the American statistical association*, 60(309):63–69, 1965.
- H Xu, T Zhu, L Zhang, and W Zhou. P. yu. machine unlearning: A survey. *ACM Computing Surveys*, 2023.
- Lei Xu, Maria Skoularidou, Alfredo Cuesta-Infante, and Kalyan Veeramachaneni. Modeling tabular data using conditional GAN. In *Advances in Neural Information Processing Systems*, volume 32, 2019a.
- Lei Xu, Maria Skoularidou, Alfredo Cuesta-Infante, and Kalyan Veeramachaneni. Modeling tabular data using conditional gan. *Advances in neural information processing systems*, 32, 2019b.
- Yifan Yang, Mingquan Lin, Han Zhao, Yifan Peng, Furong Huang, and Zhiyong Lu. A survey of recent methods for addressing ai fairness and bias in biomedicine. *Journal of Biomedical Informatics*, 154:104646, 2024.
- Samuel Yeom, Irene Giacomelli, Matt Fredrikson, and Somesh Jha. Privacy risk in machine learning: Analyzing the connection to overfitting. In *2018 IEEE 31st Computer Security Foundations Symposium (CSF)*, pp. 268–282. IEEE, 2018.
- Jinsung Yoon, Daniel Jarrett, and Mihaela Van der Schaar. Time-series generative adversarial networks. *Advances in neural information processing systems*, 32, 2019.
- Jinsung Yoon, Michel Mizrahi, Nahid Farhady Ghalaty, Thomas Jarvinen, Ashwin S Ravi, Peter Brune, Fanyu Kong, Dave Anderson, George Lee, Arie Meir, et al. Ehr-safe: generating high-fidelity and privacy-preserving synthetic electronic health records. *NPJ digital medicine*, 6(1):141, 2023.
- Hongyi Yuan, Songchi Zhou, and Sheng Yu. Ehrdiff: Exploring realistic ehr synthesis with diffusion models. *arXiv preprint arXiv:2303.05656*, 2023.
- Jiangjun Yuan, Weinan Liu, Jiawen Shi, and Qingqing Li. Approximate homomorphic encryption based privacy-preserving machine learning: a survey. *Artificial Intelligence Review*, 58(82), 2025. doi: 10.1007/s10462-024-11076-8.
- Ziqi Zhang, Chao Yan, and Bradley A Malin. Membership inference attacks against synthetic health data. *Journal of biomedical informatics*, 125:103977, 2022.

---

<sup>†</sup>Equal contribution. <sup>‡</sup>AI co-author (SciencePal Agent); see Appendix 11 for a detailed role statement.

\*Corresponding author.

## Appendix A: Author Contribution Statement

A distinguishing feature of this work is that we explicitly include SciencePal, an AI agent system, as a co-author and document every contributor’s role with full transparency. We believe that openly crediting AI contributions, rather than concealing them behind vague acknowledgments, is both more honest and more reproducible. To the best of our knowledge, this is among the first efforts to grant formal co-authorship to an AI system while simultaneously providing a granular, per-author contribution breakdown that places the AI on equal footing with human contributors in terms of disclosure. We hope that this practice may serve as a reference point for future human–AI collaborative research across the broader scientific community. All scientific judgments, ethical responsibilities, and final decisions rest solely and entirely with the human authors listed in this paper.

### Per-author contributions

**Beining Bao.** Led the execution of all experiments reported in this paper, spanning geometric validation, statistical divergence analysis, adversarial-attack evaluation, and end-to-end downstream prediction tasks on the MIMIC-IV dataset. Took primary responsibility for hyperparameter tuning across all operator configurations, conducted systematic sanity checks to verify numerical correctness, and performed detailed error analyses to trace unexpected behaviors back to their root causes. Managed runtime benchmarking across CPU and GPU settings, generated all figures and tables presented in the experimental sections, and ensured that every reported number was reproducible from the committed codebase. Co-drafted substantial portions of the initial manuscript text, with a particular focus on the method details, experimental setup, results description, and result interpretation sections. Also contributed to iterative rounds of revision by incorporating feedback from other co-authors and refining the narrative flow between sections.

**Maolin Wang.** Managed the overall project timeline from initial conception through final manuscript preparation, and coordinated task allocation and communication among all human authors and between the human team and the SciencePal AI system throughout the project lifecycle. Served as the central hub for cross-team collaboration, organizing regular progress meetings, consolidating feedback from clinical advisors, engineering contributors, and the SciencePal platform team, and ensuring that decisions and action items were clearly communicated and tracked across all parties involved. On the engineering side, contributed substantially to the codebase by implementing and maintaining core data processing pipelines, including the ETL modules that extracted and standardized MIMIC-IV tables into the feature matrices consumed by downstream operator and attack experiments. Wrote and reviewed significant portions of the experimental scripting infrastructure, such as batch job orchestration, result aggregation, and automated logging, which enabled the team to run large-scale experiments efficiently and reproducibly. Designed and maintained the human–AI collaboration workflow, which included crafting structured prompts that translated high-level research goals into actionable AI queries, systematically reviewing and filtering AI-generated code snippets and text fragments for relevance and correctness.

**SciencePal (AI co-author).** Contributed to mathematical operator design and formal analysis under human-specified constraints, including conditions C1 through C5, CPU-friendliness, and the requirement of no long-term key storage. Given high-level privacy and utility requirements articulated by human authors, SciencePal explored a broad space of candidate column-level transforms, including local rotations, orthogonal projections, piecewise-linear maps, Householder reflections, permutation-based shuffles, and various orthogonal mixing schemes, and proposed initial operator formulations together with analytical sketches for properties such as mean and variance preservation, invertibility behavior, and reconstruction difficulty under different adversarial knowledge levels. A carefully curated subset of these proposals, specifically the T1, T2, and T3 operators and the per-stay Q-mix mechanism, was subsequently selected, simplified, and rigorously formalized by the human authors, who also constructed counterexamples and tightened the arguments where needed. Beyond operator design, SciencePal contributed to attack and evaluation protocol exploration by proposing variants of reconstruction, record linkage, membership inference, and attribute inference attacks, as well as suggesting experimental flows for each attack family; human authors then formalized, simplified, or substantially modified these suggestions into the final attack matrix and protocols used in the evaluation sections. SciencePal also generated prototype code for operations such as z-score transformation pipelines, simple linear and ridge-regression reconstruction baselines, statistical divergence computation, and basic plotting utilities; all of these prototypes were re-implemented, extended, hardened, and optimized by human authors in a local environment, and were subjected to security and scalability review before any use on real clinical data. In addition, SciencePal produced draft text fragments for selected method and discussion sections in both English and Chinese, and suggested alternative structural organizations for the manuscript, such as splitting the Discussion Section into positioning, clinical scenarios,

operator analysis, Q-mix analysis, limitations, and future work subsections. All such textual output was treated as raw material; human authors thoroughly reviewed, rewrote, trimmed, reorganized, and integrated these fragments into the final manuscript, ensuring consistency of style, technical accuracy, and alignment with the overall narrative.

**Gan Yuan and Yao Wang.** Validated the AI-generated intermediate results, including operator outputs, attack success metrics, and downstream task performance numbers, against domain knowledge and clinical plausibility throughout the project. Contributed to scenario-level validation by assessing whether the proposed privacy-preserving views remain meaningful and actionable in realistic hospital analytics workflows, for instance verifying that transformed vital-sign distributions retain clinically interpretable ranges and that length-of-stay predictions built on protected views do not introduce systematic bias in patient subgroups. Provided feedback on operator parameter choices from the perspective of practitioners who routinely work with clinical data, and helped identify edge cases, such as extreme outlier patients or rare diagnosis codes, where additional robustness testing was warranted. Also participated in manuscript review by checking that the clinical motivation sections accurately reflected current hospital data governance practices and regulatory expectations.

**Hongyu Chen, Bingkun Zhao, and Baoshuo Kan.** Assisted in the day-to-day execution and support of the project across multiple stages. Helped prepare and preprocess the MIMIC-IV data tables used in the experiments, including cleaning raw extracts, aligning stay-level identifiers across modules, and producing the standardized feature matrices consumed by the operator and attack pipelines. Assisted in running batch experiments, collecting and organizing intermediate outputs, and maintaining version-controlled records of experimental configurations so that results could be reliably reproduced. Contributed to literature survey efforts by collecting, categorizing, and summarizing related work on differential privacy, synthetic data generation, and clinical NLP de-identification, which informed the positioning and related-work sections of the manuscript. Also assisted in proofreading draft sections, cross-checking notation consistency across sections, verifying reference formatting, and preparing supplementary materials such as additional tables and plots that supported the main experimental narrative.

**Wei-Ying Ma, Qi Shi, and Yinggong Zhao.** Responsible for the design, development, deployment, and ongoing maintenance of the SciencePal agent platform that served as the AI backbone of this collaboration. Provided the underlying large-language-model infrastructure, API services, prompt orchestration layer, and tool-use capabilities that enabled the human–AI co-design workflow used throughout this project. Ensured system reliability and response quality during the intensive experimentation and writing phases, iterated on the agent’s mathematical reasoning and code generation modules in response to feedback from the research team, and supported the integration of domain-specific knowledge sources that improved the relevance of SciencePal’s operator and attack suggestions. Their engineering efforts made it possible for the research team to interact with SciencePal as a responsive, context-aware collaborator rather than a text completion tool.

**Jiming Xu.** Provided deep domain expertise in clinical data systems, electronic health record architectures, and health-care information technology infrastructure. Verified the clinical value and practical relevance of the proposed privacy framework by evaluating whether the operator-based view generation approach is compatible with the data pipelines, access control models, and audit requirements found in production hospital environments. Served as a consulting advisor on real-world deployment considerations, including computational budget constraints in resource-limited hospital IT departments, regulatory alignment with data protection standards, and the practical trade-offs between privacy strength and data utility that clinical stakeholders care about most. Also contributed insights on how the proposed framework could interoperate with existing commercial de-identification solutions and hospital data warehouse systems, and reviewed the manuscript sections on system architecture and clinical scenarios for factual accuracy.

**Jun Yan.** Defined the core research problem, specifically the notion of “in-hospital usable and visible, but hard to reconstruct” numeric views, and formulated the overall modeling framework that structures the entire paper. This framework includes the mean–variance manifold perspective that provides the geometric foundation, the  $z$ -score  $\alpha$ -hierarchy that organizes operators by privacy strength, and the threat model with adversarial capability levels L0, L1, and L2 and attack families A, B, C, and D. Independently validated key theoretical results, including the conditions under which each operator satisfies or violates properties C1 through C5, and cross-checked critical experimental conclusions against back-of-the-envelope calculations to ensure consistency. Contributed to the design and partial implementation of several SciencePal agent capabilities that were used in this collaboration, bridging the gap between general-purpose language model reasoning and the specialized mathematical and privacy-engineering demands of the project. Supervised

the overall scientific direction, resolved disagreements on modeling choices, made final decisions on which results to include or exclude, and performed the last round of manuscript review to ensure that all claims are adequately supported by evidence.

### **Boundaries and responsibility**

**Independent verification.** All scientific conclusions and quantitative results reported in this paper were independently verified by at least one human author before inclusion in the manuscript. This verification covers, but is not limited to, attack success rates,  $R^2$  reconstruction curves, AUROC and AUPRC scores for downstream prediction tasks, Kolmogorov–Smirnov statistics for distributional fidelity, runtime benchmarks across CPU and GPU configurations, and the correctness of all figures and tables. Any preliminary interpretation or explanation provided by SciencePal during the research process was treated strictly as a hypothesis to be checked and, where necessary, re-derived or corrected by human authors; no AI-generated interpretation was accepted at face value.

**Responsibility.** Although SciencePal is credited as a co-author to transparently and accurately reflect its substantive contributions to operator design, code prototyping, and text drafting, all theoretical claims, methodological choices, threat model specifications, experimental designs, parameter settings, interpretive conclusions, and policy recommendations presented in this paper are the sole responsibility of the human authors. The human authors collectively accept full accountability for the correctness, reproducibility, and ethical compliance of the work, and any errors or omissions should be attributed to them rather than to the AI system.

**Referencing this collaboration.** We encourage other researchers who wish to reference the human–AI collaboration model adopted in this work to do so in a way that clearly distinguishes the roles of human authors and the AI system. For example, one may write: *“This work credits SciencePal (AI agent) as a co-author for its contributions to operator design, analytical sketching, and drafting support; all scientific responsibility rests with the human authors.”* We also welcome future studies that build upon, refine, or critique the co-authorship and disclosure framework presented here, as we believe that establishing community norms for transparent AI attribution is an evolving process that benefits from open discussion and diverse perspectives.